Manipulation of non-trivial magnetic states in electron doped noncollinear antiferromagnetic Mn_3Sn

By

Charanpreet Singh

Enrolment No: PHYS11201604010

National Institute of Science Education and Research, Bhubaneswar

A thesis submitted to the

Board of Studies in Physical Sciences

In partial fulfillment of requirements

for the Degree of

DOCTOR OF PHILOSOPHY

of

HOMI BHABHA NATIONAL INSTITUTE

July, 2022

Homi Bhabha National Institute

Recommendations of the Viva Voce Committee

As members of the Viva Voce Committee, we certify that we have read the dissertation prepared by **Charanpreet Singh** entitled **Manipulation of non-trivial magnetic states in electron doped noncollinear antiferromagnetic Mn_3Sn** and recommend that it may be accepted as fulfilling the thesis requirement for the award of Degree of Doctor of Philosophy.

Chairman – Prof. Bedangadas Mohanty — 14/04/2023

Guide / Convener – Dr. Ajaya K. Nayak — 14/04/2023

Co-guide -

Examiner – Dr. Pranaba Kishor Muduli — 14.4.2023

Member 1- Dr. Kartikeswar Senapati — 14/04/2023

Member 2- Dr. Anamitra Mukherjee — 14/04/2023

Member 3- Dr. Debakanta Samal — 14/04/23

Final approval and acceptance of this thesis is contingent upon the candidate's submission of the final copies of the thesis to HBNI.

I/We hereby certify that I/we have read this thesis prepared under my/our direction and recommend that it may be accepted as fulfilling the thesis requirement.

Date: 14/04/2023

Place: NISER

Dr. Ajaya K. Nayak

Guide

STATEMENT BY AUTHOR

This dissertation has been submitted in partial fulfillment of requirements for an advanced degree at Homi Bhabha National Institute (HBNI) and is deposited in the Library to be made available to borrowers under rules of the HBNI.

Brief quotations from this dissertation are allowable without special permission, provided that accurate acknowledgement of source is made. Requests for permission for extended quotation from or reproduction of this manuscript in whole or in part may be granted by the Competent Authority of HBNI when in his or her judgment the proposed use of the material is in the interests of scholarship. In all other instances, however, permission must be obtained from the author.

Charanpreet Singh

DECLARATION

I, hereby declare that the investigation presented in the thesis has been carried out by me. The work is original and has not been submitted earlier as a whole or in part for a degree / diploma at this or any other Institution / University.

Charanpreet Singh

List of Publications arising from the thesis

Journal

- **Published**

    1. "Pressure controlled trimerization for switching of anomalous Hall effect in triangular antiferromagnet Mn_3Sn", **C. Singh**, V. Singh, G. Pradhan, V. Srihari, H. K. Poswal, R. Nath, A. K. Nandy, and A. K. Nayak, Phys. Rev. Research 2, 043366 (2020).

- **Communicated**

    1. "Higher order exchange driven noncoplanar magnetic state and large anomalous Hall effects in electron doped kagome magnet Mn_3Sn", **C. Singh**, S. Jamaluddin, A. K. Nandy, Amitabh Das, and A. K. Nayak (under review at Physical Review letter).

- **Manuscript under preparation**

    1. "Magnetic ground state of Sb-doped Mn_3Sn samples", **C. Singh**, and A. K. Nayak.

Conferences

1. Poster presentation at International Conference on Magnetic Materials and Applications (ICMAGMA)-2018, National Institute of Science Education and Research (NISER), Bhubaneswar, India.

2. Poster presentation at Modern Trends in Molecular Magnetism (MTMM)-2019, Indian Institute of Science Education and Research (IISER), Bhopal, India.

Others

1. "Observation of the topological Hall effect and signature of room-temperature antiskyrmions in Mn-Ni-Ga D_2d Heusler magnets", Subir Sen, **C. Singh**, P. K. Mukharjee, R. Nath, and A. K. Nayak, Phys. Rev. B 99, 134404 (2019).

2. "Current-induced nucleation, manipulation, and reversible switching of anti-skyrmioniums", S. K. Panigrahy, **C. Singh**, and A. K. Nayak, Appl. Phys. Lett. 115, 182403 (2019).

3. "Robust topological Hall effect driven by tunable noncoplanar magnetic state in Mn-Pt-In inverse tetragonal Heusler alloys", B. Giri, A. I. Mallick, **C. Singh**, P. V. P. Madduri, F. Damay, A. Alam, and A. K. Nayak, Phys. Rev. B 102, 014449 (2020).

Charanpreet Singh

DEDICATIONS

Dedicated to

.....

My Loving parents

Balvinder Singh

Jaspreet Kaur

....

and to my brother

Navot Singh 'Babbar'

ACKNOWLEDGEMENTS

First of all, I would like to take the opportunity to express my gratitude to my supervisor, Dr. Ajaya Kumar Nayak, for his constant support and encouragement throughout my Ph.D. tenure. He allowed me to conduct independent research, which I greatly appreciate. I am deeply thankful to him for his valuable input and guidance in improving my knowledge. I am also grateful for his critical suggestions to improve this thesis manuscript.

I want to thank Prof. Bedangadas Mohanty, chairman of the doctoral committee, for his continuous encouragement and suggestions to improve my practical knowledge of the subject. His presence during the annual evaluation seminars always motivated me to work harder, study more and prepare better. I would also like to thank the rest of my doctoral committee members, Dr. Anamitra Mukherjee and Dr. Kartikeswar Senapati, for the continuous assessment of my work. I want to thank Dr. Debakanta Samla from IOP Bhubaneswar for his kind evaluation of my work as an external doctoral committee member. Their inquiries and doubts prompted me to learn more about the physics of the problem, which invariably improved my understanding of the topic.

I am immensely grateful to Dr. Ashis Kumar Nandy for his support in theoretical calculations. My thesis work would not have been completed without his continuous help in theory calculations and valuable inputs. The countless discussion with him has helped me a lot. I would also like to thank our collaborators, Prof. Ramesh Nath from IISER Trivandrum, Velaga Srihari and Dr. Himanshu Kumar Poswal, RRCAT Indore, Amitabh Das sir at BARC, Mumbai, and Prof. Maxim Avdeev at ANSTO, Australia.

I wish to thank the friends I met at NISER: Tanim Firdoshi, Rashmi Rekha Sahoo, Subir Sen, Sujit Garain, Sk Jamaluddin, Bimalesh Giri, Kalyaan Ghosh, Dola Chakarbartty, Anupa Kumari, and the list goes on. Without you guys, there

is no way I could have completed my doctoral. I also want to thanks all my lab mates.

The Financial assistance provided by NISER during my Ph.D. tenure is gratefully acknowledged.

Finally, my most valued thanks to my family members: my parents for their affection and love. I am very grateful to my parents for their blessing, moral support, unconditional love, and sacrifice, which gave me the strength to embrace and complete my Ph.D. in time. And I love my brother, who is always there, no matter what.

Contents

Title page **i**

SUMMARY **xii**

List of Figures **xv**

1 Introduction **1**

1.1 Magnetic energy landscape: Exchange interactions 3

1.1.1 Direct Exchange 4

1.1.2 Indirect Exchange 4

1.1.3 Asymmetric or chiral exchange 8

1.1.4 Higher order exchange 8

1.2 Magnetically ordered states 12

1.2.1 Collinear magnetic states 12

1.2.2 Noncollinear magnetic states 12

1.3 Electrical transport of magnetic systems 17

1.3.1 Intrinsic contribution 19

1.3.2 Extrinsic contribution 21

1.3.3 Scaling of anomalous Hall 22

1.4 Kagome lattice system Mn_3Sn 24

1.4.1 Crystal structure and magnetic ground state of Mn_3Sn 24

1.4.2 Important aspects of iT-AFM structure in Mn_3Sn 28

1.4.3 Open questions 33

1.5 Outline of the Thesis 37

2 Experimental techniques and methods 39

2.1 Sample preparation 39

2.2 Structural characterization 43

2.2.1 X-ray Diffraction 43

2.2.2 Extreme condition XRD 44

2.3 Magnetic characterization 45

2.3.1 Vibrating sample magnetometer 46

2.3.2 Superconducting Quantum Interference Device 47

2.3.3 High pressure magnetic measurements 48

2.3.4 Neutron diffraction 49

2.4 Electronic transport measurements 51

2.5 Analysis and theoretical methods 53

2.5.1 Density functional theory (DFT) 54

2.5.2 Calculation details 56

3 Pressure induced switching of noncollinear magnetic state in Mn_3Sn 57

3.1 Sample characterization 58

3.1.1 Determination of sample structure 58

3.1.2 Magnetic properties 60

3.1.3 Confirmation of magnetic ground state : neutron diffraction (ND) 63

3.1.4 Electronic transport properties 65

3.2 Temperature dependence of crystal structure 68

3.3 Pressure dependent ground state and switching of anomalous Hall effect 68

3.3.1 Magnetic properties 70

3.3.2 Electronic transport properties 75

3.4 Theoretical understanding 76

3.4.1 Analysis of exchange Hamiltonian 78

3.4.2 The real Mn_3Sn Kagome lattice : Effect of trimerization . . . 79
3.4.3 *ab-initio* calculations . . . 83
3.5 Conclusion . . . 86

4 Higher order exchange interaction driven noncoplanar magnetic state in Mn_3Sn 87
4.1 Structural characterization of $Mn_{3-x}Fe_xSn$ samples . . . 89
4.2 Compositional analysis . . . 90
4.3 Magnetic properties of samples . . . 92
4.4 'True' magnetic ground state of Mn_3Sn . . . 98
4.4.1 Proposed magnetic ground state . . . 98
4.4.2 Neutron diffraction study of ground state . . . 99
4.5 Transport properties of canted ground state . . . 103
4.5.1 Confirmation of the scalar spin chirality mechanism . . . 107
4.6 Dual magnetic order . . . 110
4.7 Theoretical study of magnetic ground state . . . 113
4.7.1 Ground state from $ab-initio$ studies . . . 113
4.7.2 Effects of higher order exchange interactions on the iT-AFM ground state . . . 116
4.7.3 Analysis of the data from DFT calculations . . . 119
4.8 Conclusion . . . 124

5 Magnetic properties of Sb doped Mn_3Sn samples 127
5.1 Structural characterization of Sb doped samples . . . 128
5.2 Compositional analysis . . . 128
5.3 Magnetic properties of samples . . . 129
5.4 Electronic transport properties . . . 131
5.5 Summary and Discussion of experimental results . . . 133

6 Summary and conclusion 135
6.1 Future Outlook . . . 138

SUMMARY

The specific arrangement of the magnetic moments in a magnetic material controls the physical properties of the system. In most of the cases, the parallel and antiparallel arrangements of the moments are studied rigorously. However, as the field progress, a new type of magnetic state, namely the non-collinear magnetic order, has attracted much interest. In particular, the non-collinear antiferromagnets are the subject of special attention due to the recent findings of non-trivial magnetic and transport properties. Like the collinear antiferromagnets, non-collinear antiferromagnets also exhibit faster dynamics and exclude the effect of stray fields. In this direction, the kagome lattice compound Mn_3Sn is one of the most exciting antiferromagnets that exhibits a triangular antiferromagnetic ordering. Despite having zero magnetic moment, Mn_3Sn displays a large anomalous Hall effect due to the presence of cluster octupole magnetic order that breaks the time reversal symmetry.

Though the room temperature magnetic ground state of the Mn_3Sn is well known, the modification of the magnetic state with temperature is still not fully understood. Different Mn_3Sn samples displays two types of temperature dependency, one where the magnetization drops to zero suddenly below 200 K and the second one where the magnetization rises sharply below 50 K. The sudden reduction in magnetization in some of the samples at 200 K shows a helical modulation of the regular spin structure. The source for the rise in the magnetization in the other case is not well understood. This thesis reveals the mechanism of these temperature-induced magnetic transitions in different Mn_3Sn samples.

The magnetization and Hall transport measurements on the polycrystalline samples of $Mn_{3+x}Sn_{1-x}$ show that the helical phase transition can be stabilized for the $Mn_{3.03}Sn_{0.97}$ sample, whereas the $Mn_{3.05}Sn_{0.95}$ sample only shows the low temperature transition involving rise in the magnetization. It is found that the application

of external isotropic pressure leads to a phase transition from the inverse triangular structure to the helical phase for $Mn_{3.05}Sn_{0.95}$. This magnetic phase transition leads to a switching of the anomalous Hall signal of the samples. Theoretical calculations reveal that the exchange frustration of out-of-plane exchange interactions stabilizes the helical magnetic phase. It is also shown that the trimerization of the kagome lattice with an application of pressure plays a deterministic role in the exchange interaction.

It is found that the low temperature transition can be stabilized for the high electron doping samples. In this regard, single crystalline samples of $Mn_{3.09}Sn_{0.91}$, $Mn_{2.7}Fe_{0.3}Sn$ and $Mn_{2.5}Fe_{0.5}Sn$ are synthesized. The crystal direction-dependent magnetization measurements reveal that the magnetic moment exhibits a sudden rise when the field is applied along the *c*-axis of the sample. With higher Fe doping, the net magnetization along the c-axis and the temperature corresponding to the magnetization transition keeps increasing. The neutron diffraction measurements and the density functional theory (DFT) calculations confirms the partial reorientation of the magnetic moments of the inverse triangle structure along the *c*-axis, resulting in a canted magnetic ground state. A remarkable feature is noticed for the canted magnetic state, where the in-plane octupole order coexists along with the out-of-plane non-coplanar order. The presence of distinct Hall signals characterizing these two different magnetic orders is also demonstrated. Lastly, the theoretical calculations show that the canted state is stabilized by the high-order 4-spin and 6-spin exchange interactions.

Finally, the role of electron doping in stabilizing the canted state and thus the high order exchange interaction is probed by an alternate way of electron doping by replacing the nonmagnetic Sn atoms with the Sb atoms. However, the stabilization of the low temperature canted magnetic state is not observed. Instead, the Sb doping leads to the formation of the helical phase, which also shows a new magnetic

transition inside the helical phase for the high Sb doped samples.

List of Figures

1.1 Schematic representation of possible hopping scenarios of electrons in two sites 'A' and 'B'. (a) Hopping on a half filled three degenerate energy levels. (b) Hopping parameters on two sites with split energy levels. 5

1.2 Schematic of superexchange mechanism leading to an antiferromagnetic exchange between two Mn atoms. 6

1.3 Energy level schematic of double exchnage interaction between two Mn atoms with different oxidation states. 7

1.4 Schematic of 2-spin and different 4-spin exchange interactions. 9

1.5 Energy level schematic of a model system with non-degenerate energy levels. The hopping parameters for different possible hopping are marked (left). Multi hopping process leading to a 2-spin-two-site bi-quadratic interaction (right). 11

1.6 (a) A 1-D chain of atoms with possible magnetic states for different kind of exchange interactions. The exchange interactions between different sites are marked. (b) Ground state magnetic structure representation of a frustrated triangular lattice with in-plane and out-of-plane magnetic anisotropy. 13

1.7 Spin spirals of different handedness along with the direction of DMI vector for minimum energy in each state 14

1.8 (a) scanning tunneling microscopy (STM) graph of spin spiral measured on Mn/W(001) lattice (top) and a spin schematic of same spiral state (bottom).[26] (b) Different multi-Q states in the Brillouin zone of a hexagonal system. Spin schematic for multi-Q state corresponding to different q values is also shown.[27] 17

1.9 (a) Schematic of Hall voltage measurement setup. Plot of typical Hall voltage signal vs magnetic field for (a) ordinary and (b) anomalous Hall systems. 18

1.10 (a) Band structure of $RbMnCl_3$/graphene hetrostructure with band crossing points and corresponding Berry curvature.[29] (b) Schematic of a pair of Weyl points with opposite chirality. (c) The Berry phase originating form both points.[30] 21

1.11 Schematic of a layer of (a) triangular and (b) kagome lattice. The unit cell for each lattice is marked with wine color. Different colors have been used to show lattice points in a unit cell. 25

1.12 (a-b) Kagome with Sn at hexagon centres and a 180° rotates kagome lattice. (c) Mn_3Sn lattice made up of the two rotated kagome lattices. (d) Side view showing a shift along c-axis between two kagome layers. 26

1.13 (a) Spin structure of Mn_3Sn sample where exchange parameters are marked by lines. (b) Extended Mn_3Sn lattice with various exchange interactions as marked by colored lines. (c) Degenerate triangular and inverse triangular spin structure stabilized by exchange frustration on layered kagome lattice of Mn_3Sn. 27

1.14 (a) Anomalous Hall signal as observed for Mn_3Sn at room temperature for fields applied along different directions. (b) Hall signal for field applied along $[01\bar{1}0]$ direction at different temperatures.[42] (c) Anomalous Nernst signal measured in diffrent geometries.[43] (d) Thermal Hall effect signal for the Mn_3Sn samples at room temperature.[44] 28

1.15 (a) Brillouin zone of Mn_3Sn showing a pair of Weyl points around K points. (b) Band structure along high symmetry points for Mn_3Sn. Blue and red arrows mark the Weyl points with opposite chirality. Figures taken form reference [45]. 29

1.16 (a) Octupole polarization for different domains of iT-AFM structure of Mn_3Sn. (b) Magneto-optic Kerr effect (MOKE) images of Mn_3Sn thin films. Different contrast correspond to oppositely oriented octupole domains.[46] 30

1.17 (a) Schematic of polycrystalline Mn_3Sn/Pt layer. The green arrows in Pt layer represent splitting of electrons of opposite spins due to spin orbit coupling. (b) Write current v. Hall signal plot fro difference Mn_3Sn/X films, where X = Pt, Cu and W. Figures taken from reference [61]. 33

1.18 (a) Magnetization as a function of temperature plots under constant magnetic field for Mn_3Sn single crystals. (b) Hall resistivity measured as a function of magnetic field at 5K, 100K, and 300K. (c) Temperature dependence of Hall resistivity. All plots are taken from reference [62]. 34

1.19 The neutron powder diffraction data for Mn_3Sn at (c) 190 K and (d) 270 K under different magnetic fields around (101) reflection. The satellite reflections $(101)^{\pm}$ are visible at 190 K. (c) A schematic representation of the iT-AFM and helically modulated magnetic structure. Plots are taken from reference [66, 67]. 35

1.20 (a) Magnetization as a function of temperature plots under constant magnetic field for Mn_3Sn sample. (b) Magnetization and Hall resistivity measured as a function of magnetic field at 2K. Both plots are taken from reference [54]. 36

2.1 Arc-melting furnace used to melt and synthesize polycrystalline sample. 40

2.2 Binary phase diagram for Mn-Sn elements.[69] 41

2.3 Temperature profile used for the synthesis of single crystalline samples. The pointed alumina crucible was used to keep the powdered samples in furnace. 42

2.4 Schematic representation of x-ray diffracting from planes of atoms. . 43

2.5 (a) A schematic representation of a diamond anvil cell.[70] 45

2.6 The schematic diagram of a VSM coils attached with SQUID sensor. Picture taken from Quantum Design MPMS-3 user's manual. 47

2.7 Real and schematic picture of the Quantum Design made magnetic pressure cell. 48

2.8 Different magnetic states and their respective magnetic reflections along with the nuclear reflections.. Picture taken from reference [72]. 50

2.9 A schematic of the connection made so as to measure (a) longitudnal resistivity using four probe method and (b) Hall resistivity using five probe method. 51

2.10 Picture of the ACT high pressure cell used. 52

3.1 XRD patterns with Rietveld refinement for (a) $Mn_{3.03}Sn_{0.97}$, (b) $Mn_{3.04}Sn_{0.96}$, and (c) $Mn_{3.05}Sn_{0.95}$. Some high intensity peaks are labeled in the figure (a). The legend for first three plots is shown in figure (b). (d) Calculated a and c values from the Rietveld refinement. 59

3.2 Temperature dependence of zero field cooled (ZFC) and field cooled (FC) magnetization $[M(T)]$ for (a) $Mn_{3.03}Sn_{0.97}$, (b) $Mn_{3.04}Sn_{0.96}$ and (c) $Mn_{3.05}Sn_{0.95}$ samples. The first derivative of FC curve is also plotted as black line. (d) Temperature corresponding to low temperature and high temperature transition for three samples. The transition temperatures are calculated from derivative of FC curve. 61

3.3 Field dependent isothermal magnetization $[M(H)]$ loops for (a) $Mn_{3.05}Sn_{0.95}$ and (c) $Mn_{3.03}Sn_{0.97}$ sample measured at different temperatures. Magnified view of the low field regions of the $M(H)$ loops for both the samples are shown in (b) and (d). 62

3.4 Neutron diffraction data with Rietveld refinement at different temperatures for $Mn_{3.03}Sn_{0.97}$ sample. (a) and (b) shows the 300 K and 150 K data and the fitting with iT-AFM structure. (c) shows the fitting of 150 K data with modulated iT-AFM structure. 64

3.5 (a) ND data around the (101) reflection for the $Mn_{3.03}Sn_{0.97}$ sample at different temperatures. (b) Value of the helical phase modulation vector as extracted from Rietveld refinement of neutron diffraction data. 65

3.6 (a) Temperature dependent longitudinal resistivity (ρ_{xx}) plots for $Mn_{3.03}Sn_{0.97}$ and $Mn_{3.05}Sn_{0.95}$ samples. Inset shows a magnified view of the temperature around helical transition. (b) $\rho_{xx}(T)/\rho_{xx}(300\text{ K})$ plot for the two samples. 66

3.7 Field dependence of Hall resistivity for (a) $Mn_{3.03}Sn_{0.97}$ and (b) $Mn_{3.05}Sn_{0.95}$ samples at different temperatures. Temperature dependence of (c) Hall resistivity and (d) Hall conductivity for three samples. 67

3.8 Temperature dependent XRD patterns with Rietveld refinement for $Mn_{3.05}Sn_{0.95}$ samples at (a) 13 K, (b) 150 K and 300 K. 69

3.9 Temperature dependent XRD patterns with Rietveld refinement for $Mn_{3.03}Sn_{0.97}$ samples at (a) 13 K, (b) 150 K and 300 K. 70

3.10 Temperature dependent lattice parameters a and c for (a) $Mn_{3.05}Sn_{0.95}$ and (b) $Mn_{3.03}Sn_{0.97}$ sample. (c-d) shows the unit cell volume as a function of temperature for the two samples. 71

3.11 Temperature dependent ZFC magnetization curves for (a-d) $Mn_{3.05}Sn_{0.95}$, (e-f) $Mn_{3.04}Sn_{0.96}$ and (g-h) $Mn_{3.03}Sn_{0.97}$ at different values of external pressure. 72

3.12 (a-d) Field dependent isothermal $M(H)$ loops for $Mn_{3.05}Sn_{0.95}$ sample at 100 K and 300 K under application of different external pressure. The low field region of $M(H)$ data is shown in (c-d) for both temperatures. 73

3.13 (a-b) Field dependent Hall resistivity for $Mn_{3.05}Sn_{0.95}$ sample at 100 K and 300 K under application of different external pressure. (c-d) Temperature dependent zero field longitudinal resistivity measured at 0 GPa and 1.5 GPa pressure for $Mn_{3.05}Sn_{0.95}$ sample. (d) The magnified view around the pressure induced transition. (e-f) Pressure dependent lattice parameters and unit cell volume for $Mn_{3.05}Sn_{0.95}$ sample. 74

3.14 A schematic of the kagome lattice structure of Mn_3Sn showing three nearest neighbor (a) intra-plane and (b) inter-layer exchange parameters. The number of nearest neighbor for Mn atoms are represented in (c) for J_1^{out}, (d) J_2^{out} and (e) J_3^{out}. The arrows indicate the direction of magnetic moments. 77

3.15 (a) Phase diagram of minimum energy θ value as calculated for various values of exchange J_2^{out} and J_3^{out}. The curves corresponding to purple and green star are shown in (b) and (c) respectively. 78

3.16 The crystal lattice of Mn_3Sn with an (a) ideal kagome lattice, and (b) trimerized lattice. The lengths of two corner sharing triangles are marked. (c) The number of neighbors corresponding to the spitted J_2^{out} are shown by gray and red lines joining the Mn sites. 80

3.17 (a) Phase diagram of minimum energy θ value as calculated for various values of exchange J_2^{out} and J_3^{out} for the ideal kagome structure. (b-f) J_2^s and J_2^l phase diagram of minimum energy θ for the trimerized structure at different J_3^{out}. 81

3.18 Spin spiral calculated energies as a function of q for different condition of the Mn_3Sn unit cell. 83

3.19 Spin spiral energies (green symbols) and the fitting (purple line) with eq. 3.3 for 0 GPa (a) ideal and (b) forced lattice structure. 85

4.1 XRD patterns with Rietveld refinement for the polycrystalline (a) $Mn_{2.7}Fe_{0.3}Sn$, (b) $Mn_{2.5}Fe_{0.5}Sn$, and (c) $Mn_{2.3}Fe_{0.7}Sn$ samples. Some high intensity peaks are labeled in (a). The legends for the first three plots are shown in (b). (d) XRD pattern as recorded for the (001) face of single crystal samples. 89

4.2 Recorded EBSD patterns for (a) $Mn_{3.09}Sn_{0p91}$, (b) $Mn_{2.7}Fe_{0.3}Sn$ and (c) $Mn_{2.5}Fe_{0.5}Sn$ samples. 91

4.3 The FESEM images and corresponding EDS results for $Mn_{3-x}Fe_xSn$ samples. 92

4.4 Temperature dependent ZFC and FC $M(T)$ curves for (a-b) $Mn_{3.09}Sn_{0.91}$, (c-d) $Mn_{2.7}Fe_{0.3}Sn$ and (e-f) $Mn_{2.5}Fe_{0.5}Sn$ samples measured in two different orientations. The left column shows measurements for fields applied along the c-axis, and the right column shows data for fields perpendicular to c-axis. 93

4.5 (a) ZFC and FC $M(T)$ plots for polycrystalline $Mn_{2.3}Fe_{0.7}Sn$ sample. The inset shows zoomed in view of the Neel temperature. (b) Fe doping dependence of spin reorientation transition temperature T_{SR} and magnetic ordering temperature T_N. 94

4.6 Field dependent isothermal $M(H)$ loops for (a-b) $Mn_{3.05}Sn_{0.95}$, (c-d) $Mn_{2.3}Fe_{0.7}Sn$ and (e-f) $Mn_{2.5}Fe_{0.5}Sn$ samples at various temperatures. The left column shows measurements for fields applied parallel to c-axis, and right column shows data for $H \perp c$-axis. 96

4.7 (a) Schematic of the proposed model of spin reorientation transition for the hexagonal Mn_3Sn. (b) The triangular lattice site with two large Mn and one smaller Fe moment. 98

4.8 (a) Simulated neutron diffraction data for different out-of-plane canting angles. ND data at different temperatures for (b) (201) and (c) (200) reflections. (d) Temperature dependent area of the (201) and (200) peaks as evaluated by a Gaussian fitting of the peaks. 100

4.9 Neutron diffraction data with Rietveld refinement at different temperatures for $Mn_{2.5}Fe_{0.5}Sn$ sample. (a) The 350 K data with only structural fit. (b) The ND data at 300 K fitting with iT-AFM structure. (c) The fitting of 10 K data with canted iT-AFM structure. 101

4.10 Fitting of the 10 K ND data with and without canting. 2θ range for the (201) and (200) peaks is shown. 102

4.11 (a) Schematic of the high-temperature, in-plane iT-AFM state (left) and the canted low-temperature magnetic state (right). The green arrows represent the direction of the fictitious magnetic field generated by octupole order (left) and the non-coplanar canted state (right). (b) The SSC on a triangular unit as a function of out-of-plane canting angle. (c) The hexagonal structure with marked directions that are chosen as x and y for transport measurements. (d) 3D schematic of a rectangular shaped Hall bar showing the ρ_{xy} and ρ_{xz} measurement connections. 104

4.12 Field dependent ρ_{xz} component of Hall resistivity (left column) and Hall conductivity (right column) for (a-b) $Mn_{3.05}Sn_{0.95}$, (c-d) $Mn_{2.3}Fe_{0.7}Sn$ and (e-f) $Mn_{2.5}Fe_{0.5}Sn$ samples at different temperatures. 105

4.13 Field dependent ρ_{xy} component of Hall resistivity (left column) and Hall conductivity (right column) for (a-b) $Mn_{3.05}Sn_{0.95}$, (c-d) $Mn_{2.3}Fe_{0.7}Sn$ and (e-f) $Mn_{2.5}Fe_{0.5}Sn$ samples at different temperatures. 106

4.14 (a-b) AHE scaling plots for $Mn_{2.7}Fe_{0.3}Sn$ and $Mn_{2.5}Fe_{0.5}Sn$ samples. The scattered data points represent the experimental $\log(\rho_{xy})$ values and the line correspond to a linear fit of the data. The vertical grid line mark the spin reorientation transition temperature. (c-d) The $\log(\rho_{xy}/\text{SSC})$ plots for the two samples and a line corresponding to slope of 2. 109

4.15 (a-b) The measured and calculated Hall resistivity for (a) $Mn_{3.09}Sn_{0.91}$ and (b) $Mn_{2.7}Fe_{0.3}Sn$ sample at 5 K. The shaded region highlights the mismatch between two curves. 110

4.16 Picture of the Hall connection made to measure ρ_{xy} and ρ_{xz} component simultaneously. 111

4.17 The Hall measurements data to probe characteristics of dual order are plotted. Brown and green data corresponds to the ρ_{xy} and ρ_{xz} signal respectively. A schematic at top is shows the measurement protocol. See text for more details. 112

4.18 (a-c) The change in energy as a function of out-of-plane canting angle ϕ computed using the ab-initio calculation for $Mn_{3-x}Fe_xSn$ series of samples. The dotted lines are a guide to the eye. The calculations are for an ideal kagome lattice without trimerization. (d) The value of ϕ corresponding to the energy minima for different values of x. . . 114

4.19 The Heisenberg exchange and the different 4-spin higher order exchange interaction on kagome lattice. 116

4.20 (a) Schematic of the in-plane magnetic configuration considered. (b) Energy change as a function of canting angle Θ for a set of three coplanar spins for Heisenberg exchange and (c) for 4-spin exchange interactions. (d) Energy change plots for different values for 4-spin exchange added to the Heisenberg exchange. 117

4.21 The change in energy as a function of out-of-plane canting angle ϕ for 2-spin and 4-spin exchange interactions. 118

4.22 (a) Representation of the moment S_i on a coordinate system. (b-d) Different in-plane and our-of-plane 2-spin and 4-spin exchange interaction on the kagome lattice of Mn_3Sn. 120

4.23 Out-of-plane canting angle dependent change in energy and fitting with Eq. 4.12 for $Mn_{3-x}Fe_xSn$ series of samples. 123

4.24 Energy contribution for different order of exchange interactions by fitting the DFT data presented in Fig. 4.23. 124

4.25 (a-c) The change in energy as a function of out-of-plane canting angle ϕ computed using the ab-initio calculation for $Mn_{3-x}Fe_xSn$ series of samples. The dotted lines are a guide to the eye. The calculations are for an relaxed kagome lattice that exhibit finite trimerization. . . 125

5.1 Picture of the $3d$ row and some $5p$ elements of the periodic table. . . 127

5.2 Variation of lattice constants a and c with Sb doping for $Mn_3Sn_{1-x}Sb_x$ samples. 128

5.3 The FESEM images and corresponding EDS results for $Mn_3Sn_{1-x}Sb_x$ samples. 129

5.4 XRD pattern and Rietveld refinement data for the three samples of $Mn_3Sn_{1-x}Sb_x$ series. 130

5.5 ZFC and FC $M(T)$ measurements at an applied field of 1000 Oe for (a) $Mn_3Sn_{0.9}Sb_{0.1}$, (b) $Mn_3Sn_{0.8}Sb_{0.2}$ and (c) $Mn_3Sn_{0.75}Sb_{0.25}$. (d) Dependence of T_N and temperature of helical transition with Sb doping. 131

5.6 Room temperature normalized resistivity data for different samples of series $Mn_3Sn_{1-x}Sb_x$. 132

5.7 Field dependent Hall measurements at different temperatures for (a) $Mn_3Sn_{0.8}Sb_{0.2}$ and (b) $Mn_3Sn_{0.75}Sb_{0.25}$ sample. 133

Chapter 1

Introduction

This thesis concerns different magnetic ground state spin structures in magnetic materials. To be specific, the present thesis covers the stabilization mechanisms, observable properties, and potential use of different spin structures in spintronic devices. The well-known noble prize-winning phenomenon of giant magnetoresistance (GMR) shows the importance of the relative orientation of magnetic moments to achieve desirable properties.[1,2] In case of GMR, the alignment of the two magnetic layers separated by a non-magnetic spacer layer dictates the overall electrical resistance of the system. The magnetic moments of two magnetic layers can align either parallel or antiparallel depending on the the thickness of the non-magnetic layer.[3,4] It was observed that the resistance of such a system changes with the parallel or antiparallel arrangement of the spins, where parallel arrangement of magnetic moments leads to a low resistance state and the antiparallel orientation gives a high resistance state. Thus, by controlling the direction of magnetic moments, the resistance of a device can be efficiently controlled. Following the discovery of GMR, tunneling magnetoresistance (TMR) was observed in magnetic/insulating/magnetic multilayer systems, where the difference between the high and low resistance states was found to be extremely large.[5] The read heads in vastly used hard disk drives (HDD) use the TMR phenomenon for reading the information stored in magnetic bits.

From the TMR-based read heads to the magnetic domains-based HDD, most of the devices currently use ferromagnetic (FM) materials. However, with the increasing demand for high density and high speed storage devices, improving upon the current FM based techniques is challenging. Many inherent side effect of ferromagnets like the stray fields and fragility to the high external magnetic field limit their use in densely packed devices. On the other hand, the antiferromagnets with net-zero magnetic moments are free of these problems. Antiferromagnetic (AFM) materials are immune to external magnetic fields and do not affect a neighboring antiferromagnetic domain in a closely packed storage device. On top of that, antiferromagnets also show faster dynamic responses and can have nano-sized magnetic domains.[6] However, this innocuous behaviors of antiferromagnets make them invisible to traditional magnetic probing techniques, making it difficult to implement them in spintronic devices.

In this regard, non-collinear antiferromagnets present an excellent prospect akin to their non-trivial transport properties. One can find many exciting and complex AFM materials that show a variety of non-AFM-like responses. As exemplified in case of GMR/TMR, the relative orientation of magnetic moments can completely redefine the physical properties of a material. Thus the complex magnetic structures of the non-collinear antiferromagnets offer a limitless opportunity for the realization of desirable properties. The most important aspect of these non-collinear AFM state is the possibility of finding a better way to externally control them in comparison to the conventional AFM materials. This can only be achieved by fundamental understanding of different mechanisms that stabilizes these non-collinear AFM states. Thus the study of different physical properties of these complex magnetic states and understanding their underlying mechanisms is of utmost importance for the realization of low power, faster and smaller technological devices desired in the field of spintronics.

In the following a brief discussion is focused on various fundamental aspects of magnetic interactions that are being enforced in the present thesis work. In addition, a through literature survey is presented based on the main theme of the work carried

out in the present thesis.

1.1 Magnetic energy landscape: Exchange interactions

The stabilization of a magnetic ordered states can be understood through the minimization of energy contributing to the magnetic Hamiltonian. While discussing the magnetism of solid-state systems, the smallest unit of magnetic moment can be considered to be arising from an atom. The magnetic moment of the atom may arise due to the orbital motion or the intrinsic quantum mechanical spin angular momentum of the electrons. Different magnetically ordered states are in general stabilized as a result of the collective interaction among the magnetic moments of atoms in a crystal lattice. Similar to the interaction between two electric dipoles or two nearby current-carrying wires, two magnetic dipoles sitting close to each other also interact. This interaction is called the dipole-dipole interaction and can be written as,

$$H = -\frac{\mu_0}{4\pi|r^3|}[3(m_1.\hat{r})(m_2.\hat{r}) - m_1.m_2]. \tag{1.1}$$

Here μ_0 is the permeability of vacuum, r is the distance between the magnetic dipoles, m_1 and m_2 are the magnetic dipole moments of the two atoms and $\hat{r}$ is the unit vector pointing from m_1 to m_2. The dipole interactions can be substantial at a macroscopic level, but their comparative energy at microscopic scale is small. It is exemplified by the fact that the ordering temperature of most of the common ferromagnets can not be explained based on the strength of dipole-dipole interaction only. The dipole-dipole interaction is the weakest one among different magnetic interactions through which two spins in a solid-state lattice interact. Thus, let us first look at different interactions in magnetic materials that lead to the stabilization of magnetic ground states. Afterward, a detailed discussion on different magnetic states that are being stabilized by these interactions will be focused.

The exchange interaction is the primary force behind the stabilization of or-

dered magnetic states. Like the existence of mediators for the fundamental forces, the exchange interactions are also mediated by the motion of electrons in the lattice. Depending on the nature of the system, the exchange interaction can be of ferromagnetic or antiferromagnetic in nature. The exchange Hamiltonian can be written as,

$$H = -J_{ij}(S_i.S_j), \tag{1.2}$$

where J is the exchange strength constant and S_i and S_j are spin magnetic moments at the ith and jth sites. The exchange interactions can broadly be divided into two categories: the direct exchange and the indirect exchange.

1.1.1 Direct Exchange

The simplest and most fundamental form of exchange interaction is the direct exchange. This kind of exchange arises when the orbitals of two neighboring ions directly overlap with each other. During such overlapping, the spin part of the system can either exist in the triplet state or in the singlet state. The singlet state with antiparallel orientation of the spins minimizes the total energy of the system against the electrostatic force. Thus, an antiferromagnetic exchange develops between the magnetic moments of atoms. Direct exchange, although looks fundamental but is seldom observed in real systems. The actual systems mostly show the exchange interactions of indirect nature.

1.1.2 Indirect Exchange

The indirect exchange can be of different types, but all are a results of the motion of the electrons in the crystal lattice. It is well known that the energy of an electron in a 1-D box is inversely proportional to the length of the box. Similarly, an electron on a lattice site tries to move to other lattice sites to 'increase' the length of the box to which it is confined. By doing so, it lowers the kinetic energy, a process called hopping. The hopping of the electrons from site **A** to site **B** is possible only under

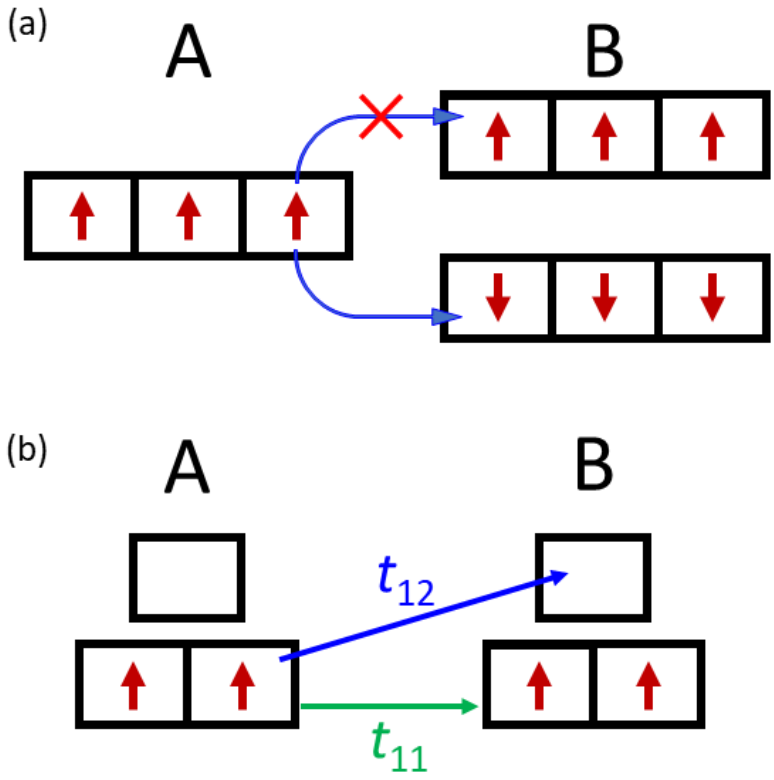

Figure 1.1: Schematic representation of possible hopping scenarios of electrons in two sites 'A' and 'B'. (a) Hopping on a half filled three degenerate energy levels. (b) Hopping parameters on two sites with split energy levels.

two circumstances. 1. The target orbital at site **B** is completely empty. 2. The unpaired electrons in the site **B** exhibit an opposite spin alignment to the spin of the electron at site **A**. This restriction is a direct consequence of Pauli's exclusion principle. Let us consider a simple example of a system with three degenerate energy levels at sites A and B [Fig. 1.1 (a)]. We first consider half-filled orbitals with three unpaired electrons. Now, if the electron spins at each site points in the same direction, it is apparent that the electrons can not hop to the following sites, as hopping preserves the direction of the electron spin. Thus, the spins at sites **A** and **B** must align oppositely for the hopping to occur. Hence, this process leads to an antiferromagnetic exchange. Now, let us consider a system as shown in Fig. 1.1 (b), with three orbitals and two electrons at each site. In this case, the nature of exchange will depend on the strength of the hopping parameter t. If t_{11} is

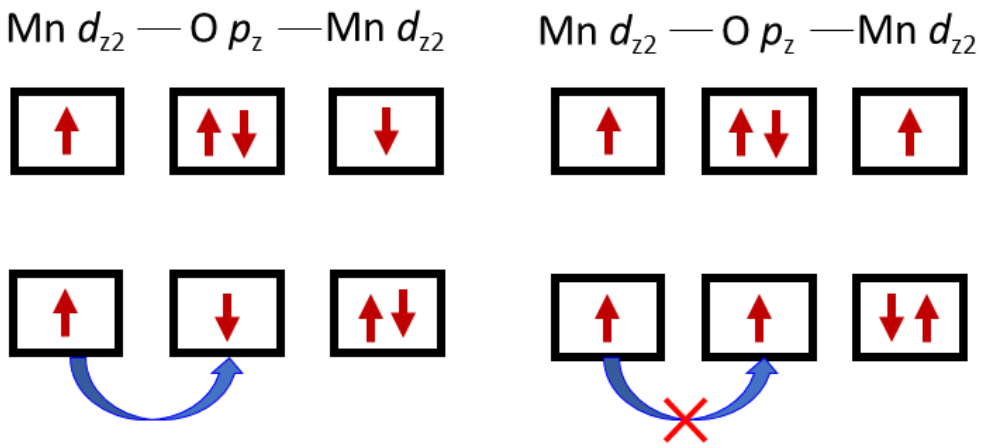

Figure 1.2: Schematic of superexchange mechanism leading to an antiferromagnetic exchange between two Mn atoms.

substantially stronger than t_{12}, then again, antiferromagnetic exchange is preferred. On the contrary, when t_{12} is stronger, a ferromagnetic exchange is possible. In physical system, the indict exchange appears mostly as superexchange and double exchange.

1.1.2.1 Superexchange

In this type of exchange, the interaction between two magnetic moments may occur through a non-magnetic atom.[7] An example of this type of exchange is the stabilization of antiferromagnetic order in MnO, where two Mn atoms are separated by a significant distance; thus, a direct hopping of electrons is not possible. The hopping between d orbitals of Mn atoms is facilitated through the p orbitals of the oxygen atom. Figure 1.2 shows the schematic diagram of the superexchange process. When the two electrons at two different Mn ions align antiferromagnetically, the electrons can easily hop between different sites. On the other hand, for a ferromagnetic alignment, electron hopping is forbidden. Thus, a robust antiferromagnetic exchange is stabilized.

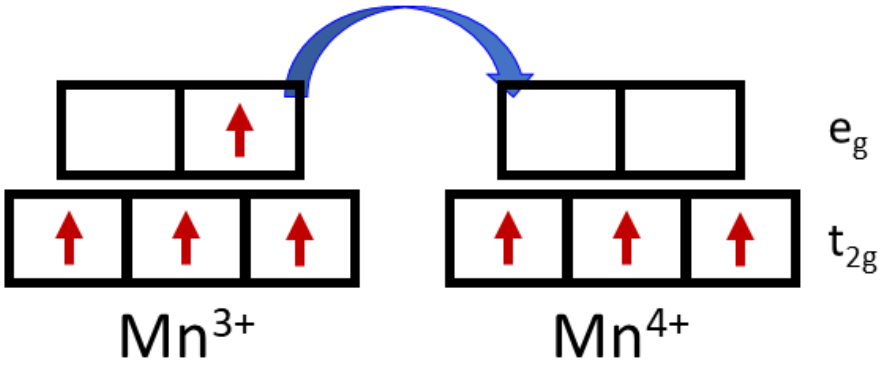

Figure 1.3: Energy level schematic of double exchnage interaction between two Mn atoms with different oxidation states.

1.1.2.2 Double exchange

The double exchange phenomenon occurs in magnetic systems where mixed valency of the same magnetic ion is present. The double exchange interaction is also a type of superexchange, but the presence of the same ion with two different oxidation states leads to a modification of exchange interaction. The double exchange was proposed by Zener in $La_{1-x}Sr_xMnO_3$.[8] $LaMnO_3$ and $SrMnO_3$ are antiferromagnetic insulators, with Mn having an oxidation state of 3+ and 4+, respectively. The antiferromagnetic exchange in the end compounds is mediated by superexchange and can be understood from the Fig. 1.2. It is clear that for Mn atoms with the same oxidation state, oxygen-mediated antiferromagnetic coupling is possible. Now, for the Sr doped $LaMnO_3$, the Mn ions exist in both the 3+ and 4+ oxidation states. This scenario is represented as energy levels in the Fig. 1.3. The extra electron from the Mn^{3+} site can easily hop to the corresponding empty level on the Mn^{4+} ionic site. However, due to strong Hund's coupling between e_g and t_{2g} electrons, it is not energetically favorable for the electron to hop to an e_g orbital where the t_{2g} are aligned oppositely. Thus the ferromagnetic exchange is the dominant exchange interaction in this case and the earlier insulating antiferromagnetic state transforms to a conducting ferromagnetic state.[9,10]

1.1.3 Asymmetric or chiral exchange

All the exchange interactions discussed in the previous sections can be modeled with the same Heisenberg exchange Hamiltonian with the dot product of magnetic moments at two sites (eq. 1.2). Hence, the exchange interaction is symmetric with respect to an interchange of magnetic moments between two sites as $(S_i.S_j) = (S_j.S_i)$. For asymmetric exchange interactions, the interchange of magnetic sites leads to a change in the sign of the energy term. The asymmetric exchange is also a manifestation of the processes described above in section 1.1.2, but with an added effect of spin-orbit coupling (SOC).[11] The spin-orbit coupling controls the normal hopping of the electrons to the excited state of the system and leads to an exchange term that is vectorial. The Dzysloshnkii-Moriya Interaction (DMI) is a well-known example of such chiral exchange, which can be written as

$$H = -D_{ij}(S_i \times S_j). \tag{1.3}$$

.

While the Heisenberg exchange interactions lead to a parallel or anti-parallel arrangement of spins, the DMI interaction tries to align spins at 90° to each other. This interaction was initially found in antiferromagnet α-Fe_2O_3.[12] In Fe_2O_3, the strong antiferromagnetic exchange tries to align spins antiparallel to each other, whereas the DMI interaction prefers an angle of 90° between the two neighboring spins. This leads to a small canting of the spins from the 180° antiferromagnetic structure. The DMI plays an important role in the research related to the chiral magnetic textures. The DMI can only be found in systems with broken inversion symmetry.

1.1.4 Higher order exchange

The exchange interactions are mediated by hopping of electron between lattice sites. When we consider the Heisenberg exchange interaction, an electron hops from a site

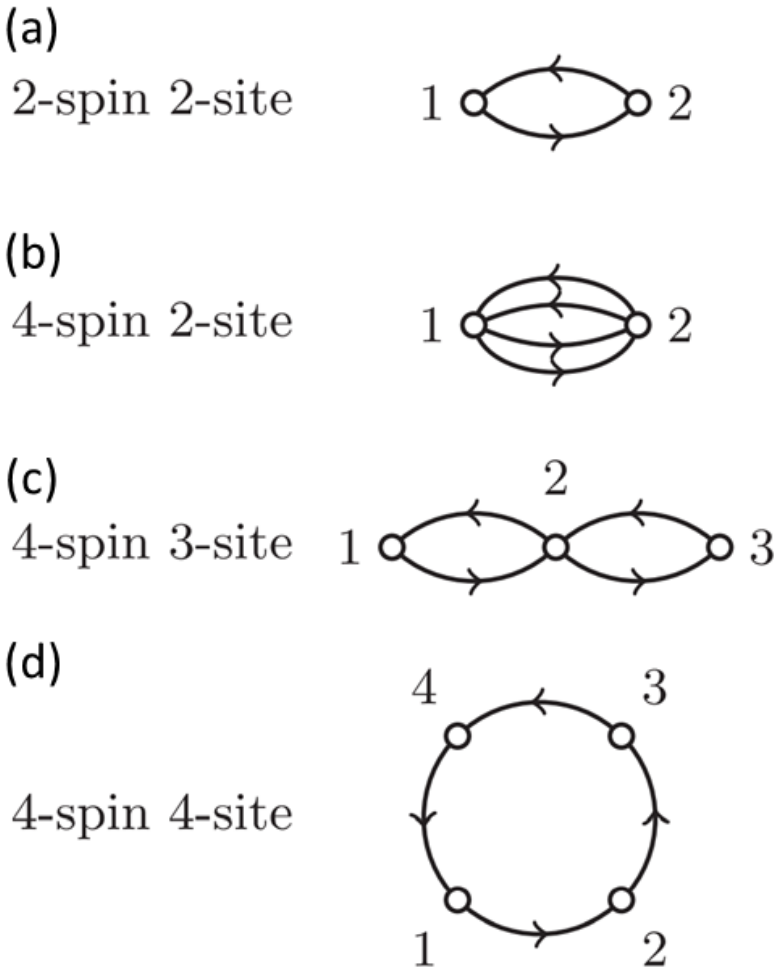

Figure 1.4: Schematic of 2-spin and different 4-spin exchange interactions.

i to j and then j to i. [Fig. 1.4 (a)]. In the $\frac{t}{U}$ expansion of Hubbard model, the strength of this interaction is proportional to $\frac{t^2}{U}$ ($\frac{t_{ij}^2}{U}$), where U is the on-site energy.[13,14] Although most of the magnetic ordered states can be explained by the Heisenberg exchange interactions, higher order exchange interaction are also permitted and can contribute in many materials.

These higher order terms involve multiple hopping of electrons, and can couple multiple spins at multiple sites. The most common addition are the 4-spin exchange interactions, whose strength in the $\frac{t}{U}$ expansion is proportional to $\frac{t^4}{U^3}$. Consider four sites on a square lattice as shown in fig. 1.4 (d). The process of hopping from and to the site '1' can be achieved in a ring manner. For this ring exchange case, the

electron makes four jumps around the lattice points sitting on a square/rectangular position. The exchange mediated in this case is brought about by four hopping, and information about four sites is included in this process. The strenght for this case is proportional to $\frac{t_{12}t_{23}t_{34}t_{41}}{U^3}$. This exchange process is called a 4-spin-four-site interaction.

The 4-spin exchange can further be present in the form of a 4-spin-two-site and 4-spin-three-site exchange. For the 4-spin-two-site interaction, the electron hops between two ionic sites twice [1.4 (b)]. This can only be possible when multiple energy levels are present on the ions, i.e. $S > \frac{1}{2}$ systems. The 4-spin-two-site exchange can be understood in detail from the fig. 1.5. Let us consider two sites with two energy levels. The hopping strength parameters t_{11}, t_{12} and t_{22} are as marked in figure. Now, if the strength of t_{11} is dominant over other hopping parameters, then an antiferromagnetic exchange is most viable. But, depending on the strength of other hopping parameters, the electron can hop between two sites following t_{12} —> t_{22} —> t_{12} —> t_{11}. This process is similar to the 4-spin-four-site ring exchange, but the double hopping takes place among two sites only. The strength in this case is proportional to $\frac{t_{12}^2 t_{22} t_{11}}{U^3}$. Similarly, the 4-spin-three-site exchange can take place through four hopping on three sites. Fig. 1.4 (c) shows the schematic of such 4-spin-three-site interaction. The strength of 4-spin-three-site interaction is proportional to $\frac{t_{12}^2 t_{23}^2}{U^3}$. Beyond 4-spin exchange, the 6-spin exchange can also exist in some materials.[15] The full Hamiltonian with 2-spin, 4-spin and 6-spin terms can be written as

$$\begin{aligned} H = &\sum_{ij} J_{ij}(S_i.S_j) + \sum_{ij} B_{ij}(S_i.S_j)^2 \\ &+ \sum_{ijk} Y_{ijk}[(S_i.S_j)(S_j.S_k) + (S_j.S_i)(S_i.S_k) + (S_i.S_k)(S_k.S_j)] \\ &+ \sum_{ijkl} K_{ijkl}[(S_i.S_j)(S_k.S_l) + (S_i.S_l)(S_j.S_k) - (S_i.S_k)(S_j.S_l)] \\ &+ \sum_{ijk} X_{ijk}(S_i.S_j)(S_k.S_l)(S_l.S_i). \quad (1.4) \end{aligned}$$

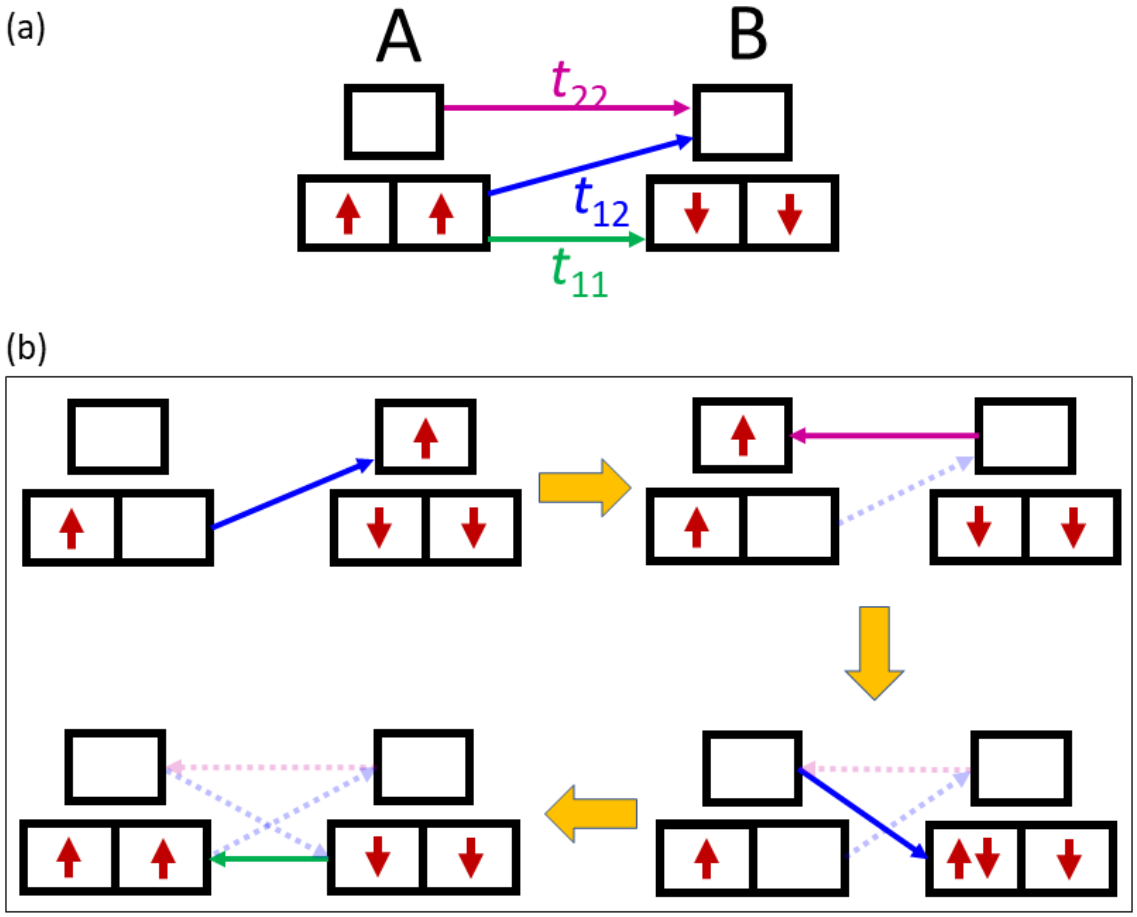

Figure 1.5: Energy level schematic of a model system with non-degenerate energy levels. The hopping parameters for different possible hopping are marked (left). Multi hopping process leading to a 2-spin-two-site bi-quadratic interaction (right).

The B, Y, K and X are the strength parameters of different high order terms. Only the 6-spin-three-site form of 6-spin exchange is written in Hamiltonian 1.4. Other form of 6-spin exchange include two-site and a six-site ring exchange. A detailed mathematical analysis for these exchanges can be found in a report by Hoffmann et al..[16] In addition to the higher-order analog of the Heisenberg exchange, the higher-order analog of asymmetric exchange can also be found.[17]

1.2 Magnetically ordered states

1.2.1 Collinear magnetic states

Now that we have discussed different magnetic exchange interactions, let us look at possible magnetically ordered ground states that can be stabilized by one or a combination of these interactions. The most common magnetic orderings that we come across are the ferromagnetic and antiferromagnetic states. The basis of the ferromagnetic/antiferromagnetic states, which can be described as collinear magnetic alignment, is the manifestation of sign of the exchange constant J as given in Equation-1.2. In the simplest case, where the exchange exists between the nearest neighbors, a positive/negative sign of the exchange constant J leads to the ferromagnetic/antiferromagnetic (Fig. 1.6) ordering. In this case, the ordering temperature depends directly on the strength of J. Beyond these simple collinear magnetic ground states, more complex arrangement of the magnetic spins can also be possible in magnetic materials. The main work of this thesis is focused on these complex magnetic ground states. A comprehensive understanding of these noncollinear magnetic ground state is discussed below.

1.2.2 Noncollinear magnetic states

1.2.2.1 Exchange frustration

Now lets consider a situation where the exchange constant J has contribution from both nearest neighbor exchange (J_1) and next nearest neighbor exchange (J_2). The introduction of the J_2 drastically affects the magnetic ground state of the system. Let us first consider the ferromagnetic ground state with positive J_1. If the J_2 is also having same sign, then the ferromagnetic state remains the ground state. However, for the case when J_2 is antiferromagnetic, the ferromagnetic ground state of the system is no longer compatible. Now depending on the relative strength of the J_2 and J_1, a noncollinear magnetic state can be stabilized. In some cases, a spin spiral

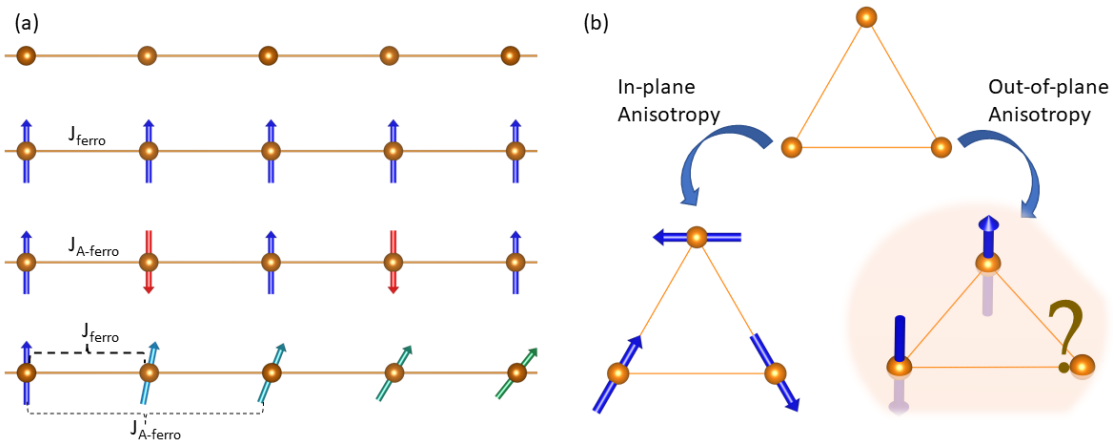

Figure 1.6: (a) A 1-D chain of atoms with possible magnetic states for different kind of exchange interactions. The exchange interactions between different sites are marked. (b) Ground state magnetic structure representation of a frustrated triangular lattice with in-plane and out-of-plane magnetic anisotropy.

state can also be stabilized where every spin orients with an angle θ to its nearest neighbor [Fig. 1.6 (a)]. The relative angle between the neighboring spin in this case is given by the minima of $-J_1 cos(\theta) + J_2 cos(2\theta)$. Similarly, an antiferromagnetic J_1 with an antiferromagnetic J_2 can also lead to a frustrated magnetic state. In an equivalent manner the exchange frustration can also arise in case of 2D lattices with multiple exchange parameters and without a unique collinear magnetic state. Besides the spin spirals, the exchange frustration also leads to canted magnetic spin structure in many materials, where different magnetic sublattices orient with an angle to each other.

1.2.2.2 Geometrical frustration

In some cases the geometry of the crystal lattice of a system dictates the nature of the magnetic ordering. In particular, the triangular lattice geometry leads to the stabilization of frustrated magnetic states in magnetic system with magnetic atoms sitting at the corner of triangle. A ferromagnetic exchange between the magnetic moments always leads to the stabilization of ferromagnetic order state. On the other hand, a unique ground state can not be found if the nearest neighbor exchange

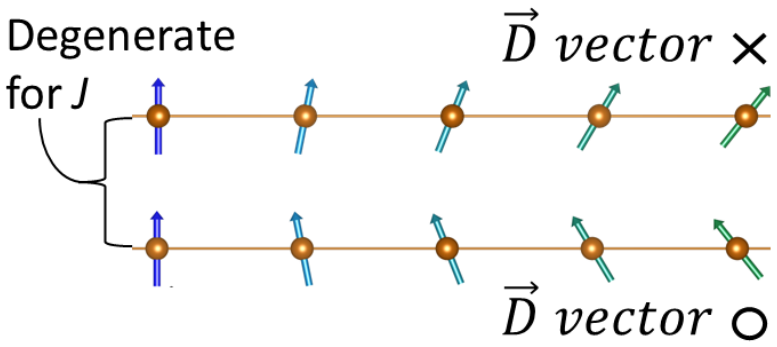

Figure 1.7: Spin spirals of different handedness along with the direction of DMI vector for minimum energy in each state .

interaction is antiferromagnetic in nature. As depicted in the Fig. 1.6 (b), when two nearest spins point in opposite direction, then there is no unique direction along which the third spin may align to minimize the energy. Such a scenario is termed as geometric frustration. For a geometrically frustrated system, a unique ground state is only possible with an easy plane anisotropy. In this case, the minima in energy is found when the magnetic moments align at an angle of 120° to each other. The 120° triangular spin structure is shown schematically in Fig. 1.6 (b).

1.2.2.3 Non-trivial spin structures stabilized by DMI

Another way to stabilize a canted magnetic state is the presence of DMI. As discussed in the section 1.1.3, the DMI interaction tries to align two magnetic moments at an angle of 90°. Hence, the competition between the DMI and the Heisenberg exchange can lead to a canted structure or spin spiral. The canted magnetic state induced by DMI is generally found in case of antiferromagnetic samples. In ferromagnetic materials, the competition of these two energies leads to a spin spiral structure in most of the cases. In general, the energy contribution of DMI is smaller than that of exchange interaction. Thus the length of the spin spirals stabilized by the DMI is larger than that set by the exchange frustration. Moreover, the magnetic states stabilized by the DMI exhibit a well-defined handedness due to the vector product form of the DMI. As shown in the Fig. 1.7, the spin spiral stabilized by the

exchange frustration can have both left-handed and right-handed sense of rotation as the ground state. In the two spirals shown in this figure, spins rotate clockwise in the top spiral and anticlockwise in the bottom. These two spirals are degenerate states when looked at from the perspective of the Heisenberg exchange. The DMI lifts this degeneracy between left and right-handed rotation and leads to a chiral spin spiral state. In general, the direction is shown by '$\times$' (into paper) and 'o' (out of paper) symbol. Due to the chiral nature, the DMI also stabilizes different types of topological spin textures, such as skyrmion[18,19] and antiskyrmions.[20,21]

1.2.2.4 Modification of magnetic structure due to higher order exchange interactions

The higher order exchange interaction include multiple hopping between same or different pair of spins. These interactions are generally weak and rarely observed in magnetic systems, hence are mostly neglected from a general magnetic Hamiltonian. Although their strength is usually small, but their effect can be dominant in some materials. Let's consider the Heisenberg exchange and 4-spin-two-site exchange as given below.

$$H_{2-spin} = J_{ij}(S_i.S_j) \tag{1.5}$$

and

$$H_{4-spin} = B_{ij}(S_i.S_j)(S_i.S_j) \tag{1.6}$$

Let's assume that the strength of pre-factor B is an order smaller than that of J. Consequently, for magnetic spin of unit length, the energy contribution due to the higher order also remains an order smaller con comparison to the Heisenberg exchange. However, for a system with larger magnetic moment, keeping the pre-factor same, the energy contribution due to the higher order interaction catches up with that of Heisenberg exchange. Even increasing the moment of size 4 units, the energy contribution due to the B exceeds that of J. Hence, the higher order interactions can also be of importance in systems with high magnetic moment.

To understand the effect of higher order interactions on magnetic states, let's look at the functional form of the 4-spin-2-site 'biquadratic' interaction. For Heisenberg exchange J, the minima in energy for a pair of two spins is obtained at either 0° or 180° alignment. But for the biquadaratic exchange interactions, the function $\cos^2(\theta)$ gives minima at 90° or leads to a degenerate state at 0° and 180°. Thus the presence of biquadaratic exchange interaction along with Heisenberg can give rise to unexpected ground states. Beyond the 4-spin-two-site interaction, multiple spins at different sites are involved and the ground state in those cases strongly varies from system to system. The most prominent feature associated with the 4-spin-three-site and 4-spin-four-site interactions is the stabilization of multi-Q spin spiral states.[22] These multi-Q states were recently observed in monolayer magnetic systems.[23,24,25] Figure 1.8 (a) shows the scanning tunneling microscopy (STM) image of a spin spiral stabilized by the exchange frustration on a Mn/W(001) lattice.[26] As we discuss earlier, the spin spirals stabilized by exchange interaction are degenerate with respect to the reversal of q vector. In addition, due to the crystal symmetry restriction, these spirals exhibits q vector direction along a set of symmetric points. The higher order exchange interactions can couple these different q spiral phases. For example, the three-site interaction couples two spirals with opposite q vector.[27] The resultant magnetic ground state is the sum of the two spirals, as shown in Fig. 1.8(b). The longitudinal component of the spins cancels each other and a magnetic state of the form *uudd* is stabilized.[28] Similarly, for Mn/Cu(111) system, a $3Q$ state is stabilized due to effects of higher order exchnage interactions.[23]

Table 1.1: Energy contribution for the 2-spin and 4-spin exchange with constant J and K with different values of magnetic moment.

	Energy	
S (a.u.)	$J\ (S_i.S_j)$	$B\ (S_i.S_j)^2$
1	0.1	1
2	4	1.6
3	9	8.1
4	16	25.6
5	25	62.5

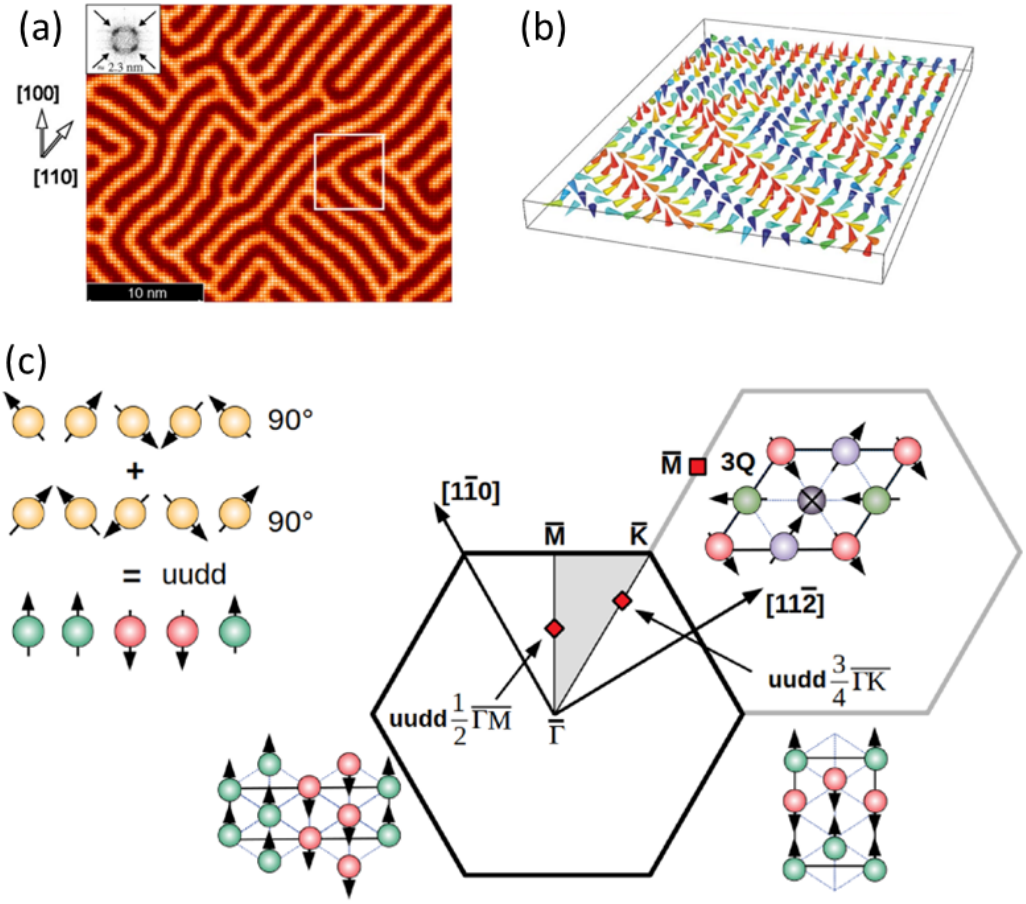

Figure 1.8: (a) scanning tunneling microscopy (STM) graph of spin spiral measured on Mn/W(001) lattice (top) and a spin schematic of same spiral state (bottom).[26] (b) Different multi-Q states in the Brillouin zone of a hexagonal system. Spin schematic for multi-Q state corresponding to different q values is also shown.[27]

1.3 Electrical transport of magnetic systems

It is well known that a charged particle moving in a transverse magnetic field experiences a Lorentz force in a direction orthogonal to both the velocity and the external magnetic field. To explore the possibility of a similar effect on the conduction electrons of a metal, E. H. Hall performed the transverse resistivity measurement in gold foil in 1879 (E. H. Hall did try other metallic materials before finally observing the effect in gold). The setup is shown in Fig. 1.9 (a), with current along x , magnetic field along z, and the measured voltage along y direction. A transverse signal

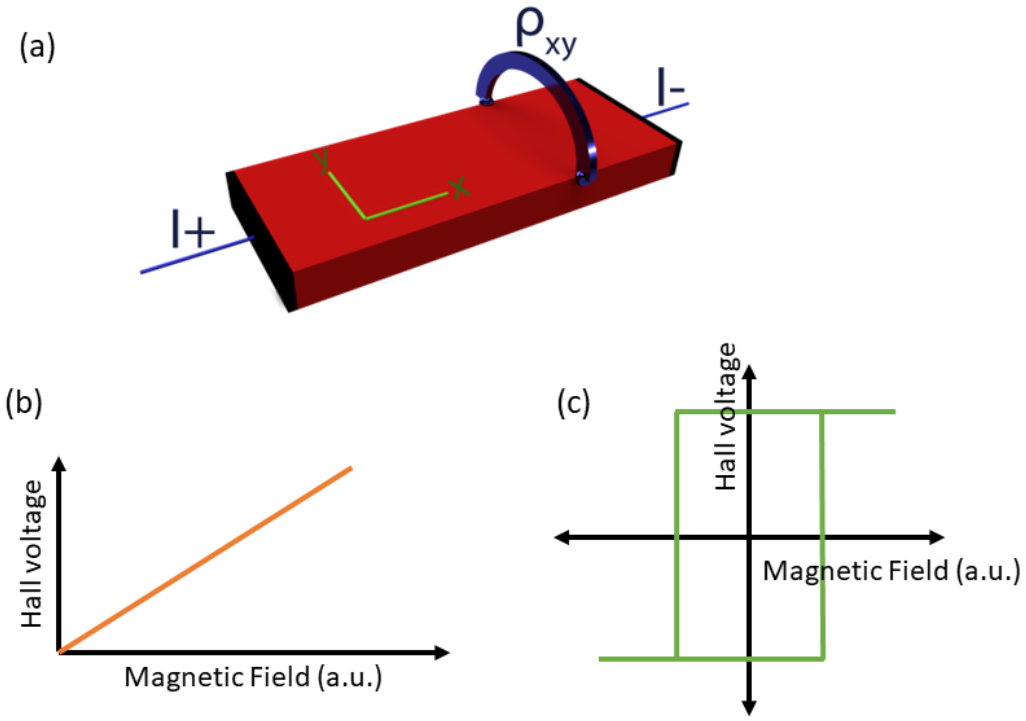

Figure 1.9: (a) Schematic of Hall voltage measurement setup. Plot of typical Hall voltage signal vs magnetic field for (a) ordinary and (b) anomalous Hall systems.

linearly proportional to the applied magnetic field was observed for the gold. This signal is a consequence of Lorentz force acting on electrons and was named the Hall effect. Mathematically, the Hall signal can be written as $\rho_{xy} = R_0 H$. Here R_0 is the Hall coefficient that is inversely proportional to the charge carrier concentration. The Hall signal is depicted in Fig. 1.9 (b). Two years later, Hall carried out the same experiment with ferromagnetic materials iron and nickel. He measured a transverse voltage signal with an order of magnitude larger than that was earlier found in nonmagnetic metals. This new Hall signal, which mimicked the hysteresis loop of the ferromagnetic material, was termed as anomalous Hall effect (AHE). The word "anomalous" was used as the origin of the effect was not known that time. A typical anomalous Hall signal is shown in Fig. 1.9 (c). A simple scaling analysis indicates that the anomalous Hall signal is directly proportional to the magnetization of the sample, with the proportionality constant being a material-dependent parameter. A natural and logical explanation was then followed, describing this effect as arising

due to the 'internal' magnetic field due to the ferromagnetic order of the samples. A more complex and detailed theoretical understanding of the anomalous Hall effect was materialized as time progressed. According to modern theories, the anomalous Hall effect can arise due to two different mechanisms. The first explanation is based on the introduction of the Berry phase. In this case, the anomalous Hall effect is a manifestation of the Berry phase that an electron picks up during its motion through magnetic materials. The second one is based on the spin-orbit coupling induced scattering of electrons. Based on these two mechanisms, the anomalous Hall contribution in various materials can be divided into two broad categories: *intrinsic* and *extrinsic*. The intrinsic component is the one that arises due to the 'intrinsic' properties of a periodic arrangement of atoms, i.e., a perfect crystal structure. Extrinsic contribution is mainly the effect of irregularities/defects in the crystal. Let us discuss these contributions in detail and also familiarize ourselves with the scaling laws governing different AHE contributions.

1.3.1 Intrinsic contribution

Intrinsic refers to the contribution from the crystal lattice itself. In the condensed matter systems, the properties of the periodic crystal lattice can be described on the basis of momentum space band structure. In case of anomalous Hall effect, the intrinsic contribution refers typically to the Hall signal that arises due to the Berry phase acquired by electrons when they move in the periodic lattice. When an electron moves in a periodic potential, its state can be written in the form of Bloch function as given below.

$$|\Psi_{kn}\rangle = e^{ik.r}|u_{kn}\rangle \tag{1.7}$$

If the electron state changes adiabatically with time, then the nth eigenstate of H (t=0) evolves to a nth eigenstate of H (t=t), while picking a phase factor. The states at t are then given as :

$$\Psi_n(t) = e^{i[\theta_n(t)+\gamma_n(t)]}\Psi_n(t), \tag{1.8}$$

where $\theta_n(t) = -\frac{1}{\hbar}\int_0^t E_n(t)dt$ is the dynamical phase and

$\gamma_n(t) = \int_0^t \langle\Psi_n(t)|\frac{\partial}{\partial t}|\Psi_n(t)\rangle dt$ is the geometrical phase. This geometrical phase is referred to as the Berry phase. The Berry curvature then is given by

$$\Omega_n(k) = \nabla_k \times a_n(k) \tag{1.9}$$

where

$$a_n(k) = \langle\Psi_n(k)|\frac{\partial}{\partial k}|\Psi_n(k)\rangle \tag{1.10}$$

The Hall conductivity from the Berry curvature can be calculated as

$$\sigma_{xy} = \frac{e^2}{\hbar}\sum_n \int_{BZ} \frac{dk}{(2\pi)^d} f(\varepsilon_n)\Omega_{xy}(k) \tag{1.11}$$

Here, the integration of Berry curvature is taken over the whole Brillouin zone. The distribution of Berry curvature in the Brillouin zone of a crystal is constrained by the symmetries of the lattice. For a time-reversal invariant system, $\Omega_n(k) = -\Omega_n(-k)$. Similarly, the presence of inversion center leads to $\Omega_n(k) = \Omega_n(-k)$. Thus, if both time-reversal and inversion symmetries are present, the Berry curvature tends to zero at all points of the Brillouin zone. Breaking of inversion symmetry of lattice leads to a finite Berry curvature at different points of momentum space. However, the total sum over the whole Brillouin zone still goes to zero. A finite Beery curvature can be found when integrated over the whole Brillouin zone only upon breaking time-reversal symmetry. Hence, breaking time-reversal symmetry is an important pre-condition for the presence of anomalous Hall signal in a system. In a ferromagnetic system, the finite moment breaks the time-reversal symmetry. As a result, a finite anomalous Hall effect can be found due to the presence of non-vanishing Berry curvature.

The Berry curvature in the band structure of a material is connected to various points of the band structure. These are mainly close to the band-crossing points without spin-orbit coupling. It can be seen from the Fig. 1.10 (a) where the Berry

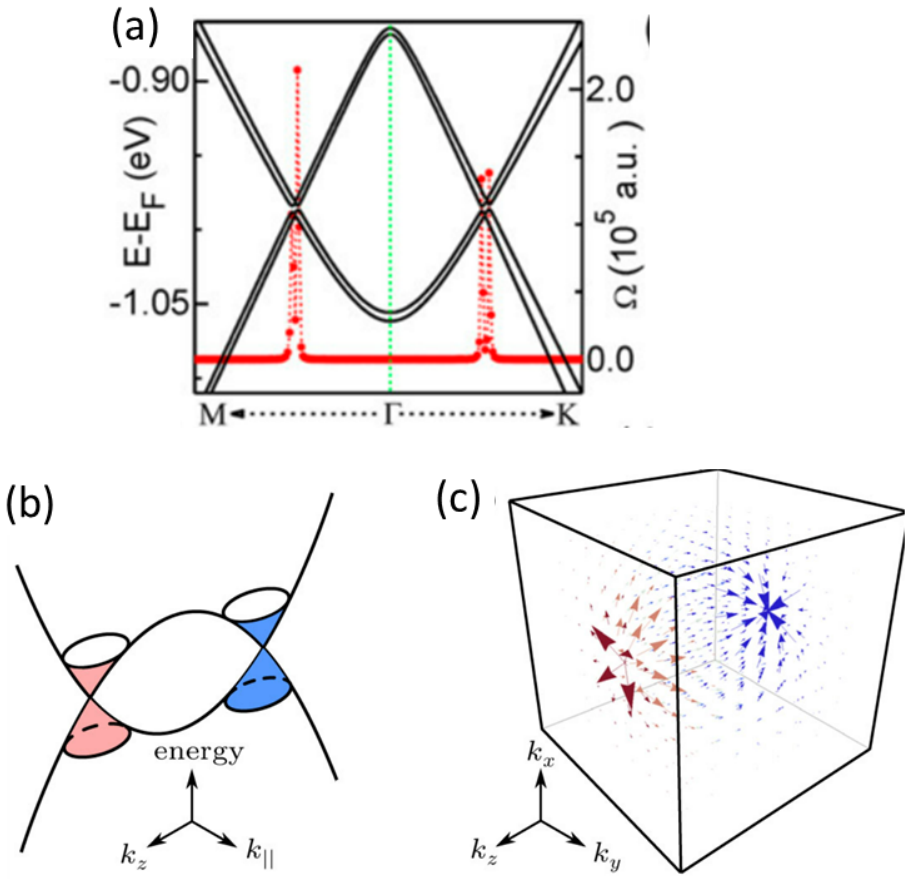

Figure 1.10: (a) Band structure of $RbMnCl_3$/graphene hetrostructure with band crossing points and corresponding Berry curvature.[29] (b) Schematic of a pair of Weyl points with opposite chirality. (c) The Berry phase originating form both points.[30]

curvature is highly localized at the band crossing points for $RbMnCl_3$/graphene hetrostructure.[29] Additionally, topologically protected band crossing points such as Weyl points also lead to a finite Berry curvature. The Weyl points are a pair of band crossing separated in momentum space. These crossing always appear as a pair [Fig. 1.10 (b)]. A pair of Weyl points act as source and sink of the Berry phase [Fig. 1.10 (c)] and impart an effective magnetic field to an electron.

1.3.2 Extrinsic contribution

In extrinsic contribution of AHE, the Hall signal arises due to the spin-dependent scattering at the defect sites of a material.[31,32,33] The extrinsic part further contains

two contributions: skew-scattering and the side jump phenomena. In case of skew scattering, the effective change in the crystal potential at the defect site leads to an effective magnetic field that deflects the electrons in an orthogonal direction. This effect depends on the electron transport lifetime τ and is not a dissipation-less current. In addition to the defects within a crystal, recent theoretical and experimental studies have also shown the appearance of skew-scattering contribution due non-coplanar spin structures,[34,35] which can act as a defect potential in a perfect lattice system. The skew scattering contribution is primarily observed in clean lattice systems, where the longitudinal conductivity of a sample is very high. Although the skew scattering is intrinsic to every materials, the effect is mainly observed for clean and high conductivity metals.[33] Another scattering like extrinsic mechanism is the side jump contribution, where a displacement of the Gaussian wave packet of electrons in the transverse direction happens upon encountering a defect in the crystal. The side jump mechanism is not commonly seen in magnetic materials, and its clear understanding remains unknown.

1.3.3 Scaling of anomalous Hall

The intrinsic as well as the extrinsic mechanisms of AHE can coexist in a material. Experimentally, the separation of intrinsic and extrinsic contribution is required to understand the underlying mechanism of AHE. The Berry phase induced intrinsic contribution is dissipation-less; the anomalous Hall signal for this case does not depend on the electron transport lifetime τ. On the other hand, the scattering-dependent contribution depends on time τ. This fact leads to distinct dependence of ρ_{xy}^{AHE} on the ρ_{xx}. For the intrinsic contribution, the $\rho_{xy}^{AHE} \propto \rho_{xx}^{2}$,[36,37] whereas for extrinsic part $\rho_{xy}^{AHE} \propto \rho_{xx}$.[31,32] Hence the total contribution due to intrinsic and extrinsic as a function of resistivity can be written as:

$$\rho_{xy}^{AHE} = a\rho_{xx} + b\rho_{xx}^{2} \tag{1.12}$$

Later, Tian et al.[38] presented a detailed relations as,

$$\rho_{xy}^{AHE} = a\rho_{xx_0} + \beta\rho_{xx_0}^2 + b\rho_{xx}^2. \tag{1.13}$$

Here the first two terms represent the extrinsic contribution in which aρ_{xx_0} is the skew scattering part, and the $\beta\rho_{xx_0}^2$ is due to the side jump. The last term corresponds to the intrinsic contribution. If we ignore the side jump term, the equation can be written as

$$log(\rho_{xy}^{AHE}) = \alpha log(\rho_{xx}). \tag{1.14}$$

$\alpha = 1$ implies extrinsic contribution and 2 suggest intrinsic contribution.[38]

1.4 Kagome lattice system Mn_3Sn

This thesis explores the non-collinear and non-coplanar magnetic ground states and their transport properties. As we discussed in the previous section, the non-collinear states can be realized by different mechanisms. However, a robust non-collinear ground state can be achieved through exchange or geometrical frustration. Spin structures stabilized by these effects can not be perturbed easily by the external magnetic fields. Thus, the geometrical frustration and exchange frustration cases are most suitable for studying the non-trivial magnetic states. In this regard, a triangular lattice structure is an ideal candidate to host the said phenomenon, as it can give both geometrical and exchange frustration. The kagome lattice antiferromagnetic compound Mn_3Sn presents an excellent prospect for studying complex magnetic states. Along with the advantages of being of an antiferromagnetic compound, Mn_3Sn displays many properties that are unique to its magnetic structure.

1.4.1 Crystal structure and magnetic ground state of Mn_3Sn

Crystal Structure : Let us first discuss the crystal structure of Mn_3Sn, where the kagome lattice consists of corner-sharing triangles and can be seen as a derivative of a triangular lattice with one of the lattice sites removed from the unit cell. The triangular lattice consists of four equal symmetric lattice positions in a unit cell, as depicted in Fig. 1.11 (a) with four different colors. The kagome lattice can be derived from this triangular lattice by removing any one of these lattice site. The resultant kagome structure is depicted in Fig. 1.11 (b). In the case of Mn_3Sn, the Mn atoms occupy the kagome lattice sites, while the Sn atoms sit at the vacant position of the kagome lattice, the extra position of the triangular lattice [Fig. 1.12 (a)]. In addition to this, each unit cell of the Mn_3Sn contains two layers of kagome lattice separated by half a unit cell distance. The two layers are rotated by 180° with respect to each other, as can be seen from Fig. 1.12 (a-b). Figure 1.12 (c) shows the resultant hexagonal Mn_3Sn structure generated by the combination of two rotated

layers. A side view of the structure is shown in Fig. 1.12 (d). The red Mn atoms lie in the bottom plane, whereas the blue are on the top plane. Each point in the upper layer is connected to a point in the bottom layer through the inversion center of the hexagonal unit cell. The atoms connected through the inversion center of sample are also depicted in Fig. 1.12 (d). The hexagonal unit cell of Mn_3Sn crystallizes in space group $P6_3/mmc$ with $a = b = 5.46$ and $c = 4.52$.

Magnetic Structure : The general magnetic ground state spin structure of a kagome lattice follows closely to that of a triangular lattice. A ferromagnetic Heisenberg exchange leads to a ferromagnetic structure for a monolayer kagome lattice, whereas an antiferromagnetc exchange leads to the geometrical frustration. To elucidate the exact magnetic structure of Mn_3Sn, neutron diffraction measurements were carried out by different authors.[39,40] It was found that Mn_3Sn exhibits a non-collinear triangular antiferromagnetic (T-AFM) structure,[39,40] a trademark of a geometrically frustrated systems. The magnetic moments in a T-AFM structure lie at 120° to each other. The antiferromagnetic nature of the nearest neighbor exchange and easy plane magnetic anisotropy leads to the stabilization of this T-AFM spin structure. The easy plane anisotropy of the sample results from the c/a <1. Let us look at the magnetic ground state and the exchange interaction of Mn_3Sn in detail. As the Mn_3Sn unit cell contains two kagome layers, the exchange parameters can be divided into two groups, intra-layer (J^{out}) and inter-layers (J^{in}). The two

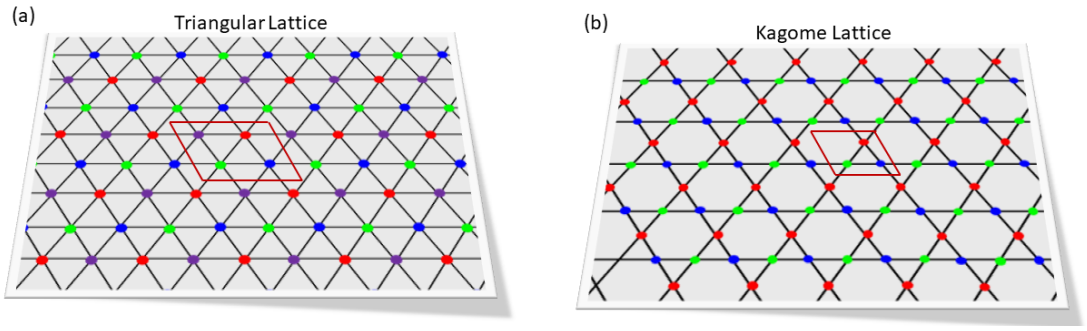

Figure 1.11: Schematic of a layer of (a) triangular and (b) kagome lattice. The unit cell for each lattice is marked with wine color. Different colors have been used to show lattice points in a unit cell.

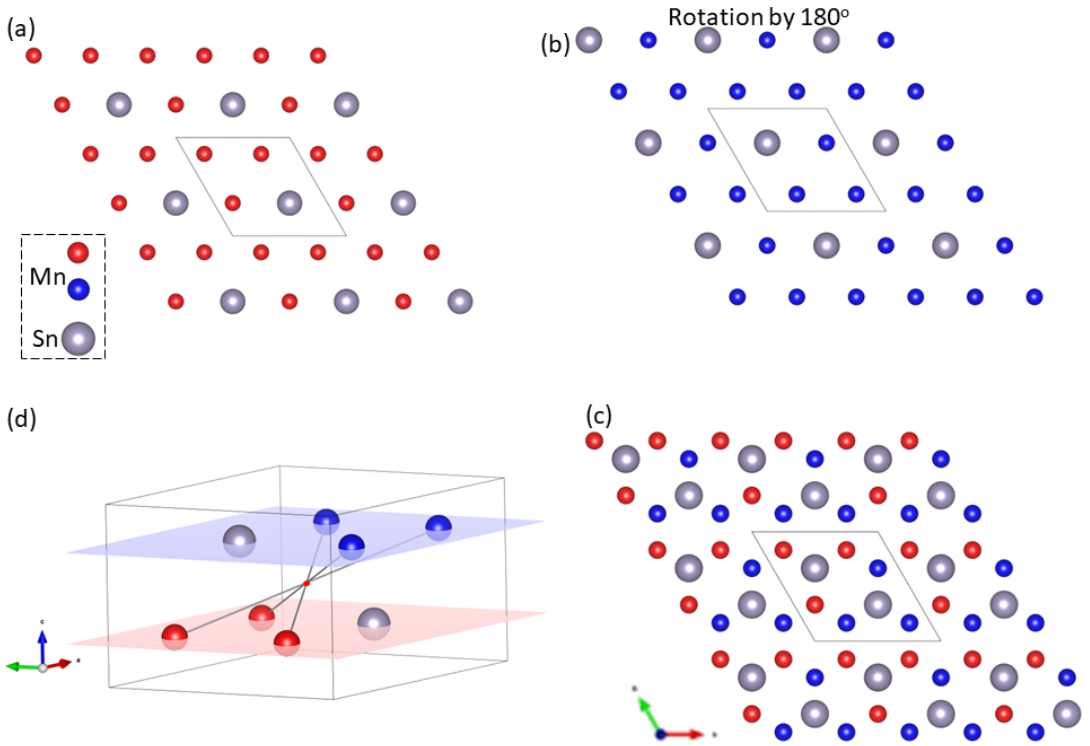

Figure 1.12: (a-b) Kagome with Sn at hexagon centres and a 180° rotates kagome lattice. (c) Mn_3Sn lattice made up of the two rotated kagome lattices. (d) Side view showing a shift along *c*-axis between two kagome layers.

nearest exchange interactions for both groups are marked in Fig. 1.13 (a-b). The nearest neighbor exchange interaction corresponding to the inter-layer exchange is marked as J_1^{out}. The inter-layer next nearest exchange interaction J_2^{out} is between two sites connected through the inversion center of unit cell. Both J_1^{out} and J_2^{out} are also shown in Fig. 1.13 (b). The nearest neighbor intra-layer J_1^{in} corresponds to the exchange in a spin triangle of the kagome lattice, while the J_2^{in} connects the larger triangle around the Sn site [Fig. 1.13 (b)].

It has been theoretically found that the in-plane nearest exchange ${J_1}^{in}$ as well as the second exchange constant ${J_2}^{in}$ are antiferromagnetic in nature,[41] which leads to the stabilization of 120° T-AFM ground state. The inter-layer ${J_1}^{out}$ and ${J_2}^{out}$ are found to be antiferromagnetic and ferromagnetic, respectively. The magnetic moments connected by ${J_2}^{out}$ point parallel to each other, which leads to a 120° angle between spins of ${J_1}^{out}$ pair. Thus, the overall T-AFM structure is stabilized

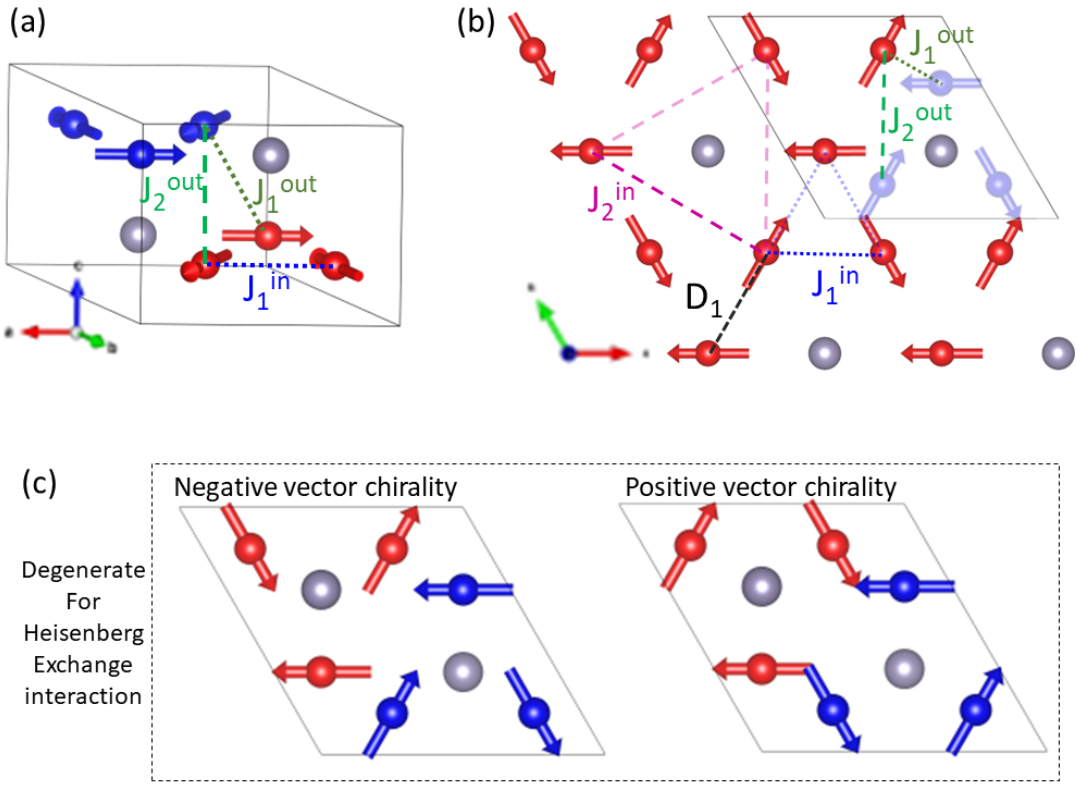

Figure 1.13: (a) Spin structure of Mn_3Sn sample where exchange parameters are marked by lines. (b) Extended Mn_3Sn lattice with various exchange interactions as marked by colored lines. (c) Degenerate triangular and inverse triangular spin structure stabilized by exchange frustration on layered kagome lattice of Mn_3Sn.

by a total of four exchange interaction. The resultant magnetic structure, as shown in Fig. 1.13 (a) and (b) preserves the inversion center of the underlying lattice structure.

Additionally, the 120° T-AFM structure stabilized in a geometrically frustrated kagome lattice consists of two degenerate spin structures. The 120° rotation of spins in either clockwise or anticlockwise fashion leads to two different magnetic states, as visible in Fig. 1.13 (c). This degeneracy can be lifted by the presence of DMI interaction between atoms corresponding to ${J_1}^{in}$. The DMI for Mn_3Sn is such that the magnetic structure exhibits an inverse vector chirality, i.e., rotation of spins in the opposite sense to the order of spins on the lattice. The magnetic structure with inverse vector chirality is named as inverse triangular antiferromagnetic structure (**iT-AFM**).

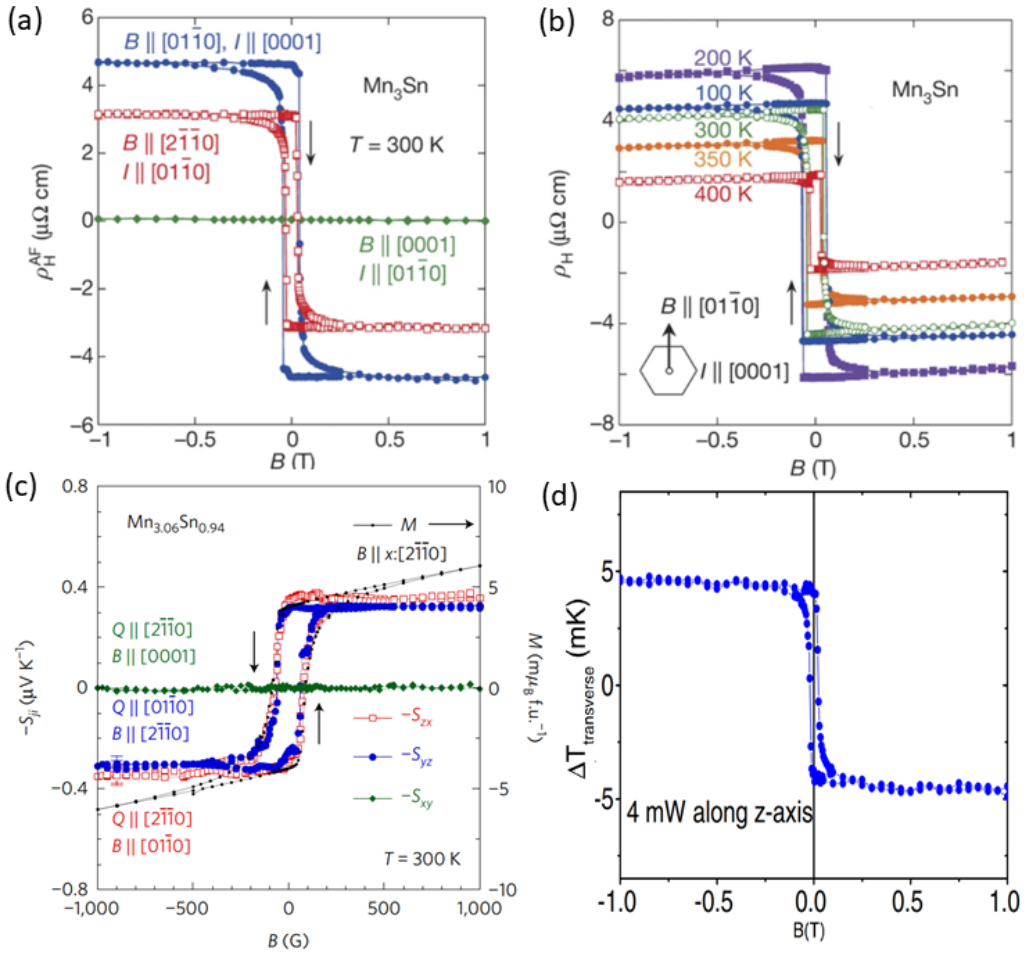

Figure 1.14: (a) Anomalous Hall signal as observed for Mn_3Sn at room temperature for fields applied along different directions. (b) Hall signal for field applied along [01$\bar{1}$0] direction at different temperatures.[42] (c) Anomalous Nernst signal measured in diffrent geometries.[43] (d) Thermal Hall effect signal for the Mn_3Sn samples at room temperature.[44]

1.4.2 Important aspects of iT-AFM structure in Mn_3Sn

Transport properties : Owing to the iT-AFM structure, the magnetic moment of the three Mn atoms sitting on a triangle cancel out each other, resulting in a net zero magnetic moment for Mn_3Sn. Thus, the sample is categorized as an antiferromagnetic material. The research interest in Mn_3Sn was redeveloped after the finding of a large anomalous Hall signal (AHE), despite being an antiferromagnet.[42] Figure 1.14 (a) shows the Hall resistivity measurements as performed on a single

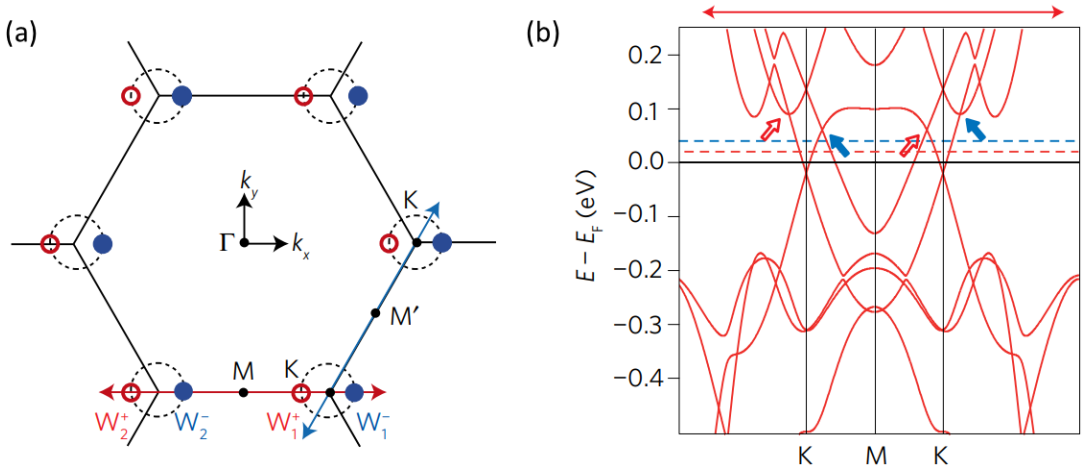

Figure 1.15: (a) Brillouin zone of Mn_3Sn showing a pair of Weyl points around K points. (b) Band structure along high symmetry points for Mn_3Sn. Blue and red arrows mark the Weyl points with opposite chirality. Figures taken form reference [45].

crystal of Mn_3Sn in different geometries.[42] A large anomalous Hall signal was observed when a magnetic field was applied in the *ab*-plane of the hexagonal structure. On the contrary, only a linear Hall signal of small strength is seen when the field was applied along the *c*-axis. The large anomalous Hall signal was found robust in a large temperature range [Fig. 1.14 (b)]. In addition to the large Hall signal, another transverse transport signature, the Nernst effect was also observed in Mn_3Sn.[43] In a Nernst setup, a temperature gradient or heat current is applied instead of a charge current. The resulting Hall voltage due to this heat current is called Nernst voltage. Figure 1.14 (c) shows the Nernst signal as a function of the magnetic field. Similar to the Hall signal, a large Nernst signal was seen when the magnetic field was applied in the *ab* plane. The Nernst signal converts the heat signal to an electric signal, thus making it possible to use Mn_3Sn in thermoelectric systems. Lastly, a thermal Hall signal can also be observed, where a heat current leads to a temperature gradient in the transverse direction. Figure 1.14 (d) shows the magnetic field dependence of thermal Hall effect at room temperature. All of these transport signatures closely mimic the magnetization v field [M (H)] measurements. The M (H) plot is shown in Fig. 1.14 (c) along with the Nernst signal. Both the curves reverses at the same

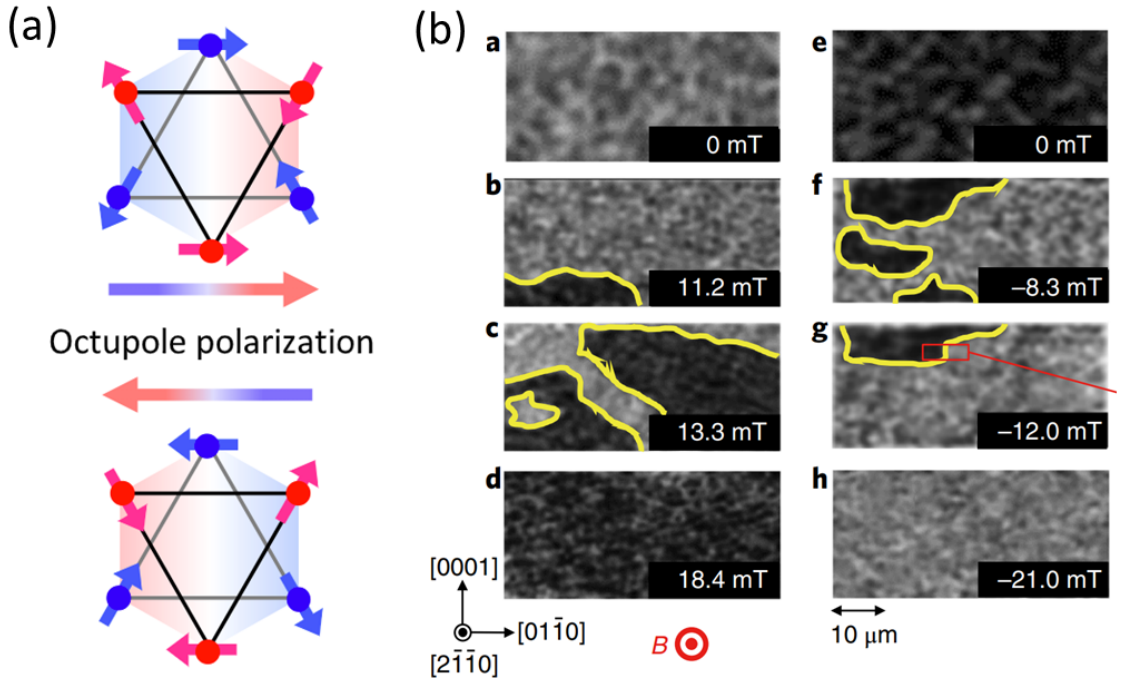

Figure 1.16: (a) Octupole polarization for different domains of iT-AFM structure of Mn_3Sn. (b) Magneto-optic Kerr effect (MOKE) images of Mn_3Sn thin films. Different contrast correspond to oppositely oriented octupole domains.[46]

point, thus suggesting that the observed transport signatures are a consequence of the magnetic structure of Mn_3Sn.

Band structure of Mn_3Sn : The above discussed transport signatures make Mn_3Sn a very compelling candidate for use in future spintronic devices. These transport properties mainly arise due to the iT-AFM structure of Mn_3Sn. As we learned in section 1.3, the Hall signal can be scattering-driven or intrinsic due to Berry phase effects. The former contribution normally arise for clean samples with high conductivity. Mn_3Sn does not display a high conductivity, hence a rich Berry physics can be expected. An analysis of band structure for the iT-AFM state revealed the presence of topological Weyl points in the non-collinear phase of the system [Fig. 1.15 (b)].[47] We can see two linearly dispersing Weyl crossing points around K point of the Brillouin zone. These Weyl nodes can act as source and sink of Berry curvature, which generates the large AHE signal. The orientation of these Weyl nodes was found to be easily rotated with the application of a magnetic

field. As shown by the dotted circle in Fig. 1.15 (a), the blue and red pair of Weyl points can rotate freely depending on the direction of applied magnetic fields. Thus, switching the magnetic field leads to reversal in the sign of anomalous Hall effect. The Weyl points generated by the linear crossing at K point are separated by small distance in the k-space, hence are not expected to play a major role in transport properties of sample.[48]

Octupole order : The Weyl nodes in a material are only formed when either the time-reversal symmetry or inversion symmetry is broken in a system. As discussed earlier, the iT-AFM state preserves the inversion symmetry of the lattice. Also, as Mn_3Sn is an antiferromagnetic material, the time-reversal symmetry is preserved due to zero magnetic dipole moment. Hence the question of satisfying the minimum condition to observe the AHE troubled researchers for a while. Then, Suzuki et al. proposed the presence of cluster multipole in the magnetic ground state of Mn_3Sn.[49] It was argued that even though the total dipole moment of the samples is zero, Mn_3Sn shows an cluster octupole moment due to the shifted layered nature of the unit cell. This octupole order reverses upon the reversal of magnetic dipoles, thus breaking the time-reversal symmetry of the sample, as shown schematically in Fig. 1.16 (a). The breaking of time-reversal symmetry due to the octupole order facilitates the observation of finite AHE in Mn_3Sn. The octupole domains have also recently been directly observed at room temperature.[46,50,51] Figure 1.16 (b) shows the polar Kerr rotation contrast of Mn_3Sn thin films. Similar to the domain structure of ferromagnetic material, octupole domains can be distinguished by the dark and bright contrast of the magneto-optic Kerr effect (MOKE) images. The bright area in the Fig. 1.16 (b) corresponds to octupole order with particular polarization, while the dark area corresponds to opposite polarization of the octupole domains. For the intermediate fields of positive and negative values, both dark and white contrast areas are visible. In the staurated state, the MOKE images show opposite contrast for the entire region.

In addition to the above-discussed properties, Mn_3Sn exhibits many more exciting properties. Some of these are listed below.

- Large magnet-optic Kerr rotation.[46]
- High damping of octupole moment.[50]
- Spin Hall effect (SHE) and inverse spin Hall effect.[52]
- Topological defects.[53]
- Topological hall effect[54,55]
- Planar Hall effect.[56]
- Chiral domain walls.[57]
- Terahertz anomalous Hall effect and Terahertz emission.[58,59]
- Kondo effect.[60]

Electrical switching : After the observation of above mentioned different properties in Mn_3Sn, the electrical manipulation of the magnetic state of Mn_3Sn was finally demonstrated in the year 2020.[61] Figure 1.17 (a) shows the schematic of the thin film structure of polycrystalline thin films of Mn_3Sn/X with X Pt, Cu, and W. It was found that the magnetic domains Mn_3Sn thin films can be switched by sending a current through the Pt layer. This effect is similar to switching ferromagnetic thin films upon injection of a spin current into the magnetic layer.[63,64] The spin current arises due to the spin Hall effect (SHE)[65] in the high spin-orbit coupling material Pt. Figure 1.17 (b) shows the Hall signal as a function of current applied to the thin-film system. It is visible that a switching of the Hall signal is only possible for the high spin-orbit coupling materials Pt and W. For the case of Mn_3Sn/Cu layer, the switching could not be seen. Also, the opposite sign of the Hall signal for the W and Pt layer suggests the SHE mechanism is the dominant force behind the switching of magnetic states. The demonstration of electrical switching signify the importance of Mn_3Sn for the perspective device applications.

To sum up, Mn_3Sn exhibits a non-collinear spin structure stabilized due to the geometrical frustration of the kagome lattice. Additionally, the double kagome

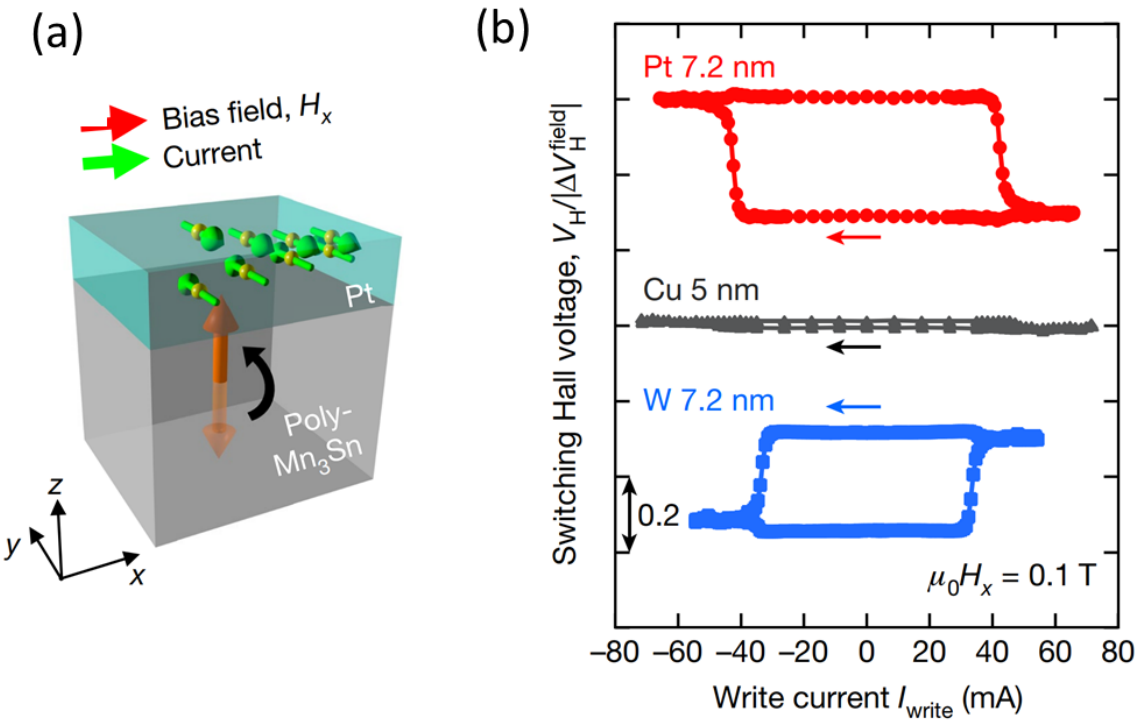

Figure 1.17: (a) Schematic of polycrystalline Mn_3Sn/Pt layer. The green arrows in Pt layer represent splitting of electrons of opposite spins due to spin orbit coupling. (b) Write current v. Hall signal plot fro difference Mn_3Sn/X films, where X = Pt, Cu and W. Figures taken from reference [61].

layered unit cell of Mn_3Sn stabilizes a cluster octupole order in the system. This octupole order breaks the time-reversal symmetry and leads to topological band structure. The combination of antiferromagnetic non-collinear state, octupole order, and non-trivial bands topology leads to fascinating properties in Mn_3Sn.

1.4.3 Open questions

The iT-AFM spin structure for Mn_3Sn has been studied in great detail at room temperature. The iT-AFM spin structure has been categorically established as the ground-state magnetic structure at room temperature for Mn_3Sn. This particular magnetic structure facilitates the presence of above discussed physical properties. An exciting development is the study of the temperature dependence of the iT-AFM structure. The observations presented in the literature for the temperature

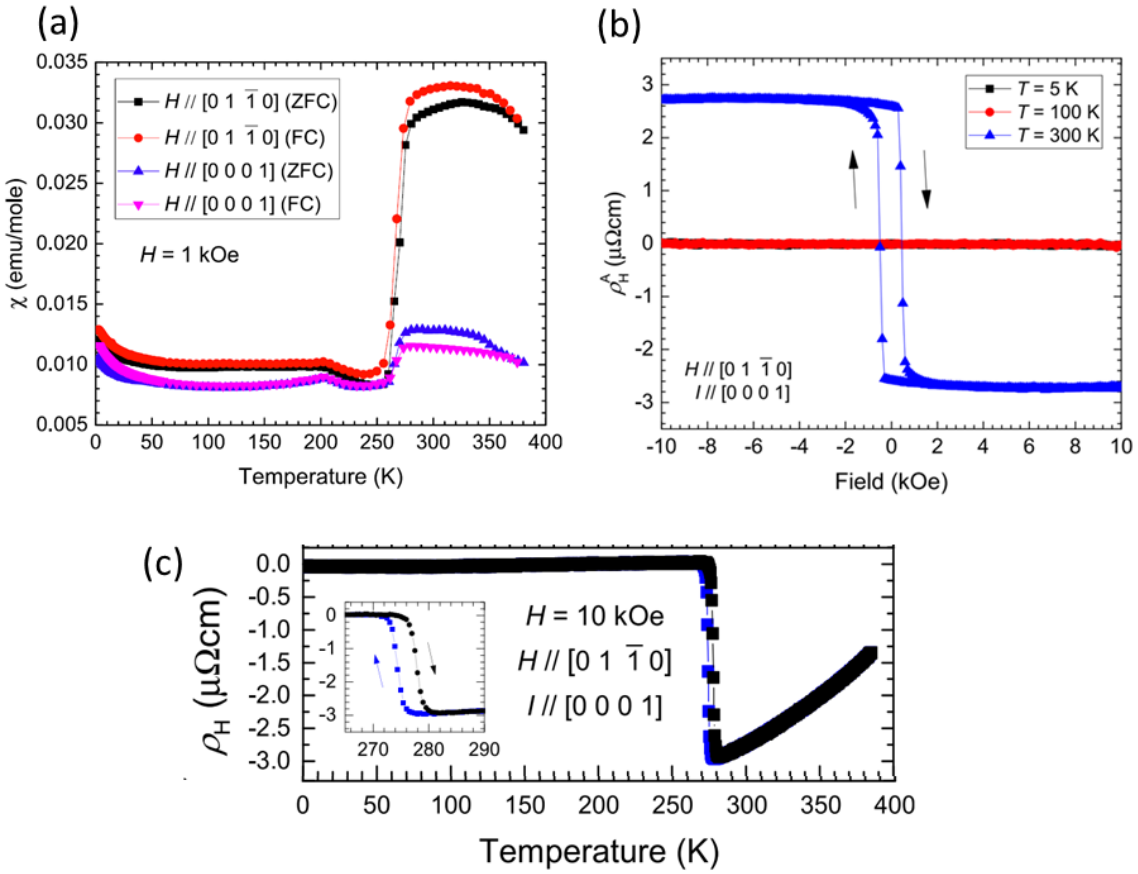

Figure 1.18: (a) Magnetization as a function of temperature plots under constant magnetic field for Mn_3Sn single crystals. (b) Hall resistivity measured as a function of magnetic field at 5K, 100K, and 300K. (c) Temperature dependence of Hall resistivity. All plots are taken from reference [62].

dependence of magnetic ground state are quite confusing and interesting. A literature survey broadly reveals two different trends in the temperature dependence of magnetization $[M(T)]$ in Mn_3Sn. A representative of first kind of M (T) plot, as reported by Sung et al., is shown in Fig. 1.18 (a).[62] The zero field cooled (ZFC) and field cooled (FC) $M(T)$ curves are plotted for fields applied along c-axis ([0 0 0 1]) and perpendicular to c-axis ([0 1 $\bar{1}$ 0]). For the field applied in the ab plane, it can be seen that the magnetization suddenly drops to a low value upon reduction in temperature to 250 K. Afterward, the magnetization stays at a low value up to the lowest temperature measured. The Hall signal measured at different temperatures for same sample is shown in Fig. 1.18 (b).

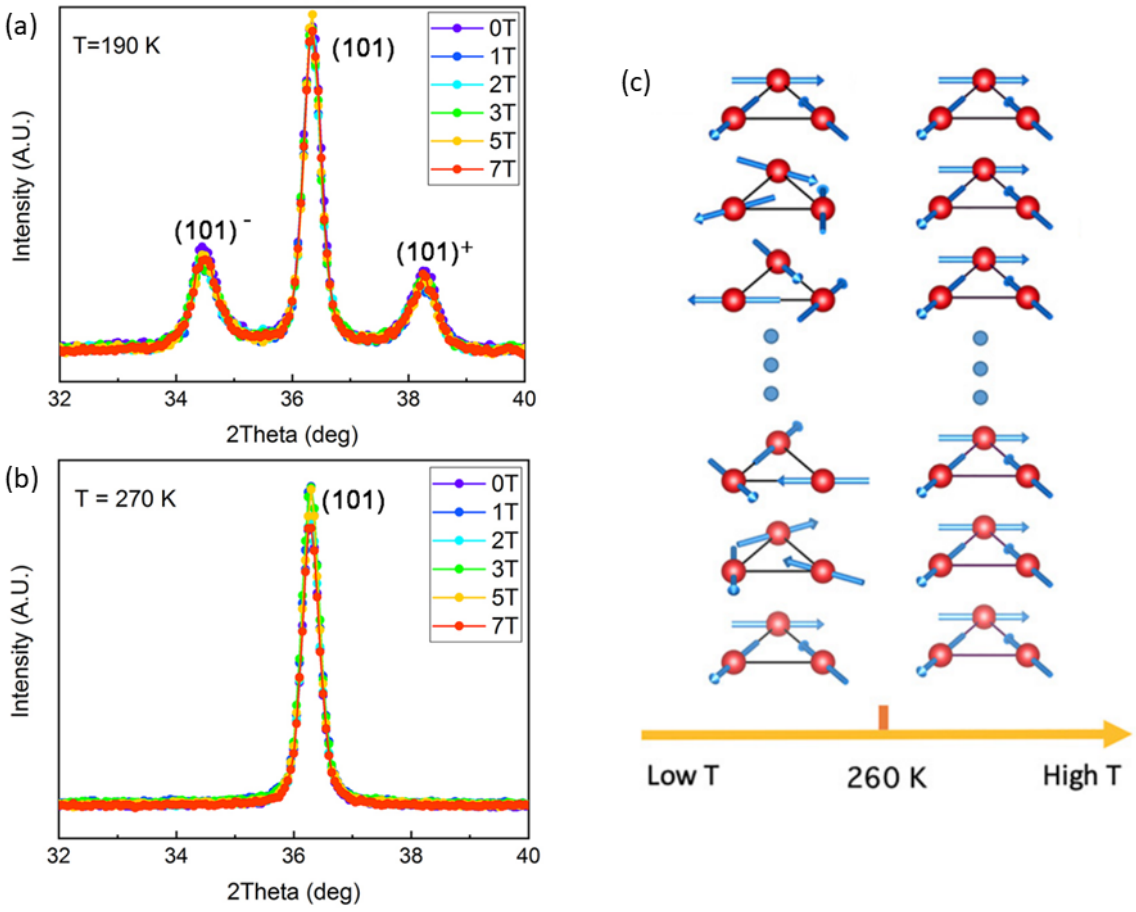

Figure 1.19: The neutron powder diffraction data for Mn_3Sn at (c) 190 K and (d) 270 K under different magnetic fields around (101) reflection. The satellite reflections $(101)^{\pm}$ are visible at 190 K. (c) A schematic representation of the iT-AFM and helically modulated magnetic structure. Plots are taken from reference [66, 67].

The large AHE is visible at room temperature, confirming the magnetic state as being iT-AFM. On the contrary, no Hall signal was found at temperatures below the sudden transition. Figure 1.18 (c) shows the Hall resistivity as a function of temperature. The Hall signal drops to zero at the temperature corresponding to this additional transition. Neutron diffraction studies have revealed that the transition to a low moment state corresponds to a helical modulation of the iT-AFM structure.[41,66] Figure 1.19 (a-b) shows the neutron diffraction data for Mn_3Sn sample below and above the sudden magnetic transition. At 270 K, the data around the (101) peak is shown. The (101) peak corresponds to the nuclear as well as magnetic

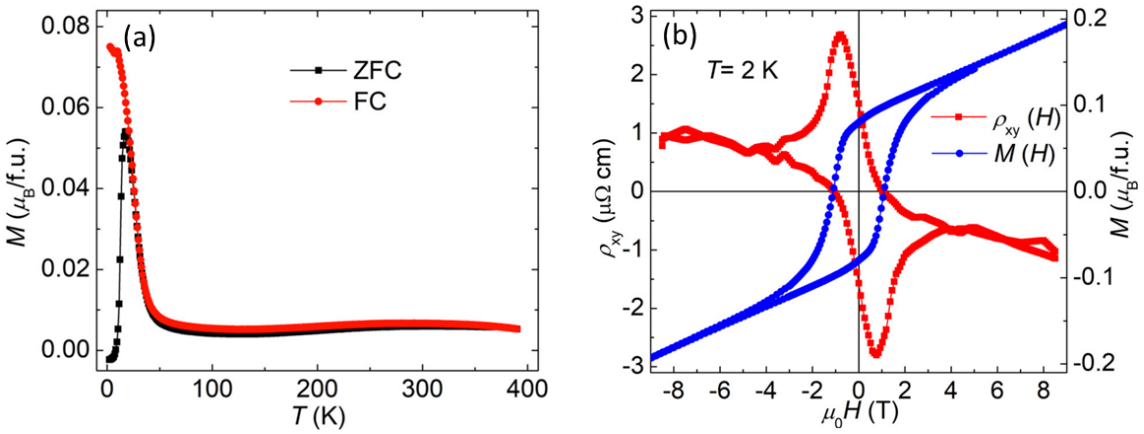

Figure 1.20: (a) Magnetization as a function of temperature plots under constant magnetic field for Mn_3Sn sample. (b) Magnetization and Hall resistivity measured as a function of magnetic field at 2K. Both plots are taken from reference [54].

reflections. Below the transition, it is clear that two satellite peaks arise around the (101) peak, which is a signature of a finite modulation of the magnetic structure. In this helically modulated structure, all the spins individually stabilize a helical phase along the *c*-axis of the sample. A schematic of the helical spin structure is shown in Fig. 1.19 (c). The octupole polarization of the samples also rotates along the *c*-axis due to the helical modulation of the iT-AFM structure. This continuous rotation of octupole order leads to a net-zero Hall signal, as the Hall contribution corresponding to each unit cell is canceled out by an opposite counterpart of the helical structure. *The mechanism and possible control of this helical transition is yet to be explored.*

In stark contrast to the M (T) data presented in Fig. 1.18 (a), the observation of $M(T)$ data similar to that is shown in Fig. 1.20 (a)[54] has also been reported. Here, no transition was observed around 200 K; rather, a different type of transition can be seen at very low temperatures. At around 50 K, the magnetization suddenly increases to a high value, and the zero field cooled (ZFC) and field cooled (FC) $M(T)$ curves show a large bifurcation. This phase has not been studied in detail and was termed as a spin-glass phase without any substantiated data.[68] In a recent report, Rout et al. have observed a complex Hall signature in this phase. Figure 1.20 (b)

shows the Hall signal as found at 2 K. The $M(H)$ measurement has shown that a large ferromagnetic-like hysteresis is present in this phase. The Hall signal reveals a topological Hall-like feature, where the Hall resistivity increases to a maximum with increasing fields and then reduces to a small value. The authors have suggested a field-induced non-coplanar state to be the source of this Hall signal, but a detailed understanding is still to be achieved. These unknown aspects of modification of the iT-AFM state of Mn_3Sn make it a very compelling system for further exploration of the intertwined nature of the magnetic ground states and various observable signatures.

1.5 Outline of the Thesis

In the work carried out in this thesis, a detailed study on the modified iT-AFM state of Mn_3Sn is carried out. The unanswered questions relating to the mechanism and control of the helical transition, along with the low-temperature transition are tackled using magnetic, transport, and neutron diffraction studies. The first part of the work, i.e., chapter 3 is concentrated on the understanding of the mechanisms of helical phase transition and its control to facilitate the use of AHE in devices. The second part of the work, i.e., chapter 4 and 5 are devoted on the understanding of the unknown magnetic phase at the low temperature.

Chapter 2

Experimental techniques and methods

This chapter focuses on the specific instruments and methods used to carry out the work in the present thesis. First, a discussion on the experimental techniques used for the present thesis will be presented, followed by a summary of the theoretical tools employed. The experimental research in condensed matter/material science starts with a motivation to understand a physical phenomenon or properties using a specific material. For the work carried out in this thesis, polycrystalline and single crystal samples of different electron doped Mn_3Sn system are synthesized. Let's start with the process of sample preparation.

2.1 Sample preparation

Polycrystalline samples : The polycrystalline samples used for the present thesis are synthesized using an arc melting furnace, where constituent metallic elements of the required sample are melted together at high temperatures. The arc melting furnace used for the present sample synthesis is depicted in Fig. 2.1. It consists of a sharp-tipped tungsten electrode, a copper hearth, vacuum chamber, pumping system, and a current source. The sharp-tipped tungsten electrode is held close to

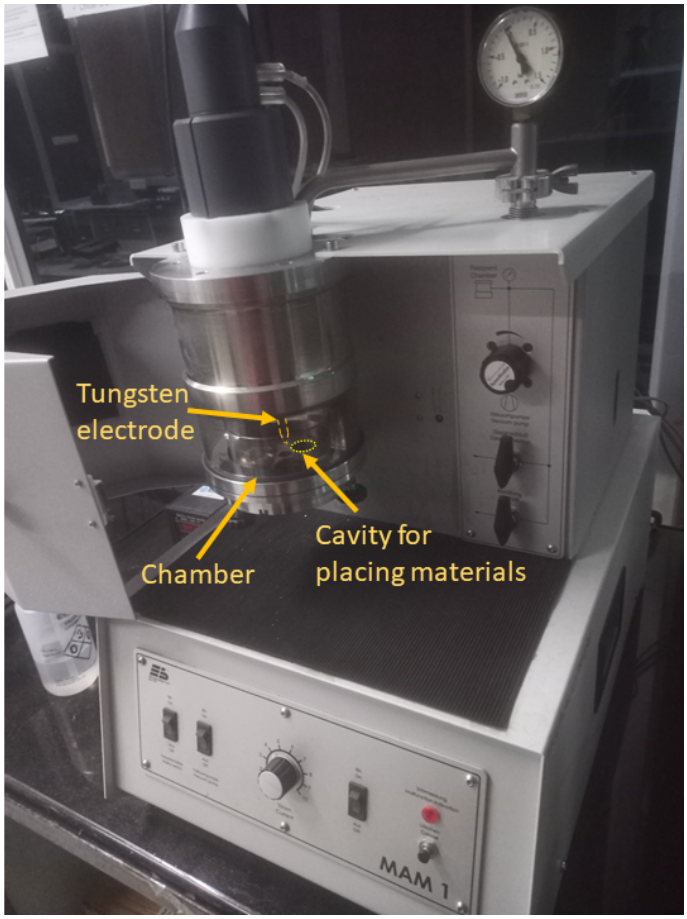

Figure 2.1: Arc-melting furnace used to melt and synthesize polycrystalline sample.

the surface of a copper hearth, where the samples are melted in cylindrical grooves. The chamber is first purged with high purity argon gas and pumped several times. To eliminate any remaining oxygen, a pure titanium ingot is utilized as a getter to absorb oxygen. A high current is applied between the electrodes which ionize the argon gas, and an arc is formed between the tungsten electrode and copper hearth. It is expected that temperatures as high as 3000°C can be generated by the arc. The copper hearth and the power input are cooled using a constant flow of chilled water. After exposure to the arc, the resultant material forms an ingot of the constituent materials. The ingots are generally flipped several times and remelted to achieve a homogeneous composition. The final sample produced by the melting at a very high temperature can exhibit a poor crystalline nature. Hence, the as-melted ingots are annealed at a material-specific temperature to improve crystallinity and promote a

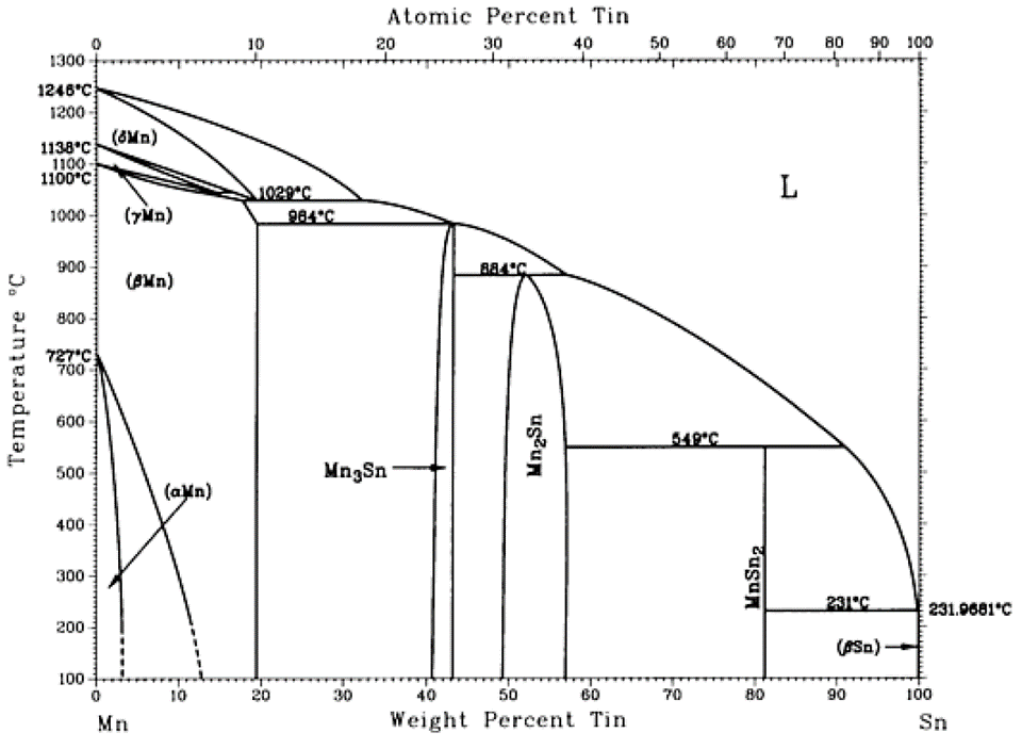

Figure 2.2: Binary phase diagram for Mn-Sn elements.[69]

single phase. The annealing temperature is set to be roughly 70-80% of the melting point of the material. In the present case, different electron doped Mn_3Sn samples are annealed for a week at 800°C.

Single crystals : To obtain single-crystal samples used for the present thesis, the self flux technique is employed. The polycrystalline samples obtained following the previous process are first powdered. The powdered samples are then sealed in pointed alumina crucibles. Following that, the samples are mixed and homogenized at a temperature above the melting point. The phase diagram of Mn-Sn is shown in Fig 2.3 (a). From the phase diagram, we observe that the melting point of Mn: Sn = 3:1 mixture is around 970°C. Thus, the furnace was heated to 1000°C for 24 hours for our purpose. Then, the furnace was kept there for another 24 hours. The temperature was then gradually reduced at a rate of 1°C/hr. Following this procedure, we move from a liquid Mn-Sn phase to the Mn_3Sn phase in the phase diagram. This process slowly forms single crystals of the required Mn_3Sn materials.

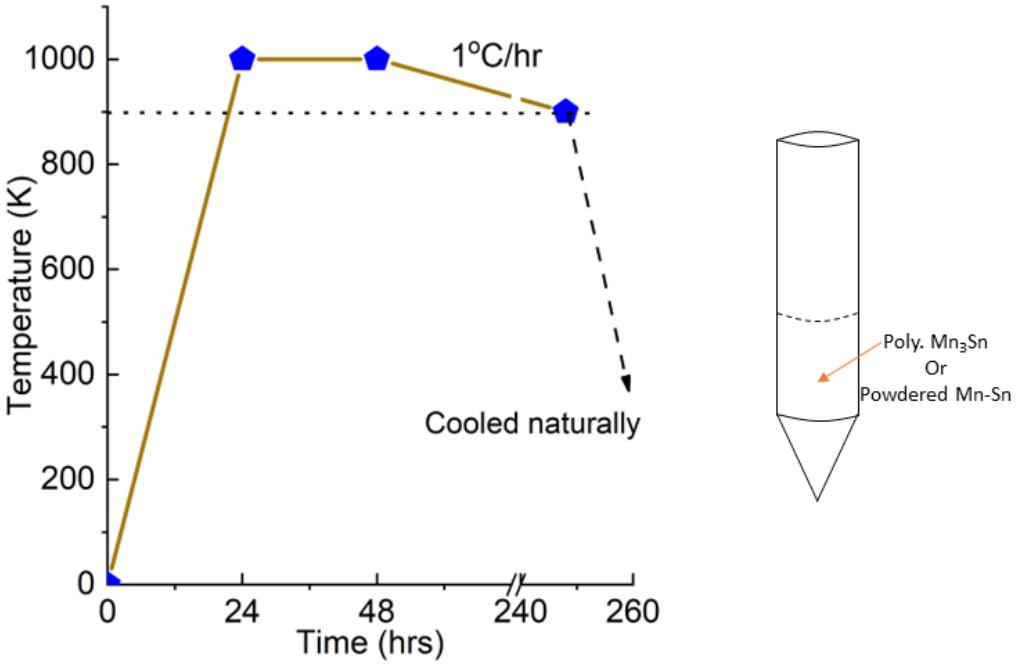

Figure 2.3: Temperature profile used for the synthesis of single crystalline samples. The pointed alumina crucible was used to keep the powdered samples in furnace.

It was discovered that a mixture of Mn: Sn in the ratio 3.09: 0.91 resulted in the formation of larger single crystals, whereas a ratio with less Mn resulted in the formation of tiny crystals. The final temperature of 900°C was chosen to stay above the crystallization temperature of Mn_2Sn. For the Fe doped samples, this temperature was chosen to be a bit below 900°C. The furnace was turned off and left to cool naturally after another 24 hours at 900°C. Figure 2.3 shows the temperature profile employed for the single crystal preparation. For the $Mn_{3.09}Sn_{0.91}$ composition, this procedure produced large crystals of length about 5 mm. It is found that the size of the Fe doped single crystals decreases with increasing Fe concentration. It is also important to mention that, the above discussed procedure can be utilized to generate single crystals directly from a mixture of constituent elements without following the arc melting procedure.

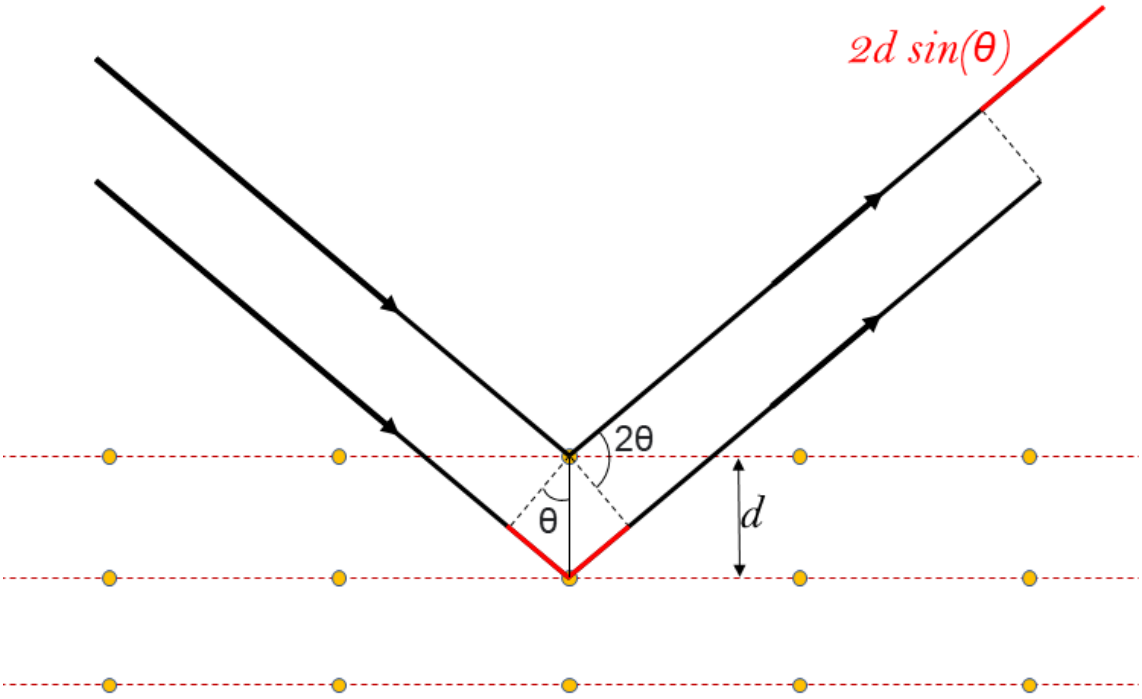

Figure 2.4: Schematic representation of x-ray diffracting from planes of atoms.

2.2 Structural characterization

The structural properties of the samples were determined using x-ray diffraction (XRD) technique.

2.2.1 X-ray Diffraction

The samples described in section 1.4 are crystalline in nature. To confirm the phase purity and crystalline nature, XRD measurements are carried out on the samples. The spacing between atoms in a crystalline material is usually of the order of few . Hence, x-rays are an excellent source for studying the crystal structure. The XRD measurement works on the basis of Bragg's law. Consider a plane of atoms, as shown in Fig. 2.4. Here we consider a simple rectangular lattice, with the distance between planes to be d. When a parallel beam of x-rays falls on this plane, the incident rays get diffracted by different layers of the atomic planes. The reflected

beams from different planes acquire a finite path difference. For an incident angle of θ, the path difference between two rays is $2d\sin(\theta)$. The reflected rays can undergo constructive or destructive interference depending on the path difference created and the wavelength of incident light. Mathematically, constructive interference occurs when

$$2dsin(\theta) = n\lambda. \tag{2.1}$$

The above equation is called Bragg's condition. Thus, knowing the incident angle and the wavelength of x-rays, the value of d can be deduced by scanning the theta. The exact process can be repeated for different planes, and a detailed crystal structure can be resolved. For the work presented in this thesis, the room temperature XRD measurements were performed using a Rigaku SmartLab x-ray diffractometer. The x-ray was operated at 40 kV and 30 nA current. A Cu-Kα source with an x-ray wavelength of 1.54182 was used. The diffraction data were recorded using the 2θ range 10° to 90°. The temperature dependent x-ray data were measured by employing a PANalytical diffractometer, with temperature range of T = 15 K to 650 K.

2.2.2 Extreme condition XRD

Extreme pressure XRD measurements were performed at the Raja Ramanna Centre for Advanced Technology's INDUS-II synchrotron radiation source in Indore, India. The BL-11 Beamline is a specialized instrument for XRD measurements in a variety of extreme conditions. The option to measure the XRD pattern at extreme pressure was used for the present study. A diamond anvil cell (DAC) was utilized for the high pressures. The powder samples were placed between the end of two small diamond pieces. The powder is kept inside a small hole in the metal gasket that separates the diamond heads. The diamond anvil cell holder was then subjected to external pressure. The DAV holder is depicted schematically in Fig. 2.5. Small ruby pieces were placed in the sample area in addition to the powder sample for determining the

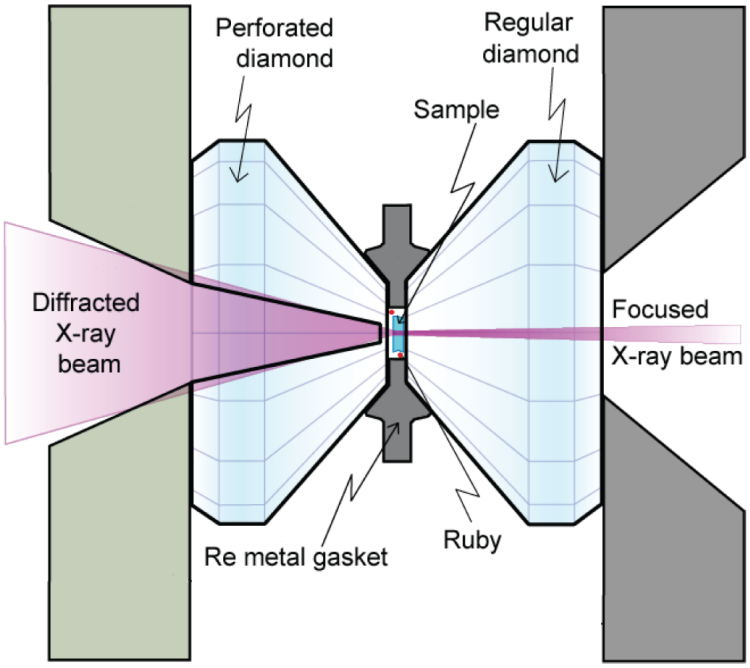

Figure 2.5: (a) A schematic representation of a diamond anvil cell.[70]

amount of pressure applied to the sample area. Ruby shows a well-defined shift in the photoluminescence spectra with applied pressure.[71] The PL spectra are measured with a laser before and after pressure is applied. The wavelength used for the experiments in the synchrotron was 0.500022 . The diffracted rays were detected using a high purity Germanium detector.

2.3 Magnetic characterization

Following the determination of crystal structure of the materials studied in this thesis, the characterization of the magnetic properties was performed with varying the temperatures and applied magnetic fields. For this purpose, a vibrating sample magnetometer (VSM) attached to a superconducting quantum interference device (SQUID) magnetometer was utilized (MPMS-3, Quantum Design).

2.3.1 Vibrating sample magnetometer

In a typical magnetometer, measuring the magnetic moment of a sample involves two steps. The sample's magnetic signal is first transformed into an electric signal by using the Faraday's law of electromagnetic induction, which can be written as,

$$V_{coil} = \frac{d\phi}{dt}. \tag{2.2}$$

Here, V_{coil} is the induced voltage, ϕ is the magnetic flux enclosed in the loop, and t is the time. Due to the induced voltage, a current is generated. In the vibrating sample magnetometer, the sample is made to oscillate along the axis of a circular loop. The oscillations are required to generate a finite time-dependent change in magnetic flux across the loop. The center of the oscillation is fixed at the center of the conducting loop. This oscillatory motion is carried out using a linear motor, to which the sample is connected through a sample rod. When the sample starts to oscillate around the center of the loop, the Equation 2.2 can be rewritten as

$$V_{coil} = \frac{d\phi}{dz}.\frac{dz}{dt} \tag{2.3}$$

where z is the direction of oscillation. This can further be reduced to the following equation for a sinusoidal oscillation.

$$V_{coil} = 2CmA\sqrt{f}sin(2\sqrt{f}t) \tag{2.4}$$

As a result, the current created in the loop provides direct information about the sample's magnetic moment. A four coil setup is used to pick up the VSM signal in a real system. The four coils are arranged as shown in Fig. 2.6. Such a configuration reduced the effect of any constant magnetic field and generated a pure signal from the sample. Next, the generated current signal is measured to calculate the magnetic moment of the sample. The precision of magnetic measurements depends on the instrument's capacity to measure this current. A Superconducting Quantum

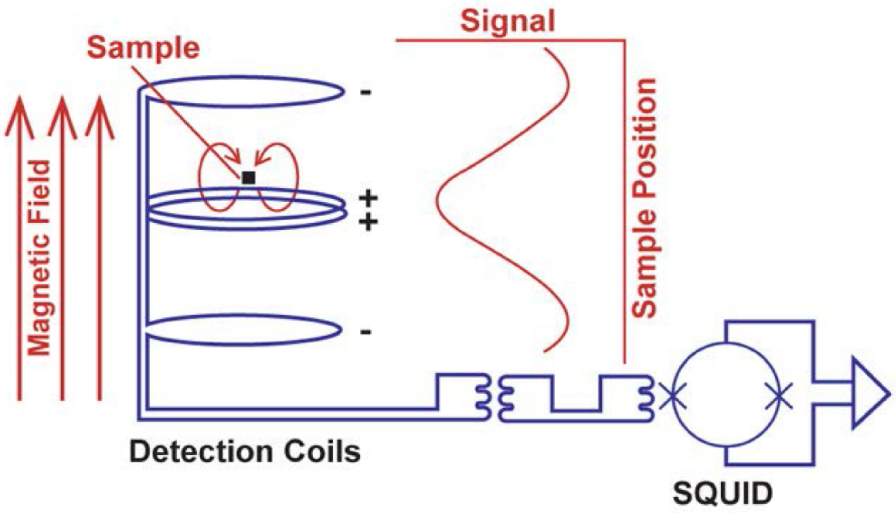

Figure 2.6: The schematic diagram of a VSM coils attached with SQUID sensor. Picture taken from Quantum Design MPMS-3 user's manual.

Interference Device is utilized to measure this current efficiently.

2.3.2 Superconducting Quantum Interference Device

The SQUID is based on the concept of two Josephson junctions joined in a superconducting loop. The Josephson junction is a setup of two superconductors separated by thin insulation of a metallic barrier (right side of Fig. 2.6). The thickness of the barrier is small such that the Cooper pairs can tunnel through the junction. If an insulator is used, the thickness is usually of the order of tens of , whereas for a metallic barrier, the thickness can be microns thick. The critical current around this superconducting loop depends on the mutual phase difference of the two currents flowing through the two Josephson junctions. When the dc SQUID is current biased, the voltage measured about the two ends of the SQUID oscillates between a high and low value with an oscillating period equal to ϕ_0 ($=\frac{h}{2e}$). This voltage generated by the change of a single quantum of magnetic flux can then be measured by conventional electronic systems. The current signal created by the sample movement is then inductively connected to the SQUID magnetometer. Thus, the current

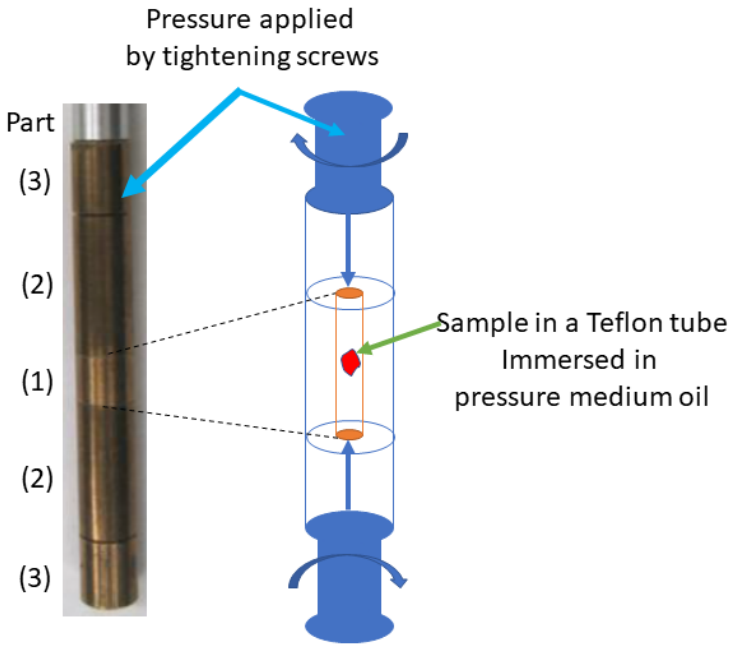

Figure 2.7: Real and schematic picture of the Quantum Design made magnetic pressure cell.

signal detected by the coil in VSM mode is detected by the highly efficient SQUID. The SQUID device is installed at a distance from the VSM area and is covered in a superconducting shield to minimize any external noise in the SQUID system.

2.3.3 High pressure magnetic measurements

The high-pressure magnetic measurements were carried out using a Quantum Design (QD)-made high-pressure cell. The body of the pressure cell is made up of beryllium copper (Be-Cu) alloy for its high strength and non-magnetic nature of the material. The schematic and picture of the pressure cell used in the SQUID magnetometer are shown in Fig. 2.7. The central part (1) is a half hollow Be-Cu cylinder. A Teflon cylindrical vessel with pressure transmitting liquid and sample is inserted into the central Be-Cu part. The Teflon cylinder is closed from both sides with Teflon caps. Afterward, two long Be-Cu cylindrical-shaped hollow cylinders [part (2)] are tightened at both sides of the central part (1). Two pistons are inserted into these cylinders. Lastly, at the ends of part (2) cylinders, pressure is applied to the

central Teflon tube by tightening the screws [part (3)] from both ends of the sample holder. A superconducting material like In or Sb is added along with a sample in the Teflon tube. The superconducting transition temperature is measured to calculate the applied pressure upon tightening screws. The maximum pressure that can be applied using QD magnetic pressure cell is 1.5 GPa.

2.3.4 Neutron diffraction

Just as an x-ray is used for determining the crystal structure of a sample, the neutron can also be used for the determination of crystal as well as the magnetic structure of the samples. The De-Broglie wavelength of the neutrons is comparable to that of the lattice spacing. The thermal neutrons typically posses a wavelength of about 1-4 . The use of neutron source gives some advantages like 2θ independent scattering and higher resolution for the detection of isotopes and lighter elements. Apart from these properties, the main advantage of using neutrons lies in the fact that the neutrons exhibit a finite magnetic moment, which enables the interaction of neutrons with the magnetic moment of the electrons in the materials. Thus, neutron diffraction can be used to extract information regarding the magnetic structure in addition to the crystal structure.

The neutron diffraction generates a diffraction pattern depending on the magnetic ground state of the sample. Let us understand better with the help of Fig. 2.8. When neutron diffraction is used on a non-magnetic lattice, it generates Bragg's peaks similar to the x-ra, as shown in case-1. When we consider a ferromagnetic sample, as considered in the 2, the magnetic reflections appear on top of the nuclear reflections. When an antiferromagnetic is used, as shown in 4, magnetic reflections appear at half the value of the earlier nuclear reflections. This is because the magnetic unit cell has a periodicity of $2a$ for the antiferromagnetic state. In the case of ferrimagnets, as shown in 3, we observe half indexed as well as integer indexed magnetic reflections. For a non-collinear state, as shown in 5 and 6, the magnetic unit cell shows a length of $4a$. Thus quarter indexed magnetic peaks are observed.

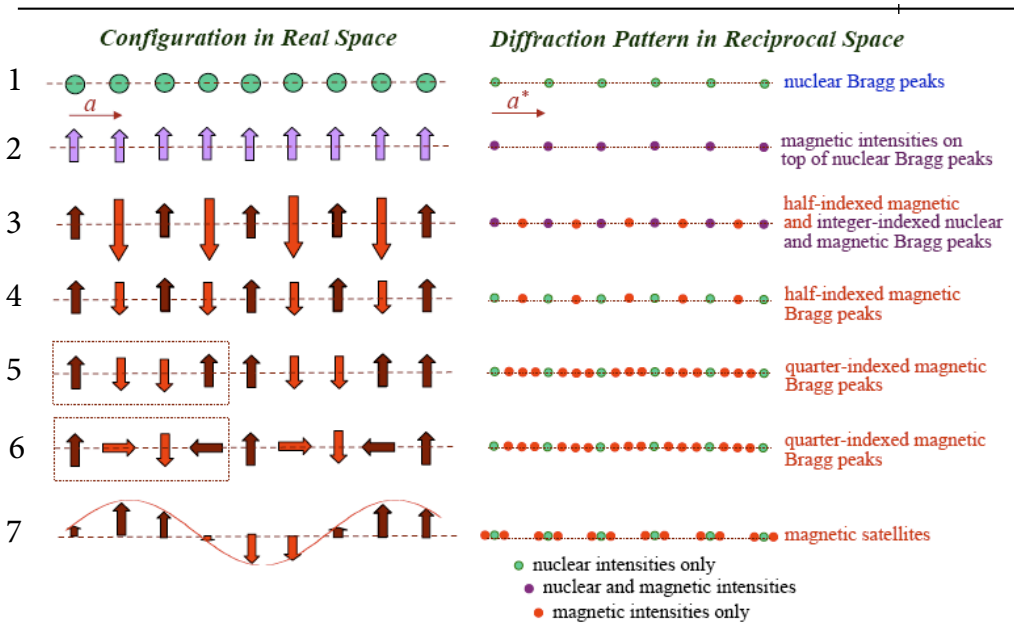

Figure 2.8: Different magnetic states and their respective magnetic reflections along with the nuclear reflections.. Picture taken from reference [72].

Apart from the reflection appearing due to modification of the length of the magnetic unit cell, another magnetic state with incommensurate modulations can also be detected using neutron diffraction. One such state is depicted in 7, where the magnetic moments change slowly. In this case, the magnetic unit cell do not show an integer multiple of the lattice unit cell. Hence, satellite-like magnetic reflections are observed on both sides of the nuclear peaks.

For the work in this thesis, the neutron diffraction data were taken on a PD2 neutron diffractometer with $\lambda = 1.2443$ at Dhruva reactor, Bhabha Atomic Research Centre, Mumbai, and at high resolution neutron powder diffractometer ECHIDNA of Australian Nuclear Science and Technology (ANSTO) with a monochromatic neutron wavelength of $\lambda = 2.44$.

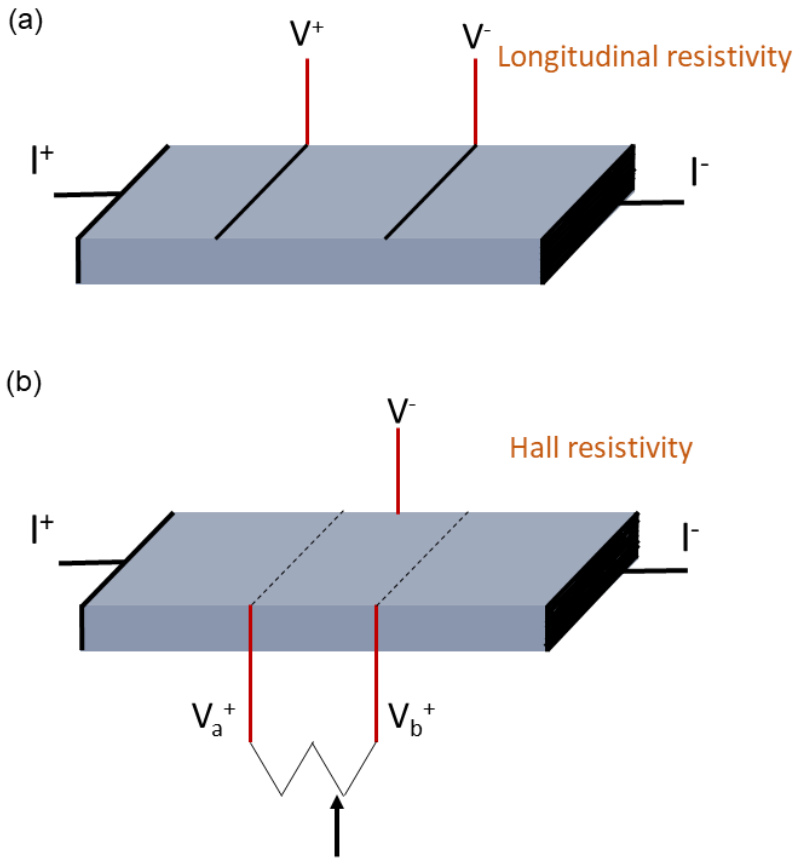

Figure 2.9: A schematic of the connection made so as to measure (a) longitudnal resistivity using four probe method and (b) Hall resistivity using five probe method.

2.4 Electronic transport measurements

Hall bars fabrication

The electronic transport properties f the samples were recorded on rectangular shapes Hall bar samples, with typical lengths of 5mmx1mmx0.5 mm for the polycrystalline samples and similar shapes but with a smaller size for the single crystalline samples. The Hall bars were shaped using a diamond and wire cutter for precise cutting. These Hall bars were then used for transport properties.

Electronic transport measurement details

A Quantum Design Physical Property measurement System (PPMS) was used to evaluate the electronic transport properties. The longitudinal and transverse resistivity of the samples were measured using the AC transport (ACT) option of the PPMS. A constant current was applied along the length of a rectangular-shaped sample to determine its resistivity. The current contacts are made across the entire cross-section of the sample to flow a homogeneous current through out the sample. The voltage drop was measured using two voltage probes in the four-probe configuration. The connection diagram is shown in Fig. 2.9 (a) The measure voltage signal was then converted into resistivity by using the relation.

$$\rho_{xx} = \frac{A}{l}\frac{V}{I}. \tag{2.5}$$

Here A is the cross-section area of the sample, l is the distance between the voltage leads, V is the voltage drop measured, and I is the applied current. The same four-probe technique can be utilized for Hall measurement, as shown in Fig. 2.10(b). In four-probe configuration the voltage connections must be made opposite to each other at the two sides of the sample to detect a pure Hall signal. In practice, achieving such a precise alignment of voltage probes is difficult, and we invariably end up with a magnetoresistance signal in addition to the desired Hall signal. A five-probe approach with an additional voltage probe is employed to solve this problem. At zero magnetic field, the excess voltage signal is initially neutralized. The nullification is achieved by using a potentiometer between the two contacts to achieve a zero voltage before measurements. This significantly reduces the contribution of magnetoresistance to the measured Hall signal.

Figure 2.10: Picture of the ACT high pressure

In addition, the QD-PPMS allows detecting resistivity in both DC and AC modes. The ACT option of the PPMS was used to conduct all of the resistivity measurements reported in this thesis as it offers the benefit of a signal filtering process. The AC bias can be set with a frequency anywhere between 1 Hz and 1 kHz, which improves measurement precision. The time-dependent profile and frequency of the target signal to be detected are identical to those of the applied AC current. Frequency-dependent noise, DC offset, and instrumental drift can be reduced in the ACT measurement mode.

The high-pressure transport properties were also measured using the ACT option in the PPMS. A QD-made Be-Cu high-pressure cell was used to measure the pressure-dependent transport properties (Fig. 2.10). The working principle of the ACT pressure cell is similar to the magnetic pressure cell. The sample and a superconducting wire were installed in the Teflon cylinder with pressure transmitting oil inside for the ACT case. The sample was fixed on a small custom-made Teflon base, and the required Hall or longitudinal resistivity connections were made. The pressure is measured by measuring the superconducting transition of the superconductor after applying pressure to the cell.

The above-mentioned magnetic and transport measurements are measured under magnetic fields up to 5 Tesla. The magnetic field is generated using superconducting magnet that is immersed in a cold He-liquid chamber of the measurement unit. The He is liquefied using a cold head, through which highly pressurized He flows. The cold head employs the Joule-Thomson Cooling effect to reduce the temperature further. A controlled flow of He from Dewar to the chamber is used to cool down the sample chamber temperature in the range from 2 K to 400 K.

2.5 Analysis and theoretical methods

Once the required data was collected, the next step is the modeling and analysis of the data. The work related to data fitting, and analytical modeling of Hamiltonian

was performed using self-written python codes. In addition to an analysis of the model Hamiltonian, the ab-initio calculations is used extensively in this thesis to understand the experimental data and elucidate the hidden physics.

2.5.1 Density functional theory (DFT)

The problem of theoretically evaluating the properties of a system can be achieved by solving the Hamiltonian of a system. The equation to solve for the periodic lattices of condensed matter systems is a many-body Hamiltonian involving the nucleus and electrons. The nuclear and electron motion can be decoupled using the Born Oppenheimer approximation, leaving us with solving a many-body electron system. Subsequently, the Hartree-Fock (HF) formalism was introduced to obtain many body wave functions, where the many body wave function is assumed to be a product of the wave functions of individual electrons. Later, the proposal to use density in place of the $3N$ electron coordination was put forward. Finally, with the efforts of Kohn, Hohenberg, and Sham, the current form of DFT was put forward. The DFT theory reduces the system to a non-interacting particle system. An external potential is used on a particle in such a way that particle density and total energy of the system match to that of an interacting many-body system. The density functional used in DFT can be written as,

$$F(n) = T_S(n) + E_H(n) + E_{ex}(n). \tag{2.6}$$

Here, the first term is the kinetic energy of the system, the second term is the Hartree function, and the third term represents the exchange-correlation. The HF model incorporates the Coulomb interaction and direct exchange interaction terms. All other interactions like exchange due to Pauli's exclusion principle and correlation effects are included in the E_{ex} term.

These pieces of information are incorporated into a DFT calculation by means of a pseudo-potential. These are the effective potential that acts on the valance elec-

trons of a system. These are calculated from all-electron calculations considering a rigid ion core with nuclei and strongly bound core electrons. In the pseudo-potential approach, the ion core is assumed to not participate in the chemical bonding. The Kohn-Sham equation of DFT is solved in a self-consistent way, where the Kohn-Sham potentials are calculated from an initial guess (input density state) of the density. The Kohn-Sham Hamiltonian is then solved on the system with an input density state. A new (output) density state is calculated from this solution, which is then compared with the old density state. A match under a cutoff difference ends the calculation, and else the process is repeated with the output density state as the new input.

The exact form of the E_{ex} is not known, and various approximations have been used for practical calculations. The most basic and frequently used exchange-correlation functionals are those with local density approximation (LDA) and generalized gradient approximation (GGA).

Local Density Approximation (LDA)

In this form of approximation, the system is divided into small volumes, and the density inside these volumes is taken to be constant. The exchange-correlation energy for each volume is evaluated by calculating the energy of uniform electron gas at the same density. The exchange correlation energy for LDA can be written as,

$$E_{ex}^{LDA} = \int \rho(\mathbf{r}) \epsilon_{ex}^{unif}[\rho(\mathbf{r})] d\mathbf{r}, \tag{2.7}$$

where $\epsilon_{ex}^{unif}[\rho(\mathbf{r})]$ is the exchange-correlation energy density for the interacting electron gas of density $\rho(\mathbf{r})$. Thus, the potential in the case of LDA only depends on the density of the system. These potentials have been found to work very well for metallic systems.

Generalized Gradient Approximation (GGA)

The LDA can then be improved by including the variation in density in the exchange-correlation functional. The GGA exchange-correlation functionals can be written in the form

$$E_{ex}^{GGA} = \int f_{ex}^{GGA}[\rho(\mathbf{r}), \nabla\rho(\mathbf{r})]d\mathbf{r}. \tag{2.8}$$

The GGA potentials improve over LDA results in some cases. As mentioned earlier, the LDA potentials work well for the metallic materials and is used for the calculations used to carry out the work of this thesis.

2.5.2 Calculation details

The first principle calculations have been performed by using the Vienna *ab initio* simulation package (VASP). VASP is a plane wave pseudopotential-based code used extensively to perform DFT calculations. The spin-polarized calculations were performed within the projector augmented wave (PAW) method[73] as implemented in VASP.[74,75,76,77] The generalized gradient approximation (GGA) exchange-correlation potential in the form of Perdew-Burke-Enzerhof (PBE)[78] was used. A Γ-centered k-point grid of 8×8×9 is used for the Brillouin-Zone (BZ) integration. The plane-wave cut-off energy is set as 500 eV. The noncollinear version of the VASP code is used to perform the magnetic calculations for the current hexagonal system. The lattice constants are fixed as the experimentally obtained values for the lattice relaxation, while the internal coordinates are relaxed till the forces become less than 1 meV/Å. Further, the spin-spiral calculations are performed using the full-potential linearized augmented plane wave (FLAPW) method implementing the noncollinear version of the FLEUR code.[79] The energy of the SS state characterized is calculated using the generalized Bloch theorem.[80] A mesh of 16×16×18 is used for k-points in the full-BZ and a cutoff of $K_{max} = 4.1\ a.u.^{-1}$ to expand the LAPW basis functions.

Chapter 3

Pressure induced switching of noncollinear magnetic state in Mn_3Sn

A review of the literature and different methods for carrying out the work in the present thesis have been provided in the previous two chapters. The present chapter will focus on some of the important works that have been carried out in this thesis. The main objective of this thesis is to examine and comprehend the temperature evolution of the magnetic ground state of the extremely important noncollinear antiferromagnetic compound Mn_3Sn. In this chapter, the findings of a detailed study on the helical phase transition of the iT-AFM spin structure are presented. As it is discussed in chapter 1, the helical transition in some of the Mn_3Sn samples appears around 200-250 K, while it is absent in few Mn_3Sn samples. As the helical phase transition does not always show up in the temperature dependence of the magnetic ground state of Mn_3Sn, it becomes imperative to synthesize samples with reproducible magnetic properties. Thus to conduct the intended study, the first step is to prepare samples that host the helical phase of the iT-AFM state.

It is found from the literature survey that a stoichiometric ratio of 3:1 for the Mn_3Sn compound is not stable. The hexagonal phase of Mn_3Sn is stable with some

level of electron doping in $Mn_{3+x}Sn_{1-x}$. The large AHE has been initially reported in $Mn_{3.02}Sn_{0.98}$, i.e., $x = 0.02$. On the other hand, the large THE was discovered for of $x = 0.05$, i.e. $Mn_{3.05}Sn_{0.95}$. The value of x reach as high as 0.09 and 0.16 for single crystalline samples and epitaxial thin films, respectively.[45,60]

Motivated by these studies, polycrystalline samples of $Mn_{3+x}Sn_{1-x}$ are synthesized with $x = 0.03$, 0.04, and 0.05 to explore a link between the electron doping and dissimilar temperature dependency of the magnetic ground state. The samples are synthesized using arc melting technique as described in chapter 2. The XRD measurements at room temperature are used to confirm the crystal structure of the samples. Magnetic and transport measurements are carried out to explore the physical properties of the samples. A theoretical understanding of the helical phase transition is realized using the information from the experimental characterization of the samples. Utilizing this newly acquired knowledge, the external control of the helical phase transition that leads to the switching of the anomalous Hall signal is also demonstrated.

3.1 Sample characterization

3.1.1 Determination of sample structure

Powder XRD measurements are performed to confirm the hexagonal crystal structure of the $Mn_{3+x}Sn_{1-x}$ samples. The XRD data are recorded for 2θ values between 10° to 90°, at a step of 0.01°. The XRD patterns for the three samples are shown in Fig. 3.1 (a-c). The scattered data shown in blue color correspond to the experimental data. The structural information is extracted from the XRD data using the Rietveld refinement. The initial structural information of the Mn_3Sn was ob-

Table 3.1: The structural information of the Mn_3Sn unit cell.

Space group = 196	
	Wyckoff Position
Mn	$6h$ (x,$2x$,1/4)
	$x = 0.1616$
Sn	$2d$ (1/3,2/3,3/4)

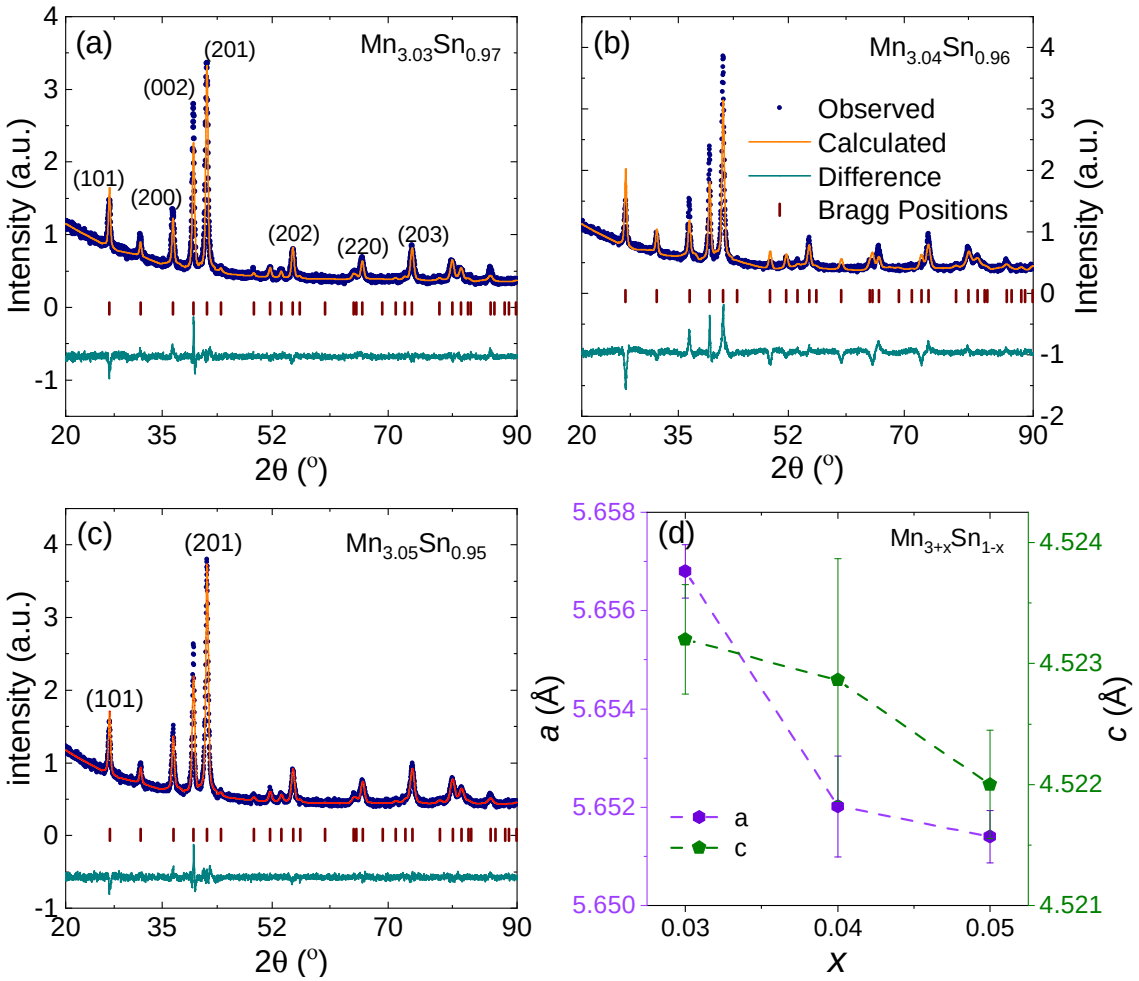

Figure 3.1: XRD patterns with Rietveld refinement for (a) $Mn_{3.03}Sn_{0.97}$, (b) $Mn_{3.04}Sn_{0.96}$, and (c) $Mn_{3.05}Sn_{0.95}$. Some high intensity peaks are labeled in the figure (a). The legend for first three plots is shown in figure (b). (d) Calculated a and c values from the Rietveld refinement.

tained from the literature as tabulated in table 3.1. The fitted curves, the Bragg peak positions, and the difference between calculated and recorded data are also plotted in the Fig. 3.1 (a-c) for the three samples. It can be seen that the XRD patterns can be fitted nicely taking the hexagonal crystal structure of the samples. All the peaks can be indexed to the various reflections of the hexagonal Mn_3Sn structure. The mismatch in the intensities of calculated and measured XRD data mostly originates from the preferred orientation of the grains in the sample. Nevertheless, the perfect indexing of all the peaks confirms the presence of a single hexagonal

phase of Mn_3Sn for all the samples. The lattice parameters for the samples are plotted in Fig. 3.1 (d). A small reduction in lattice parameters is observed with increasing Mn concentration, but the observed change is less than 0.1%.

3.1.2 Magnetic properties

After successful synthesis and structural characterization, the magnetic properties of theses samples are studied. The temperature dependent magnetization [$M(T)$] measurements are performed in the zero field cooled (ZFC) and field cooled (FC) modes in the presence of a field of 1000 Oe. The $M(T)$ graphs are shown in Fig. 3.2. It is quite interesting that although all the samples exhibits same crystal structure with a small variation of lattice parameters, although the $M(T)$ curves are not identical. For the $Mn_{3.03}Sn_{0.97}$ sample [Fig. 3.2 (a)], the magnetization starts at a finite value at room temperature. Upon lowering the temperature, a sharp fall in the magnetization is observed around 200 K, before starts to climb upwards below 50 K. The first derivative of the FC curve is also plotted along with FC and ZFC magnetization curves. The first derivative show two distinct extrema, one around 200 K and another below 50 K. The transition around 200 K corresponds to the helical phase transition of the iT-AFM magnetic phase (chapter 1). Moving on to the $Mn_{3.04}Sn_{0.96}$ sample [Fig. 3.2 (b)], a similar trend with different relative magnitude of the two magnetic transitions is found. The high-temperature transition is now dominated by a contribution from the low temperature transition. The derivative of the FC curve shows a clear signature of both the transitions. A significant bifurcation between the ZFC and FC curves also appears at low temperatures. Lastly, for the sample $Mn_{3.05}Sn_{0.95}$ [Fig. 3.2 (c)], the high temperature transition is absent, while a large transition at the low temperatures appears. The temperature corresponding to both the transitions as extracted from the derivative of the FC curve is plotted in Fig. 3.2 (d). The helical phase transition temperature decreases with electron doping and is absent for $Mn_{3.05}Sn_{0.95}$ sample, while the critical temperature of low temperature transition keeps on increasing. In the present chapter, the manipulation

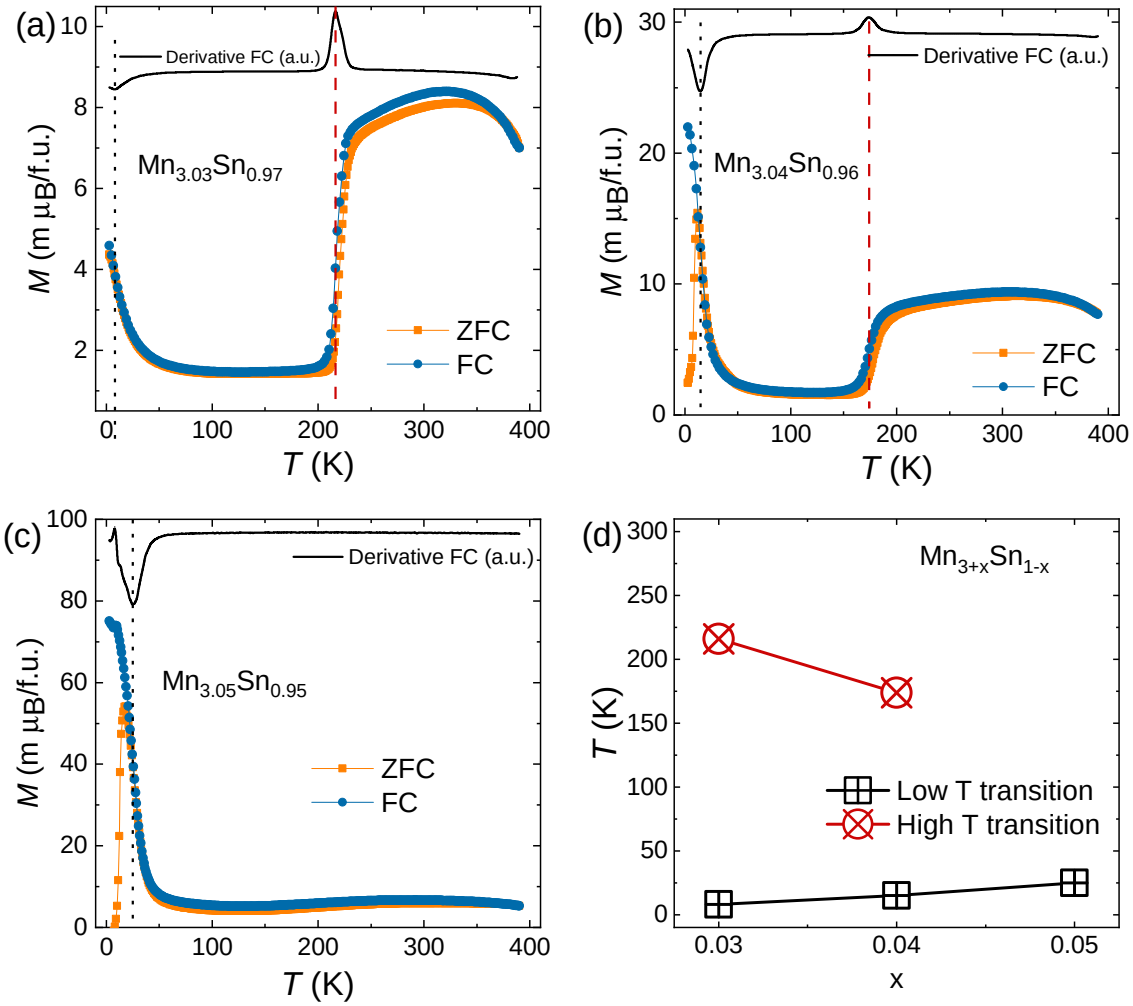

Figure 3.2: Temperature dependence of zero field cooled (ZFC) and field cooled (FC) magnetization $[M(T)]$ for (a) $Mn_{3.03}Sn_{0.97}$, (b) $Mn_{3.04}Sn_{0.96}$ and (c) $Mn_{3.05}Sn_{0.95}$ samples. The first derivative of FC curve is also plotted as black line. (d) Temperature corresponding to low temperature and high temperature transition for three samples. The transition temperatures are calculated from derivative of FC curve.

of the helical phase transition is mainly taken into consideration. Therefore, from here on, the discussions will be only limited to physical properties for temperatures greater than 50 K.

Next, the field dependent magnetization $[M(H)]$ measurements are performed to probe the magnetic state at different temperatures. Figure 3.3 (a-b) shows the $M(H)$ plots for $Mn_{3.03}Sn_{0.97}$ and $Mn_{3.05}Sn_{0.95}$ samples. Both samples show near linear $M(H)$ behavior for measurements performed at different temperatures above

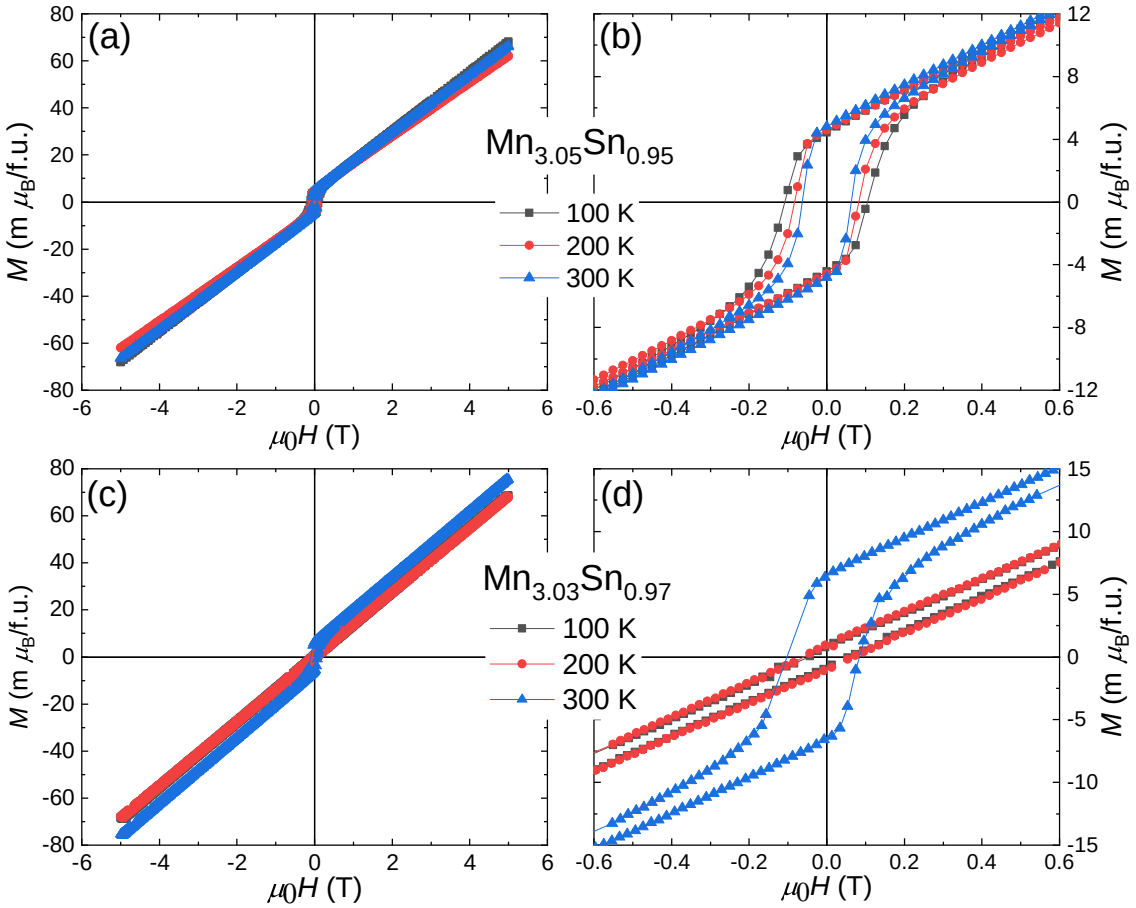

Figure 3.3: Field dependent isothermal magnetization $[M(H)]$ loops for (a) $Mn_{3.05}Sn_{0.95}$ and (c) $Mn_{3.03}Sn_{0.97}$ sample measured at different temperatures. Magnified view of the low field regions of the $M(H)$ loops for both the samples are shown in (b) and (d).

50 K. The linear behavior results from the antiferromagnetic nature of the samples. A magnified view of the $M(H)$ curves is shown in Fig. 3.3 (c) and (d). From the low field plots, it is seen that the $M(H)$ curves show a small ferromagnetic-like hysteresis at 300 K for both the samples. However, a linear behavior is observed below the transition at 200 K for $Mn_{3.03}Sn_{0.97}$ sample. The presence of linear behavior further suggests the presence of the helical phase. As the magnetic moments rotate by full 360° for the helical phase, the net magnetic moment reaches zero. On the other hand, the $Mn_{3.05}Sn_{0.95}$ sample shows hysteresis behaviors in the whole temperature range. As a result, a clear relationship is established between the temperature-dependent magnetic ground state and the electron doping. These findings reveal a

straightforward method for producing Mn_3Sn samples, both with and without the helical phase.

3.1.3 Confirmation of magnetic ground state : neutron diffraction (ND)

Although the samples have been characterized by the help of macroscopic magnetic measurements, these measurements only act as an indication of the magnetic transition. To validate the magnetic ground state, neutron diffraction measurements are performed on $Mn_{3.03}Sn_{0.97}$ and $Mn_{3.05}Sn_{0.95}$ samples. Figure 3.4 shows the room temperature and 150 K neutron diffraction data for $Mn_{3.03}Sn_{0.97}$. The ND data at 300 K and the Rietveld fitting for the iT-AFM structure are shown in Fig. 3.4 (a). It is visible that the room temperature ND data can be easily fitted with the iT-AFM magnetic structure. For the 150 K data, extra peaks are visible in the pattern. Specifically, two very clear peaks can be seen around the (101) peak around (20°). The fitting of the 150 K data with iT-AFM structure is shown in 3.4 (b). It is observed that the above mentioned extra peaks could not be accounted for by the iT-AFM structure. These new peaks and the full pattern can only be taken into account by including a finite modulation vector for the iT-AFM magnetic structure. The fitting after incorporating the helical phase is shown in Fig. 3.4 (c). The helical modulated structure nicely fits the ND data at 150 K. Thus, it is clear that the $Mn_{3.03}Sn_{0.97}$ samples exhibits a helical magnetic phase at 150 K. To correlate the helical phase with temperature, the zoomed-in range of ND data for various temperatures is plotted in Fig. 3.5 (a). It is visible that the satellite peaks start to arise around the same temperature as that of transition in $M(T)$ plots. The extracted q vector of the helical phase is also plotted in Fig. 3.5 (b), where the finite q value is observed below the magnetic transition. Thus the neutron diffraction measurements, in addition to the magnetic characterization, confirm the presence of helical magnetic ground state in the samples.

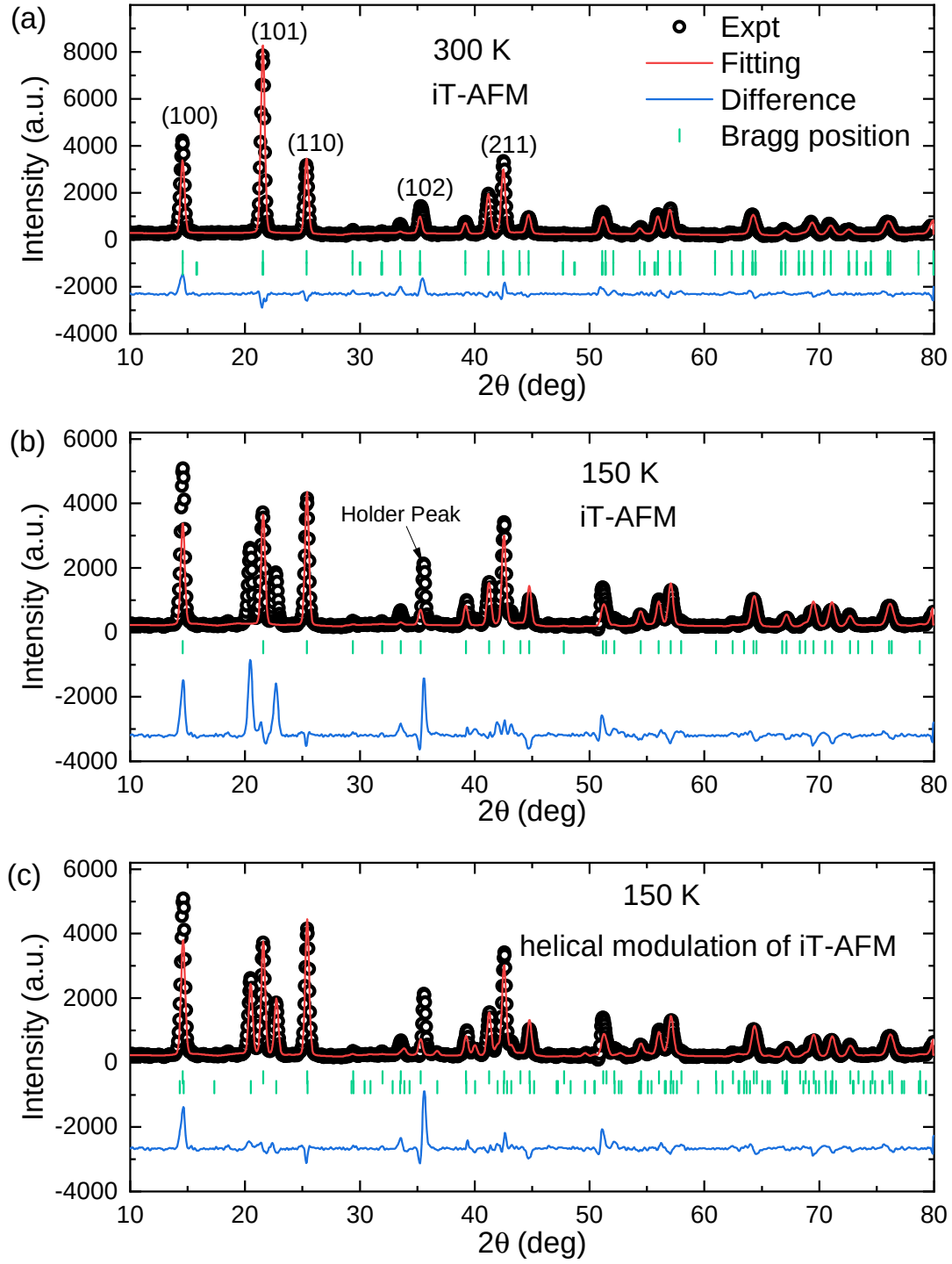

Figure 3.4: Neutron diffraction data with Rietveld refinement at different temperatures for $Mn_{3.03}Sn_{0.97}$ sample. (a) and (b) shows the 300 K and 150 K data and the fitting with iT-AFM structure. (c) shows the fitting of 150 K data with modulated iT-AFM structure.

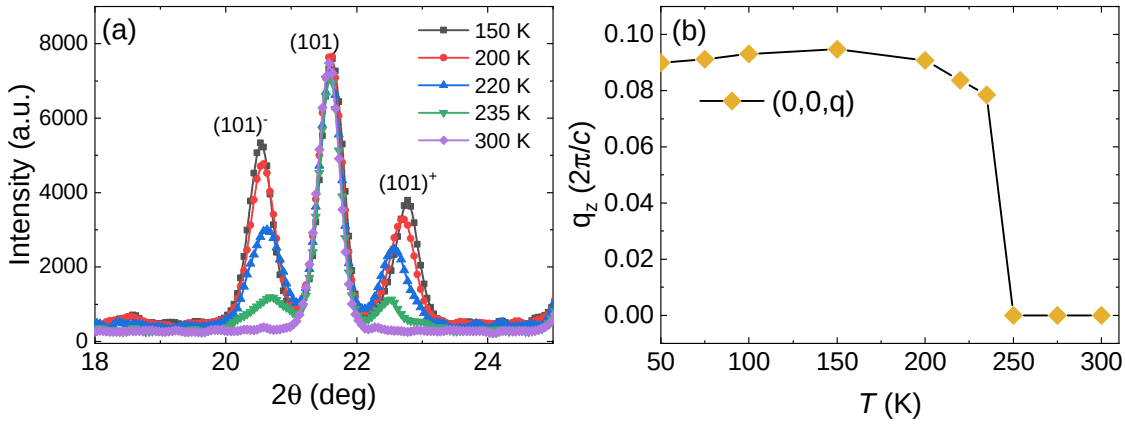

Figure 3.5: (a) ND data around the (101) reflection for the $Mn_{3.03}Sn_{0.97}$ sample at different temperatures. (b) Value of the helical phase modulation vector as extracted from Rietveld refinement of neutron diffraction data.

3.1.4 Electronic transport properties

The transport properties are investigated in order to learn more about the helical phase transition. The strongest feature of the iT-AFM spin structure of Mn_3Sn is the presence of non-trivial Hall signal. The Hall transport (ρ_{xy}), as well as the longitudinal resistivity (ρ_{xx}) of the samples, are measured using a the Physical Property Measurement System (PPMS). Figure 3.6 shows the longitudinal resistivity data recorded in cooling and heating modes for the $Mn_{3.03}Sn_{0.97}$ and $Mn_{3.05}Sn_{0.95}$ samples. Both samples show metallic behavior, as can be seen from the reduction in resistivity with a decrease in temperature. The data for $Mn_{3.05}Sn_{0.95}$ sample only shows the standard metallic curve, and no other features are visible. The peak at 50 K is due to the Inconel effect,[81] which arises due to the measurement setup. For the $Mn_{3.03}Sn_{0.97}$ sample, in addition to the metallic nature, a small feature is visible around 200 K. The magnified inset in the figure shows a clear thermal hysteresis, which corresponds to the helical phase transition observed in the magnetic measurements. The thermal hysteresis arises due to the first-order nature of the helical transition. The residual resistivity of the higher electron-doped sample is comparatively larger than other samples. It is even more evident from the room temperature normalized resistivity plots in Fig. 3.6 (b) for the two samples. This

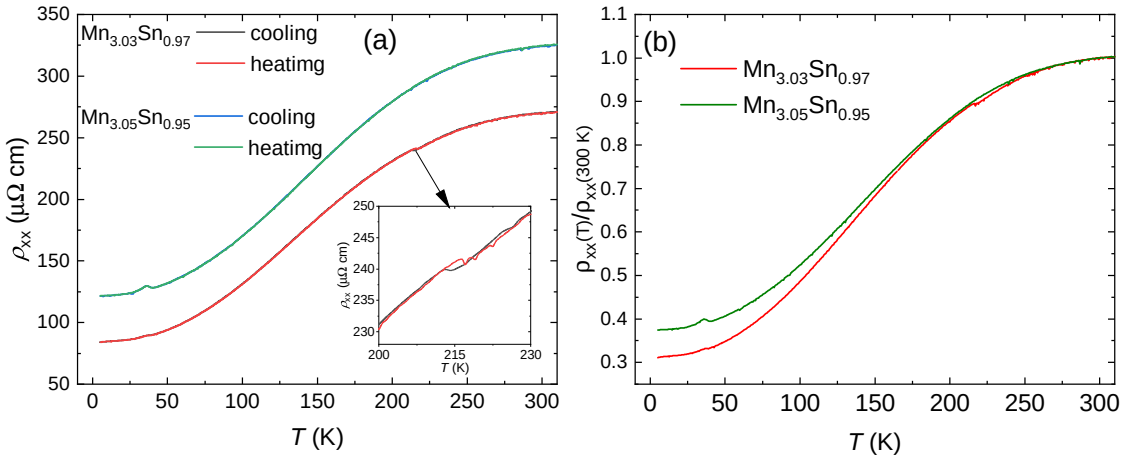

Figure 3.6: (a) Temperature dependent longitudinal resistivity (ρ_{xx}) plots for $Mn_{3.03}Sn_{0.97}$ and $Mn_{3.05}Sn_{0.95}$ samples. Inset shows a magnified view of the temperature around helical transition. (b) $\rho_{xx}(T)/\rho_{xx}(300\ \mathrm{K})$ plot for the two samples.

difference could be a consequence of the extra Mn atoms sitting at the Sn sites. The presence of Mn atoms in place of the Sn atom can lead to an enhanced scattering.

The Hall data at different temperatures are plotted in Fig. 3.7. The samples show a large anomalous Hall signal at 300 K. The presence of the AHE at room temperature reaffirms earlier deductions that the samples stabilize in the iT-AFM magnetic ground state. Below the room temperature, $Mn_{3.03}Sn_{0.97}$ sample does not show any Hall signal in the helical phase. The temperature dependence of Hall resistivity and conductivity is shown in Fig. 3.7 (c-d). These results match well with the earlier prediction that the helical phase does not host any AHE. The absence of the Hall signal is a consequence of the rotating spin structure of the helical phase. The AHE signal from each layer of the helical modulated structure generates a Hall signal in a particular direction. Different layers generate the Hall signal in all directions, making a vanishing the resultant signal. The $Mn_{3.05}Sn_{0.95}$ sample, on the other hand, shows the Hall signal in the whole temperature range. This holds well with the fact that the $Mn_{3.05}Sn_{0.95}$ sample does not show any magnetic transition up to 50 K. The Hall resistivity shows a maximum value at 200 K while the Hall conductivity keeps on increasing till the lowest temperature. These trends match well with earlier results.[42]

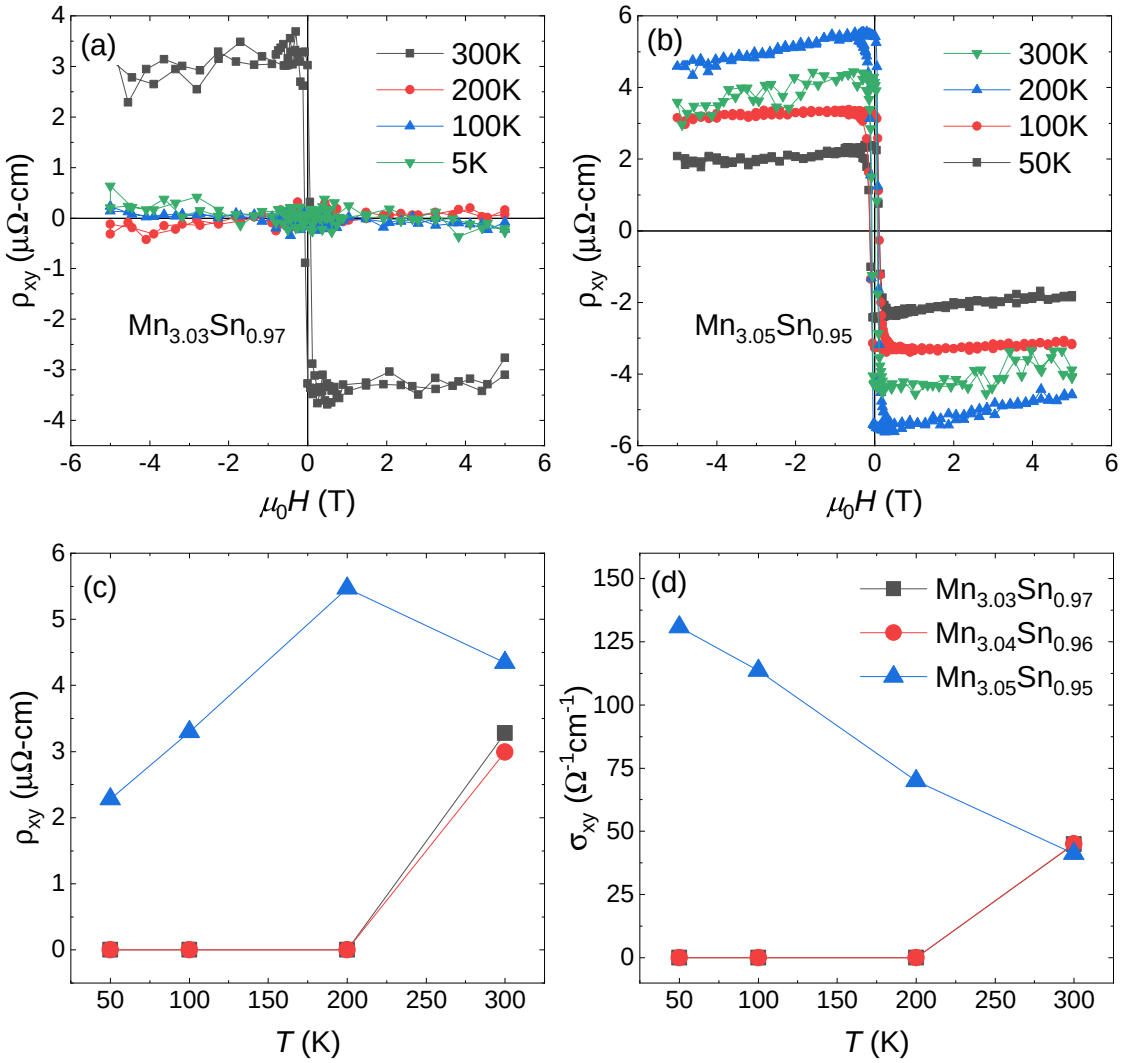

Figure 3.7: Field dependence of Hall resistivity for (a) $Mn_{3.03}Sn_{0.97}$ and (b) $Mn_{3.05}Sn_{0.95}$ samples at different temperatures. Temperature dependence of (c) Hall resistivity and (d) Hall conductivity for three samples.

A correlation between the electron doping and the magnetic ground state has been established. The magnetic, neutron and the transport measurements confirm the presence of the helical phase in $Mn_{3.03}Sn_{0.97}$, whereas it is absent in case of $Mn_{3.05}Sn_{0.95}$ sample. Now that the desired samples have been obtained, the task at hand is to gain a complete understanding of the helical transition. As the helical phase appears with a reduction of temperature, the temperature dependent crystal structure of these samples is studied in details to explore the presence of any

modification of crystal structure due to the helical phase transition.

3.2 Temperature dependence of crystal structure

The temperature-dependent XRD measurements are performed on the $Mn_{3.03}Sn_{0.97}$ and $Mn_{3.05}Sn_{0.95}$ samples to find out the effect of magnetic phase transition on the structure. Figure 3.8 and 3.9 shows the XRD plots for $Mn_{3.05}Sn_{0.95}$ and $Mn_{3.03}Sn_{0.97}$ samples at some temperatures. Both the samples do not show any structural transition up to the lowest temperature measured. Figure 3.10 (a) and (b) shows the temperature variation of lattice parameters extracted from the Rietveld refinement of temperature dependent XRD data. The lattice parameters decrease overall with reducing the temperature for both the samples. However, for the $Mn_{3.03}Sn_{0.97}$ sample, a sudden change in the lattice parameters is observed around the helical phase transition temperature. The lattice parameter a decreases suddenly at the stabilization point of the helical phase, while a small change is also seen in c. The above observation can be seen more clearly in the unit cell volume vs. temperature plot as shown in Figure 3.10 (c) and (d). An abrupt feature is seen for the volume of $Mn_{3.03}Sn_{0.97}$ sample, whereas the $Mn_{3.05}Sn_{0.95}$ does not show any distinguishable feature. This sudden change happens precisely at the helical phase. Thus a correlation can be expected between the lattice size and the magnetic ground state. Motivated by this result, the pressure-dependent magnetic and transport measurements are carried out for these samples.

3.3 Pressure dependent ground state and switching of anomalous Hall effect

The magnetic and transport properties of the samples are characterized as a function of pressure. First the pressure dependent magnetic property is discussed, followed by the discussion of pressure dependent transport properties.

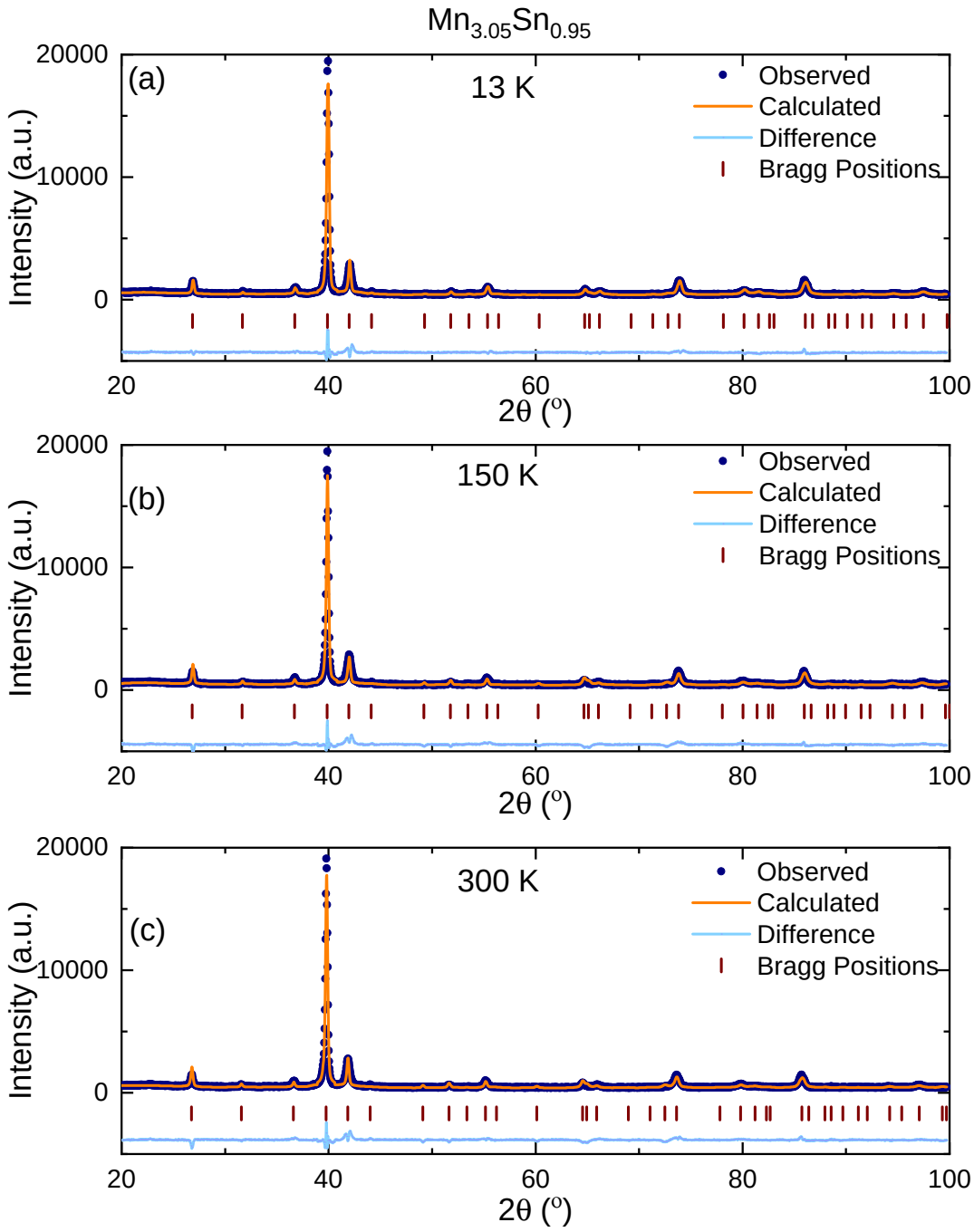

Figure 3.8: Temperature dependent XRD patterns with Rietveld refinement for $Mn_{3.05}Sn_{0.95}$ samples at (a) 13 K, (b) 150 K and 300 K.

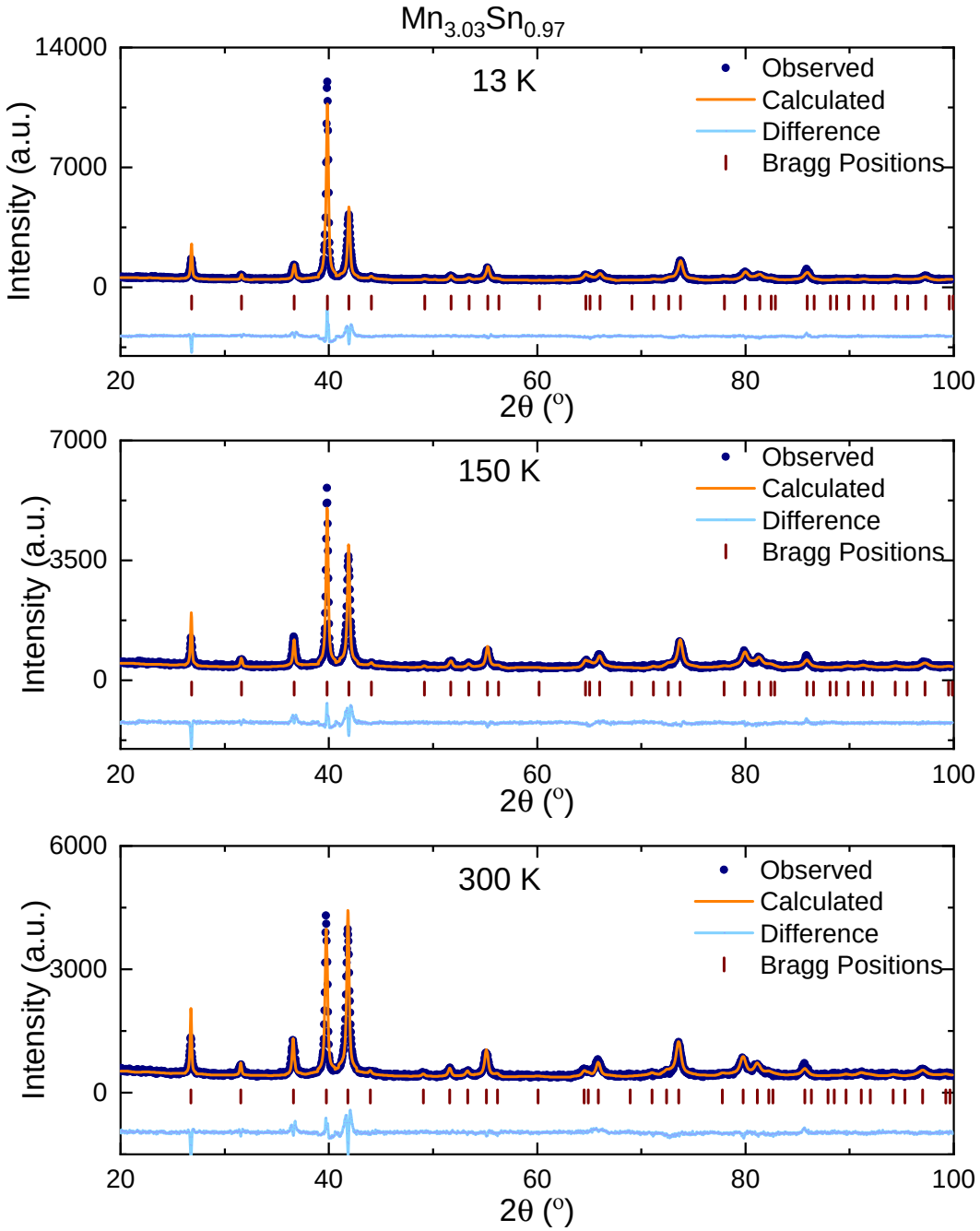

Figure 3.9: Temperature dependent XRD patterns with Rietveld refinement for $Mn_{3.03}Sn_{0.97}$ samples at (a) 13 K, (b) 150 K and 300 K.

3.3.1 Magnetic properties

The pressure dependent magnetic measurements are performed to uncover the role of pressure on the magnetic phase transitions. Figure 3.11 shows the $M(T)$ mea-

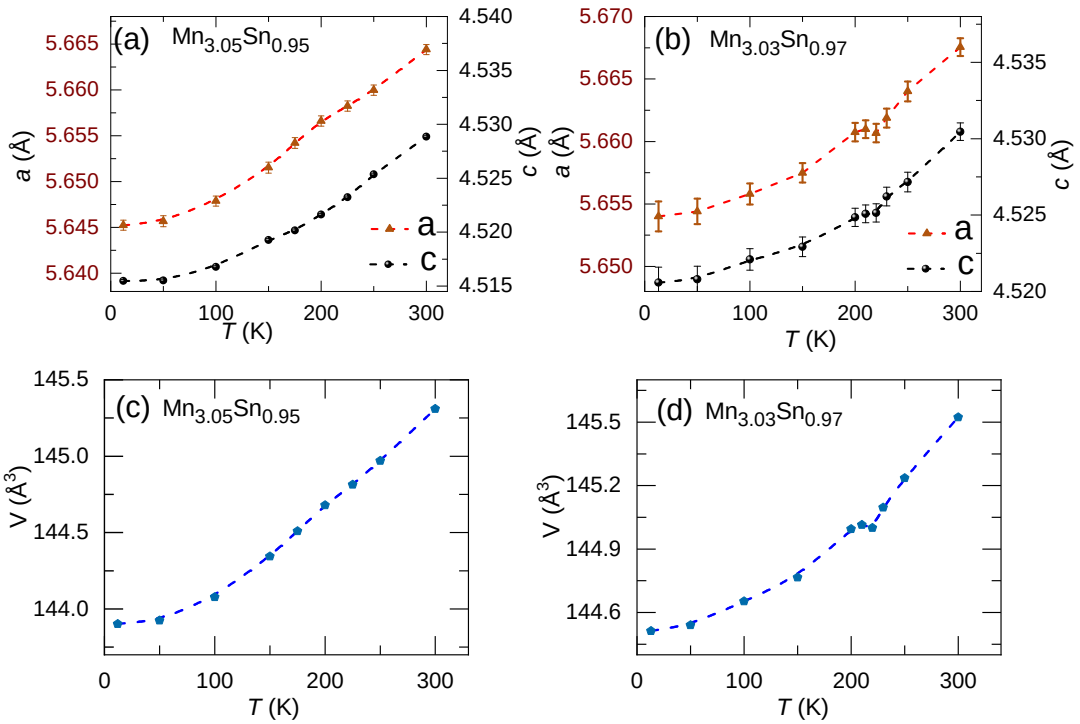

Figure 3.10: Temperature dependent lattice parameters a and c for (a) $Mn_{3.05}Sn_{0.95}$ and (b) $Mn_{3.03}Sn_{0.97}$ sample. (c-d) shows the unit cell volume as a function of temperature for the two samples.

surements performed at different pressure for different samples. For the $Mn_{3.05}Sn_{0.95}$ sample, the application of pressure leads to a modification of the magnetic ground state. Figure 3.11 (a-d) shows the ZFC measurements at different pressure values. The $M(T)$ taken at 0.5 GPa shows similar behavior to that at ambient pressure. However, further increasing the pressure to 0.9 GPa, a transition starts to appear around 150 K. Finally, at a pressure of about 1.2 GPa, the $M(T)$ curve shows a clear transition at 150 K. The transition shows a similar characteristic to that of a helical phase transition found at ambient pressure for $Mn_{3.04}Sn_{0.96}$ and $Mn_{3.03}Sn_{0.97}$. For the $Mn_{3.04}Sn_{0.96}$ sample, the application of pressure shifts the helical phase transition to higher temperatures. Finally, the application of pressure on the $Mn_{3.03}Sn_{0.97}$ sample changes the critical temperature of the helical phase by a small value only.

To gain more insight, the $M(H)$ measurements were performed on $Mn_{3.05}Sn_{0.95}$ sample at 100 K and 300 K. Figure 3.12 shows the field-dependent magnetization

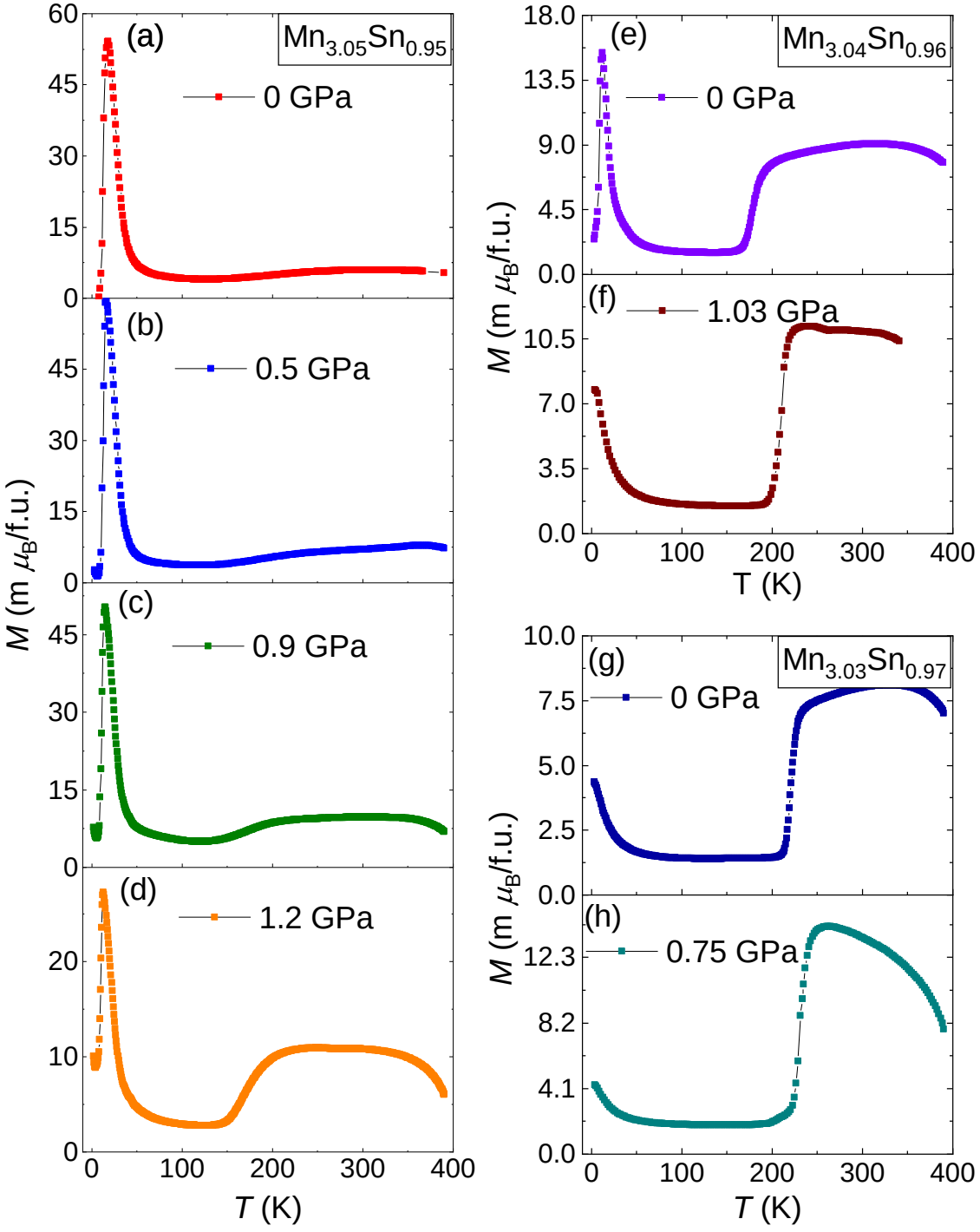

Figure 3.11: Temperature dependent ZFC magnetization curves for (a-d) $Mn_{3.05}Sn_{0.95}$, (e-f) $Mn_{3.04}Sn_{0.96}$ and (g-h) $Mn_{3.03}Sn_{0.97}$ at different values of external pressure.

loops at various pressure values. It is very much evident that the $M(H)$ data at 100 K show a considerable change with the application of pressure. The hysteretic

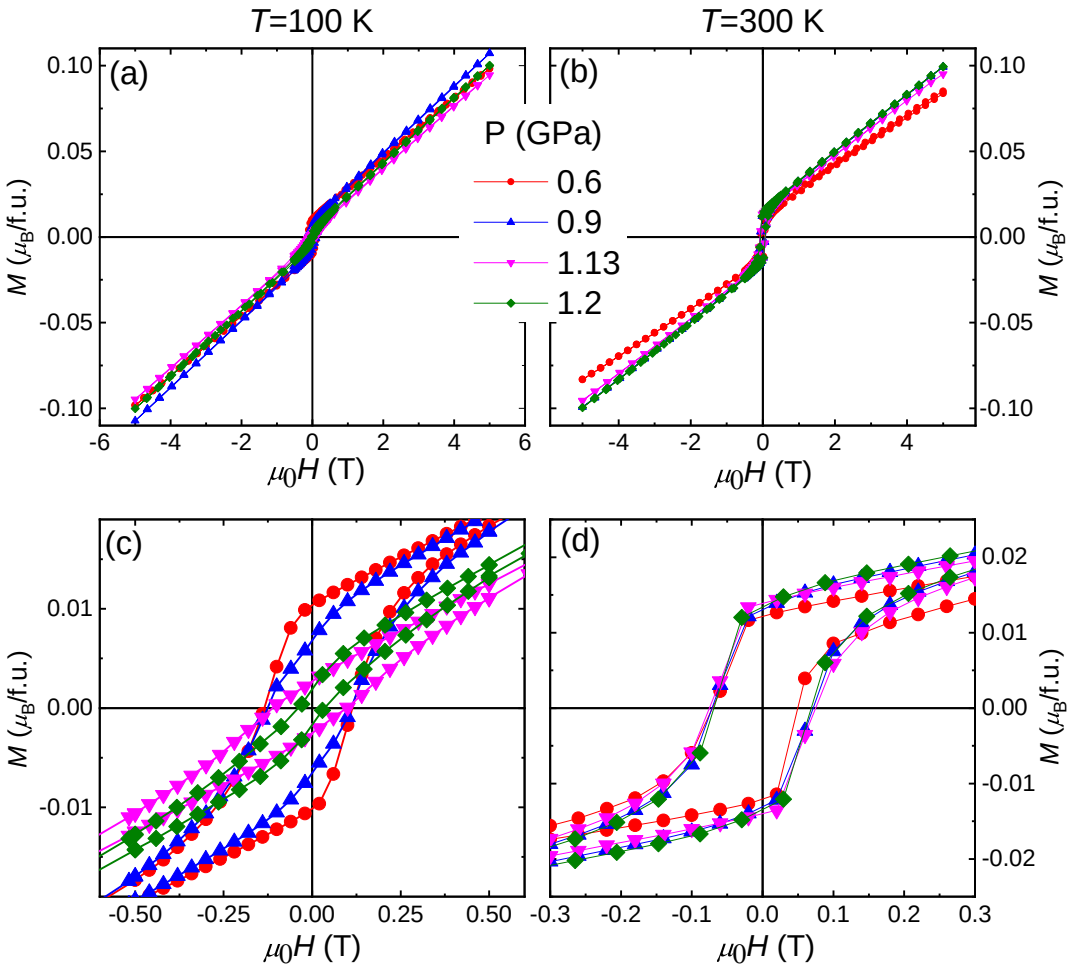

Figure 3.12: (a-d) Field dependent isothermal $M(H)$ loops for $Mn_{3.05}Sn_{0.95}$ sample at 100 K and 300 K under application of different external pressure. The low field region of $M(H)$ data is shown in (c-d) for both temperatures.

behavior of the $M(H)$ loop at ambient temperature changes to a near-linear type with application of pressure. A similar linear $M(H)$ curve is observed in the helical phase of the $Mn_{3.03}Sn_{0.97}$ sample. Thus, the $M(H)$ measurements also point to the stabilization of the helical phase with the application of pressure in $Mn_{3.05}Sn_{0.95}$ sample at 100 K. On the contrary, the $M(H)$ loops at 300 K do not vary with the application of pressure, pointing to a robust iT-AFM state. These magnetic measurements hence point toward increased stability of the helical phase with the application of pressure.

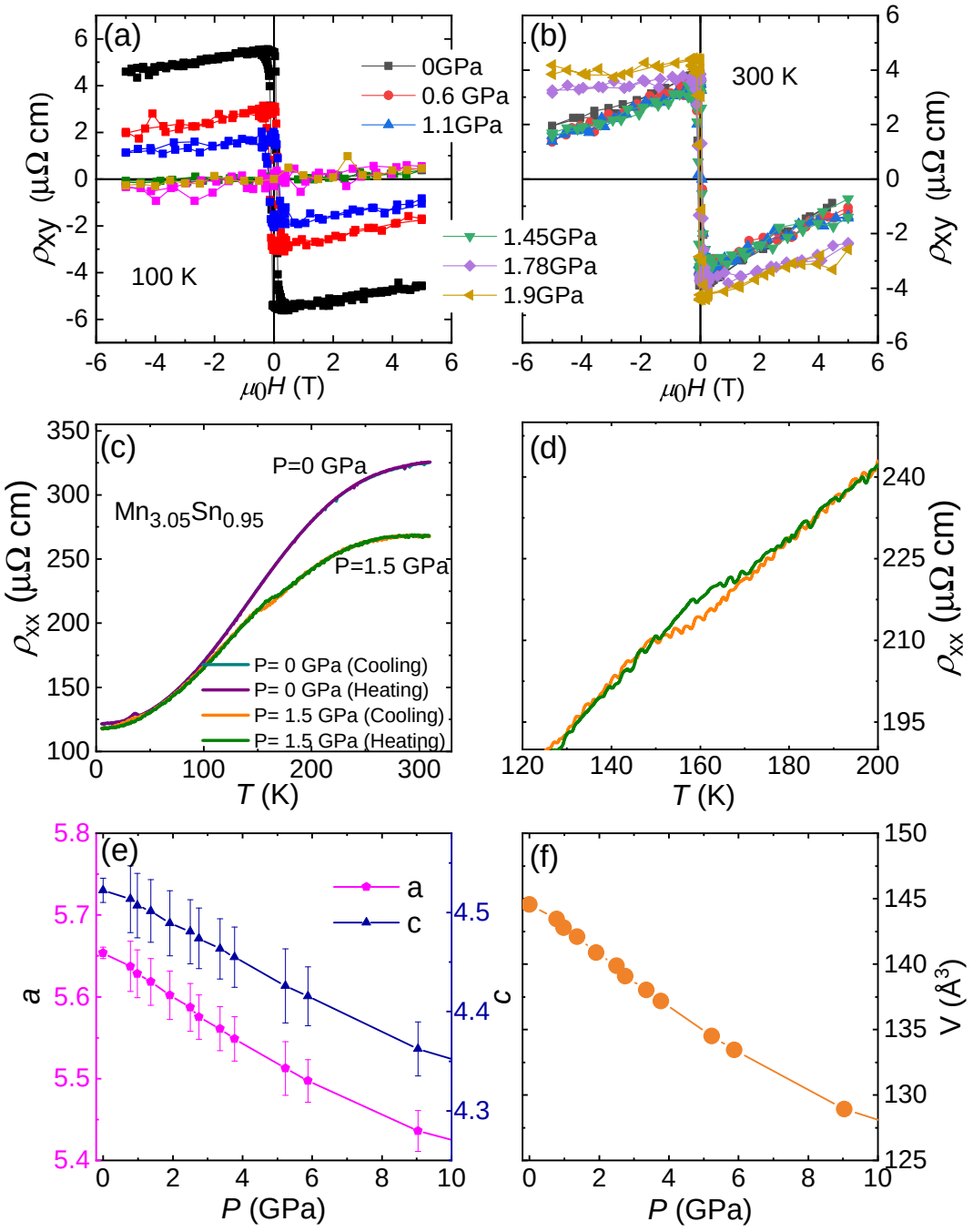

Figure 3.13: (a-b) Field dependent Hall resistivity for $Mn_{3.05}Sn_{0.95}$ sample at 100 K and 300 K under application of different external pressure. (c-d) Temperature dependent zero field longitudinal resistivity measured at 0 GPa and 1.5 GPa pressure for $Mn_{3.05}Sn_{0.95}$ sample. (d) The magnified view around the pressure induced transition. (e-f) Pressure dependent lattice parameters and unit cell volume for $Mn_{3.05}Sn_{0.95}$ sample.

3.3.2 Electronic transport properties

A unique signal to differentiate the helical to iT-AFM state is the presence of large AHE in the iT-AFM state of the sample. This Hall resistivity signal usually is absent for the helical phase. In this regard, pressure-dependent Hall resistivity measurements are performed on the $Mn_{3.05}Sn_{0.95}$ samples. Figure 3.13 (a-b) shows the Hall resistivity as a function of the magnetic field at various pressure values. At room temperature, the application of pressure does not change the Hall signal. This corroborates well with the earlier observation from the magnetic measurements that a robust iT-AFM state is always present at room temperature. At 100 K, it is seen that the Hall resistivity reduces and finally goes to zero with the application of pressure. Figure 3.13 (c-d) shows the longitudinal resistivity vs. temperature plots at different pressure values. It can be seen that the pressure induces a small hysterics behavior in the resistivity data, similar to that of $Mn_{3.03}Sn_{0.97}$ sample. The hysteresis in resistivity data can be clearly seen in the enlarged view plot in Fig. (d). Finally, to verify the nature of the pressure-induced transition, pressure-dependent XRD measurements are performed to rule out any structural phase transition. The lattice parameters as extracted from the pressure-dependent XRD are plotted in Fig. 3.13 (e-f) along with the unit cell volume. No structural transition is observed. The sample shows only a smooth reduction in the lattice parameters up to 10 GPa. Thus the switching of the Hall signal does not depend on the change in the crystal structure, rather entirely a consequence of the pressure-driven transition of the iT-AFM state to a helical modulation.

Thus, the transition of the iT-AFM state to the helical phase can be used to switch the AHE in $Mn_{3.05}Sn_{0.95}$. The switching is brought about by the application of external isotropic pressure.

3.4 Theoretical understanding

The switching of the AHE is brought about in the present case by a change in the magnetic ground state. Thus, understanding the switching process requires untangling the mechanism of helical phase transition. The stabilization of different magnetic states in magnetic materials can be understood in terms of the exchange interaction among the magnetic moments. As discussed in chapter 1, the iT-AFM structure stabilizes by a combination of antiferromagnetic and ferromagnetic exchanges. Two nearest in-plane and out-of-plane exchange parameters were discussed in chapter 1. These exchange parameters are again labeled in Fig. 3.14 of the Mn_3Sn kagome lattice. The sign of the exchange constants up to the second nearest neighbor is in accordance with the observed iT-AFM state. Therefore, we must go beyond the second nearest-neighbor interaction to explore the possibility of stabilizing the helical phase. Additionally, the role of DMI in the stabilization of helical phase can be ruled out based on two observations. First, the helical phase is stable up to very high magnetic fields, which implies stronger interaction at play rather than the comparatively weaker DMI. Secondly, the presence of an inversion center rules out the possibility of any long-range magnetic states stabilized by DMI.[11]

In the helical phase of the Mn_3Sn, the intra-layer 120° spin structure remains unchanged, i.e., the angle between spins in a single layer remains constant. However, a finite rotation is observed between spins when we move along the *c*-axis. Thus, any role of intra-layer exchange interaction can safely be excluded for the stabilization of the helical phase. Therefore, only the inter-layer or out-of-plane exchange parameters will be considered. The three nearest inter-layer exchange parameters are labeled in Fig. 3.14 (b). The sign of the first two has already been discussed, with J_1^{out} being AFM and J_2^{out} being FM in nature. Figure 3.14 (c-d) shows the total number of neighboring sites corresponding to J_1^{out} and J_2^{out}. The magnetic moments for J_1^{out} pairs lie at 120° to each other, which is a minimum energy state for AFM exchange in a triangular lattice. The moments for J_2^{out} are parallel to each other, which also is a minimum energy state for the ferromagnetic J_2^{out}. The third nearest

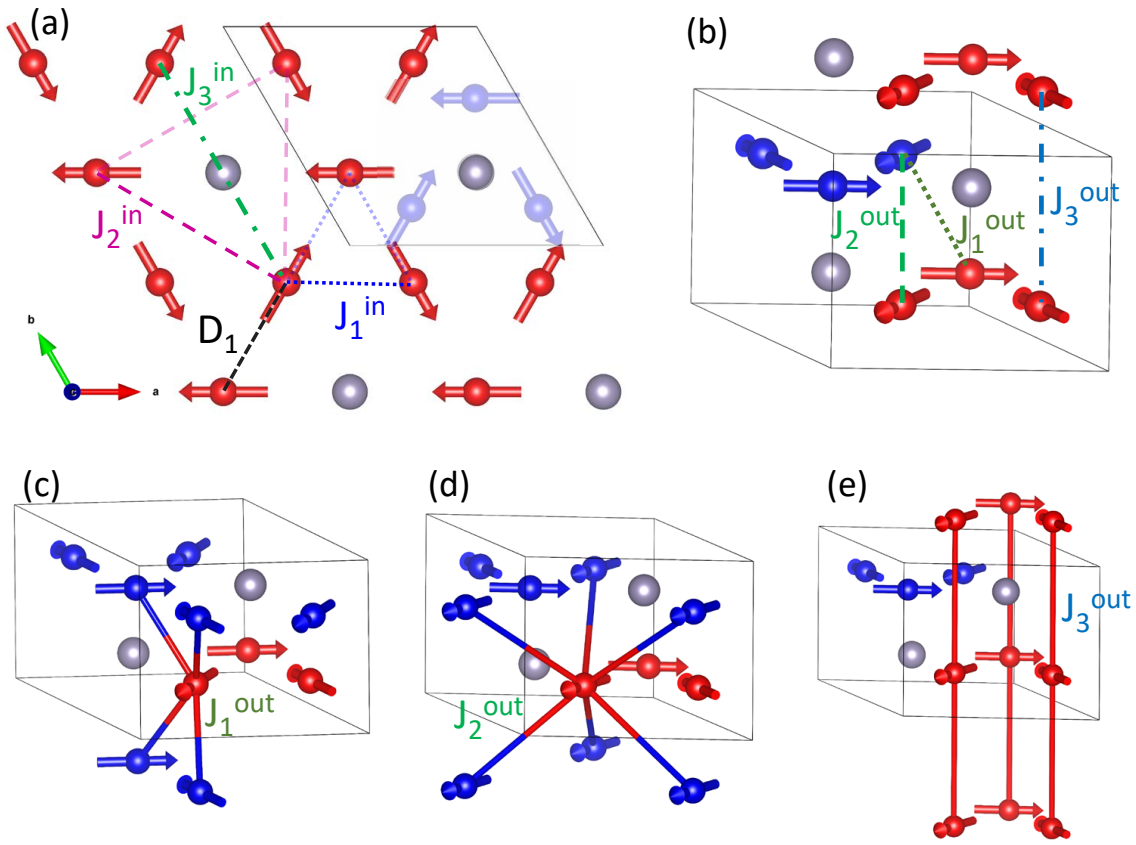

Figure 3.14: A schematic of the kagome lattice structure of Mn_3Sn showing three nearest neighbor (a) intra-plane and (b) inter-layer exchange parameters. The number of nearest neighbor for Mn atoms are represented in (c) for J_1^{out}, (d) J_2^{out} and (e) J_3^{out}. The arrows indicate the direction of magnetic moments.

exchange parameter connects spins in the next neighbor layer along the *c*-axis [Fig. 3.14 (b,e)]. The spins corresponding to this exchange interaction are parallel in the case of the iT-AFM structure. This is clearly visible in Fig. 3.14 (e), where the J_3^{out} neighbors for a site are shown. As it is discussed in chapter 1, the exchange frustration can stabilize a helical phase. For the present case, where the J_1^{out} and J_2^{out} energy is minimum when spins for J_3^{out} are parallel, exchange frustration can only arise if the J_3^{out} is antiferromagnetic. Thus a spin spiral state can be stabilized due to a competition between the ferromagnetic J_2 and antiferromagnetic J_3.

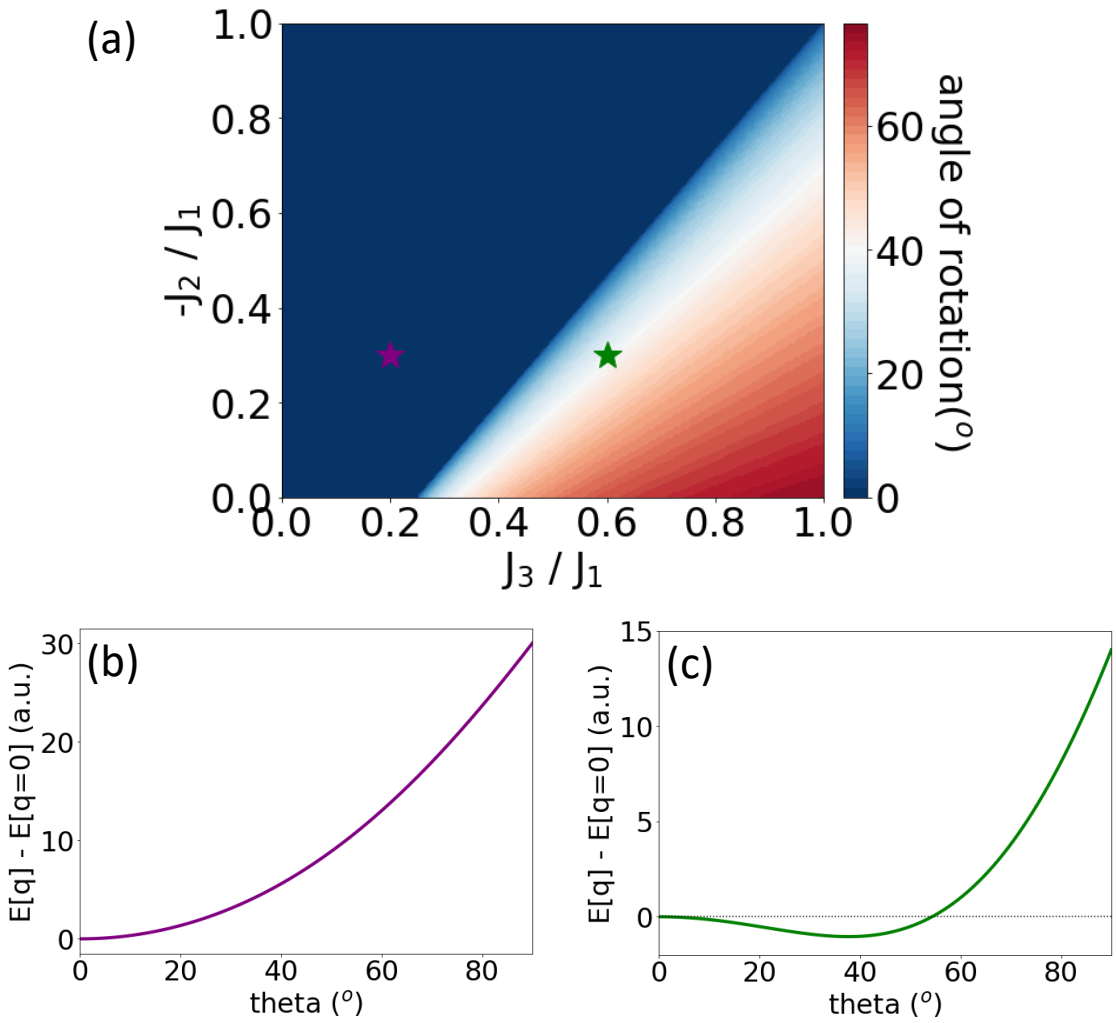

Figure 3.15: (a) Phase diagram of minimum energy θ value as calculated for various values of exchange J_2^{out} and J_3^{out}. The curves corresponding to purple and green star are shown in (b) and (c) respectively.

3.4.1 Analysis of exchange Hamiltonian

To explore the possibility of stabilizing a helical phase, the exchange Hamiltonian with three inter-layer exchange interactions is utilized. The exchange Hamiltonian for a single site can be written as

$$H = 4J_1^{out}\cos(\frac{2\pi}{3}) + 6J_2^{out}\cos(0) + 2J_3^{out}\cos(0). \tag{3.1}$$

The helical phase induces a finite rotation between the magnetic moments when moving along the c-axis. The spins in the $+c$ direction are rotated by an angle θ from the reference layer, while spins in the -c direction are rotated by -θ. Thus, the Hamiltonian of the system in this case can be written as

$$H = 2J_1^{out}\cos(\frac{2\pi}{3}+\theta) + 2J_1^{out}\cos(\frac{2\pi}{3}-\theta) + 6J_2^{out}\cos\theta + 2J_3^{out}\cos(2\theta). \quad (3.2)$$

Here, the value of θ depends on the q vector of the helical modulation, and $\frac{2\pi}{3}$ in J_1 is the initial phase between two consecutive Kagome sublattices. Using the above equation, the exchange energy as a function of θ is evaluated. The value of J_2^{out} and J_3^{out} is varied in the range 0-1 J_1^{out}, where J_3^{out} is taken as AFM. The minima in energy lie at 0^circ for the iT-AFM state and at finite θ for spin spiral states. The typical plots for these two scenarios look like that in Fig. 3.15 (b-c). For Fig. 3.15 (b), the iT-AFM state is stable as energy is minimum at $\theta = 0$. For the second plot, a spiral state is stabilized with a finite value of θ. The full results are summarized in the J_2^{out} vs. J_3^{out} phase diagram presented in Fig. 3.15 (a).

It is observed from the phase diagram that a region exists in the phase diagram where the θ is finite, thus confirming the suggestion that the exchange frustration can stabilize the helical phase. Secondly, there exists a minimum value of J_3^{out}, after which the iT-AFM state transforms into the helical phase for a given value of J_2^{out}. Naturally, the minimum value increase to larger values for an increase in the strength of J_2^{out}. This is expected as the J_2^{out} 'fights' for the iT-AFM structure while J_3^{out} tries stabilizing a helical phase. Thus the helical phase can be stabilized due to exchange frustration among the out-of-plane exchange interactions.

3.4.2 The real Mn_3Sn Kagome lattice : Effect of trimerization

Although the above discussed exchange model can explain the stabilization of helical magnetic ground state, it is found that the crystal structure of Mn_3Sn possesses a

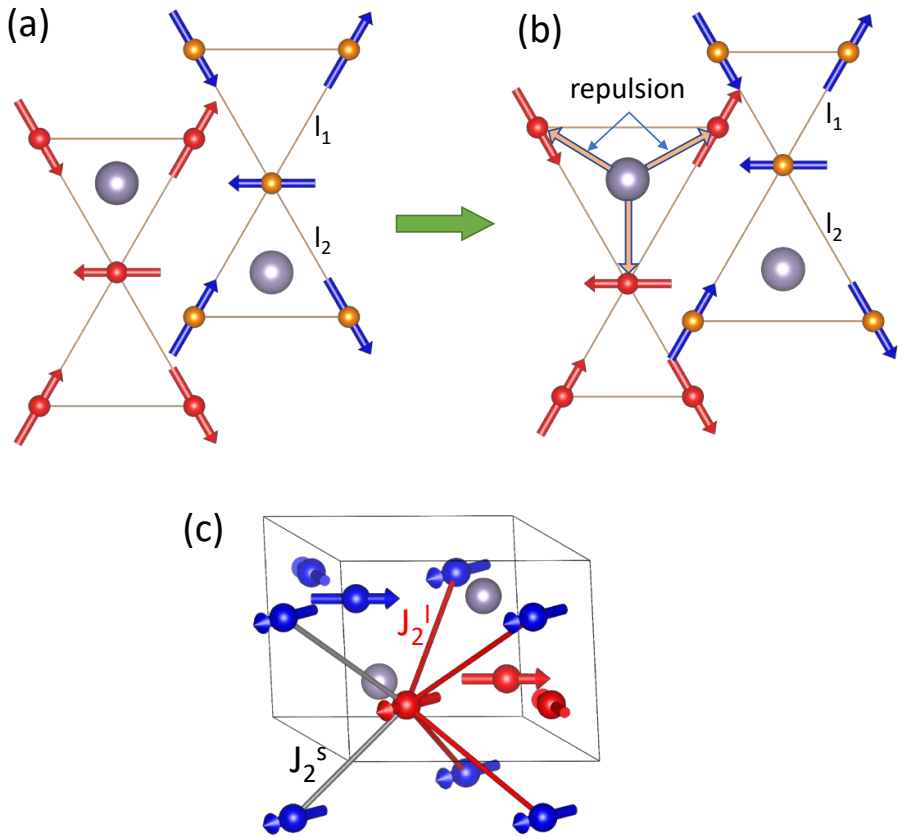

Figure 3.16: The crystal lattice of Mn_3Sn with an (a) ideal kagome lattice, and (b) trimerized lattice. The lengths of two corner sharing triangles are marked. (c) The number of neighbors corresponding to the spitted J_2^{out} are shown by gray and red lines joining the Mn sites.

little quirk that has gone unnoticed till now. The usual kagome lattice comprises equilateral triangles connected at a common point, where two nearby triangles are of equal in size [Fig. 3.16 (a)]. However, in the case of Mn_3Sn, the two nearby triangles are unequal. This is a consequence of the layered structure of the Mn_3Sn, where electrostatic interaction between the Sn atoms in one layer and the Mn atoms in the other layer makes one of the Mn triangles larger than other [Fig. 3.16 (a)]. This phenomenon is termed trimerization, while the structure is referred to as the breathing kagome lattice. The extent of trimerization can be quantified using the trimerization parameter $\delta = \frac{l_2 - l_1}{l_2 + l_1}$, where l_1 and l_2 are the bond lengths for the smaller and larger triangles. A consequence of the trimerization is the splitting of the bond for J_2^{out} into two different bonds, one larger and one smaller than the earlier

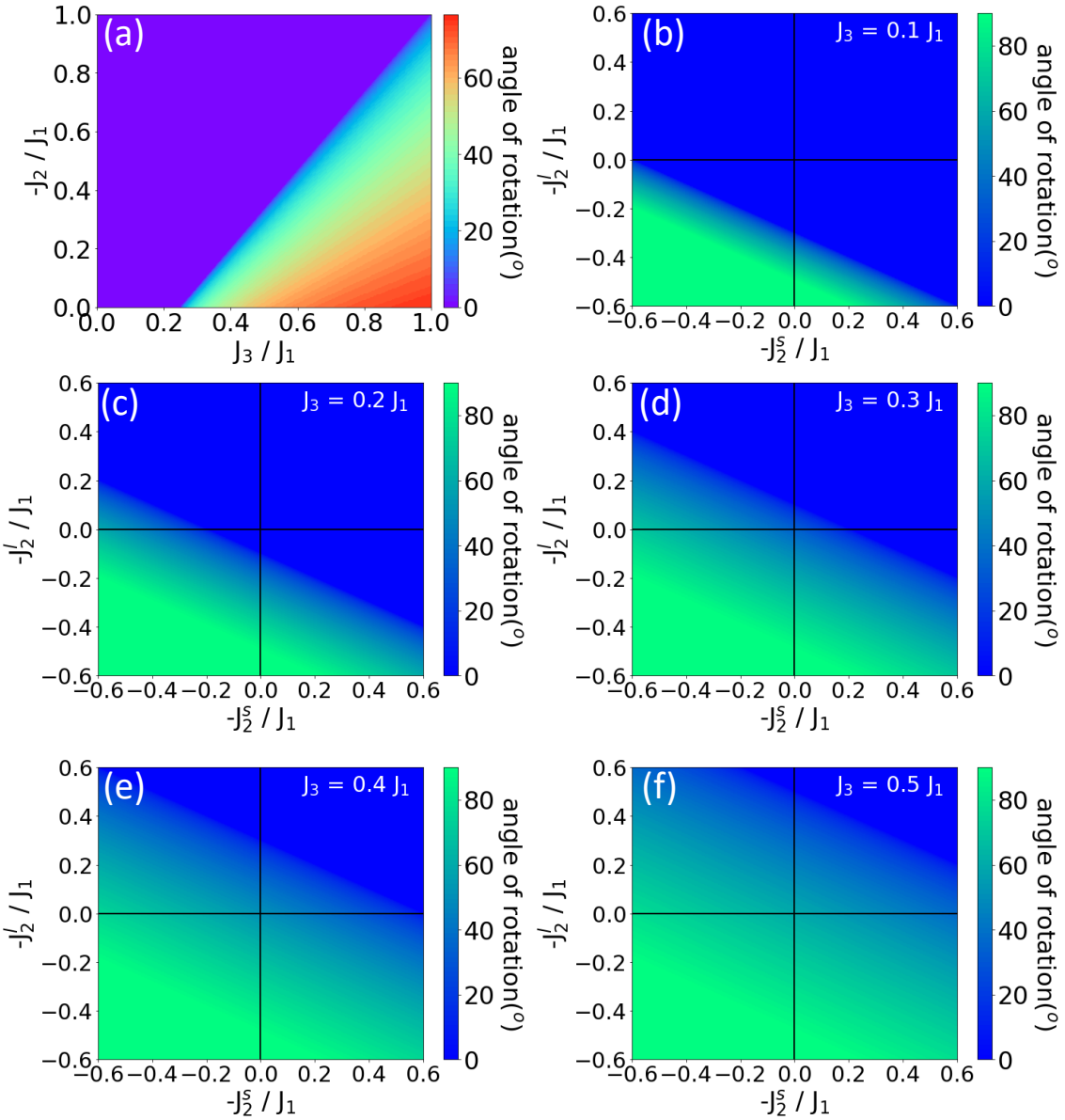

Figure 3.17: (a) Phase diagram of minimum energy θ value as calculated for various values of exchange J_2^{out} and J_3^{out} for the ideal kagome structure. (b-f) J_2^s and J_2^l phase diagram of minimum energy θ for the trimerized structure at different J_3^{out}.

one. The Heisenberg J's corresponding to these bonds is denoted by J_2^s and J_2^l for the smaller and larger bond, respectively. The J_2^s and J_2^l are marked by grey and red lines in Fig. 3.16 (c).

While the general information about the relative strength of J_2^{out}/J_3^{out} for helical phase stabilization still holds for the trimerized structure, certain deviations are

expected. Although the length of l_1 and l_2 change by the same amount, the strength of the exchange parameters do not change equally. In addition, the J_2^{out} comes with six neighbors, three in the upper and three in the bottom layers. However, after trimerization, the small and large triangles do not share equal neighbors, instead the larger one gets four, and the smaller gets two [Fig. 3.16 (c)]. The new exchange Hamiltonian for the trimerized Mn_3Sn lattice can be written as

$$H = 2J_1\cos(\frac{2\pi}{3}+\theta) + 2J_1\cos(\frac{2\pi}{3}-\theta) + 2J_2^l\cos(0+\theta) + 2J_2^l\cos(0-\theta) + J_2^s\cos(0+\theta) + J_2^s\cos(0-\theta) + J_3\cos(0+2\theta) + J_3\cos(0-2\theta) \quad (3.3)$$

The effect of trimerization is investigated by calculating the exchange Hamiltonian 3.3. The J_2^s and J_2^l exchange are modified in units of J_1^{out} for different values of J_3^{out}. Figure 3.17 shows the phase diagrams for positive and negative values of J_2^s and J_2^l. The phase diagram for the ideal kagome case is also plotted for reference. The J_2^s vs. J_2^l phase diagrams are calculated for different values of J_3^{out}, which are marked in Fig. 3.17 (a). First, we look at the phase diagram for $J_3^{out} = 0.2\ J_1^{out}$. This value is below the critical value for the stabilization of the helical phase in the ideal kagome structure. Thus a $\theta = 0$ state is found in the whole first quadrant. However, a finite theta region is found for opposite values of J_2^s and J_2^l. The negative values mean an antiferromagnetic J_2^{out}, which now fights against the iT-AFM state and favors a helical phase. A sharp boundary is present in separating the non-helical from the helical phase. This boundary moves to cover a larger part of the phase diagram as the value of J_2^{out} increases.

To summarize the Hamiltonian analysis, exchange frustration among the out-of-plane Js can stabilize the helical phase. The ferromagnetic J_2^{out} tries to stabilize the iT-AFM state while an AFM J_3^{out} destabilizes it. Thus the appreciable value of J_3^{out} is required to stabilize the helical phase. Additionally, the trimerization can help in stabilizing the helical phase due to dissimilar changes in the strength of J_2^s and J_2^l. To establish the above findings and understand the role of pressure on the

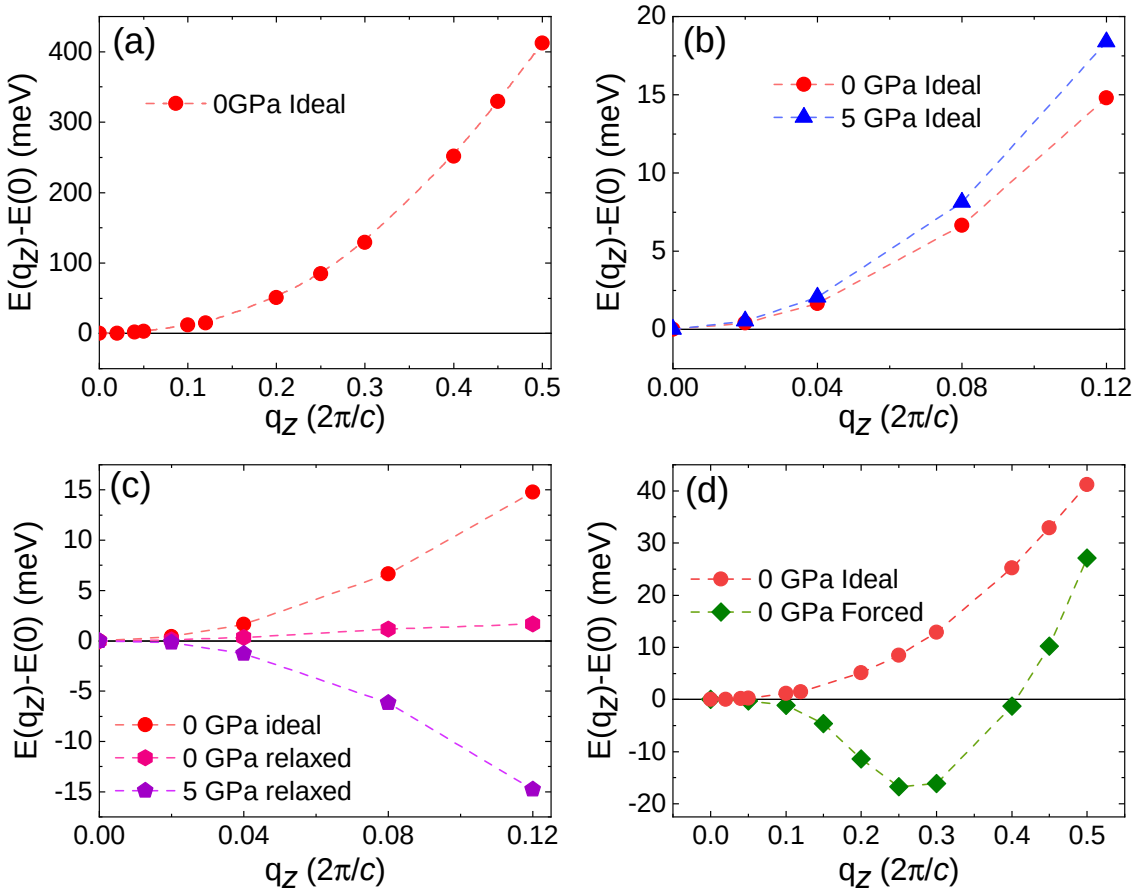

Figure 3.18: Spin spiral calculated energies as a function of q for different condition of the Mn_3Sn unit cell.

helical transition, DFT calculations are performed for Mn_3Sn lattice using VASP and FLEUR packages.

3.4.3 *ab-initio* calculations

The spin spiral (SS) calculations are performed using the FLUER code. The q=0 state is set to be the iT-AFM state. First, the SS calculation is performed using the Mn_3Sn experimental lattice parameters and an ideal kagome lattice. Figure 3.18 (a) shows the q vs. δE plots for the ideal kagome at 0 GPa. It can be seen that the energy minima lie at q = 0, and the iT-AFM is the ground state. Next, the calculations for the pressure of 5 GPa are carried out. The pressure was incorporated by using the experimental lattice parameters. However, the application of pressure

Table 3.2: δ, the measure of effective trimerization at different pressure values in case of ideal and relaxed structures along with Mn Wyckoff position.

Pressure (GPa)	x (6c: x,2x,0.25)	δ (10^{-2})
0.0 (ideal)	0.1666	0.0
5.23 (ideal)	0.1666	0.0
0.0 (relaxed)	0.1626	2.4
2.75 (relaxed)	0.1605	3.7
5.23 (relaxed)	0.1493	10.3
0.0 (forced)	0.1466	12.0

even deteriorates the situation further. Here, not only does the ground state lie at $q = 0$, but the energy cost for stabilizing a helical phase increases [Fig. 3.18 (b)]. Thus, applying pressure on an ideal kagome net alone can not explain the experimental observation of change in the ground state. Hence, the above-discussed trimerization must play a definite role in stabilizing the helical phase.

Next, the trimerized lattice of Mn_3Sn is used for the SS studies. The structural relaxation of the Mn_3Sn unit cell is performed using the VASP code. The unit cell size and volume are fixed for the structural relaxation, while the ionic positions are relaxed to find the minimum energy crystal structure. The trimerized state is allowed by the symmetry of the (x,2x,0.25) lattice position. After relaxation, the value for the x is obtained, and the results are listed in the table 3.2. It is observed that the trimerization parameter δ increases with increasing pressure. Figure 3.18 (c) shows the SS calculated energy for the relaxed lattice for 0 GPa and 5 GPa. The SS data for the ideal 0 GPa case is also plotted for reference. For the relaxed 0 GPa structure, the energy cost to stabilize a spin spiral reduces drastically, but the ground remains in the iT-AFM state.

Table 3.3: Out-of-pane exchange parameters as extracted by fitting the $E(\mathbf{q})$ vs q curves with the usual exchange Hamiltonian.

	J_1^{out} (meV)	J_2^{out} (meV) [-J_2/J_1]		J_3^{out} (meV) [J_3/J_1]
		J_2^l (meV) [-J_2^l/ J_1]	J_2^s (meV) [-J_2^s/J_1]	
0 GPa (Ideal)	20.83	-9.29 [0.445]		7.09 [0.340]
0 GPa (Forced)	13.12	-0.32 [0.024]	2.59 [-0.197]	4.41 [0.336]

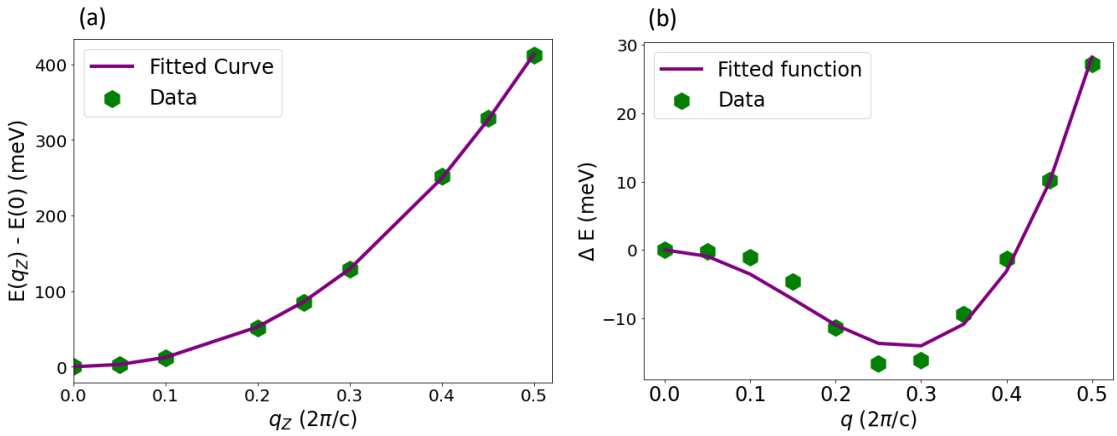

Figure 3.19: Spin spiral energies (green symbols) and the fitting (purple line) with eq. 3.3 for 0 GPa (a) ideal and (b) forced lattice structure.

On the other hand, the q vs. δE trend for the 5 GPa relaxed case changes drastically. The energy curve for the finite q now displays a negative slope, opposite to that of a positive one found for others. This implies that a minimum in energy is to be found at a finite value of the q vector. It implies that the pressure on the lattice increases the extent of trimerization, which then leads to the stabilization of the helical phase. To clearly establish the effect of trimerization, the SS calculations are performed with a forced trimerization case for the 0 GPa case. For this case, the extreme trimerization also results in the stabilization of the helical phase. The SS curves for the 0 GPa ideal and forced structure are fitted with eq. 3.3. The data and the corresponding fitting curves are shown in Fig. 3.19. The fitting parameters are tabulated in table 3.3. For the 0 GPa ideal lattice, the fitting reveals a dominant J_1^{out}. The positive sign here implies an AFM exchange. Additionally, a ferromagnetic J_2^{out} and an AF J_3^{out} are also obtained. Although the extracted sign of J_3^{out} is AFM in nature, the relative strength of J_3^{out} is not large enough to stabilize a helical phase. For the forced trimerization case, the relative strength of J_3^{out} is nearly the same as the case of the ideal case, but a large change is observed for the splitted J_2^{out}. The trimerization leads to a large reduction in the strength of J_2^l, while a change in sign is observed for J_2^s. This change in sign can lead to the stabilization of helical phase, as can be interpreted from the phase diagrams plotted in Fig. 3.17. Thus, the

pressure-induced trimerization is the main driving force behind the transformation of the iT-AFM state to a helical modulated magnetic state.

3.5 Conclusion

The switching of the anomalous Hall signal is a highly studied topic for future technological applications. In ferromagnetic materials, switching of the Hall signal is commonly accomplished by changing the ferromagnetic order parameter. The same method has also been used for Mn_3Sn, where the octupole order is reversed by employing a magnetic field or electric current. The results presented in the current chapter show a pressure-induced switching of the anomalous Hall effect. The mechanism of helical phase transition is uncovered using a combination of experimental and theoretical studies. It is found that the trimerization of kagome lattice can drive the helical phase transition. In addition, the trimerization can be controlled using the external pressure. This new mechanism to switch the anomalous Hall effect expands the prospect of device based on antiferromagnetic materials.

Chapter 4

Higher order exchange interaction driven noncoplanar magnetic state in Mn_3Sn

The last chapter was mainly focused on the temperature-dependent modification of the magnetic ground state of layered kagome compound Mn_3Sn. However, the analysis of the ground state was limited to temperatures greater than 50 K. The present chapter deals with the magnetic ground state at the lowest possible temperatures and its origin in Mn_3Sn. The most important factor that motivates us to study the low-temperature magnetic ground is that the nature of magnetic ordering at the said temperature regime was unclear till the present study. As discussed in chapter 1, the magnetic ground state of a system controls various observable physical properties. The electronic, as well as the magnonic and phononic dispersion, depend strongly on the magnetic ground state. Thus, resolving the low-temperature magnetic ground state can reveal more details about the magnetic interactions and energy landscape of the present system.

The only information available in literature beforehand about the low temperature magnetic state was the formation of glassy ferromagnetic phase.[68] It was shown that the real part of susceptibility exhibits a spin glass signature, along with the an

additional ferromagnetic contribution. It was suggested that a long-range dominant ferromagnetic order may present in the sample.[68] The presence of the spin glass signal on top of the ferromagnetic phase was ascribed to the disordered occupation of Mn atoms at Sn sites for $Mn_{3+x}Sn_{1-x}$ samples. However, no clear understanding of the long-range ferromagnetic order or the mechanism of the magnetic ground state is achieved so far. This chapter answers these questions through rigorous magnetic, electronic transport, neutron diffraction, and theoretical studies. In doing so, a 'new' Hall signal arising from the non-coplanar magnetic ground state is brought into the light. Furthermore, the phenomena of dual magnetic ordering in a sample is seen for the first time. The current chapter also establishes the presence of higher-order exchange interaction, which modifies the energy landscape of magnetic interactions in this well-studied kagome material.

The journey to uncover these properties again starts with the process of synthesizing a suitable set of samples. As we learn in chapter 3, a correlation exists between the magnetic ground state and the electron doping of the samples. A close look at the Fig. 3.2 tells us that the high electron doping stabilizes samples with only the low-temperature transition. Motivated by this, a series of electron-doped samples were synthesized for the current study. As the samples beyond the doping of $Mn_{3.09}Sn_{0.91}$ could not be acquired, a series of samples with $Mn_{3-x}M_xSn$ were synthesized. A natural candidate for the M element is the Fe atom, which has one additional electron than Mn atoms. Thus, the Fe doping was chosen to expand the limits of the possible electron doping and minimize the disordered occupation of the Mn atoms at the Sn sites. Moreover, the Fe atoms also show large magnetic moment which preserves the magnetic site and allows for synthesizing large doping samples. In this regard, samples with composition $Mn_{3.09}Sn_{0.91}$ and $Mn_{3-x}Fe_xSn$ are synthesized. As the Mn_3Sn samples exhibit highly anisotropic magnetic properties, the samples are synthesized in a single crystalline form to extract the exact orientation-dependent physical properties. The synthesis details can be found in chapter 2.

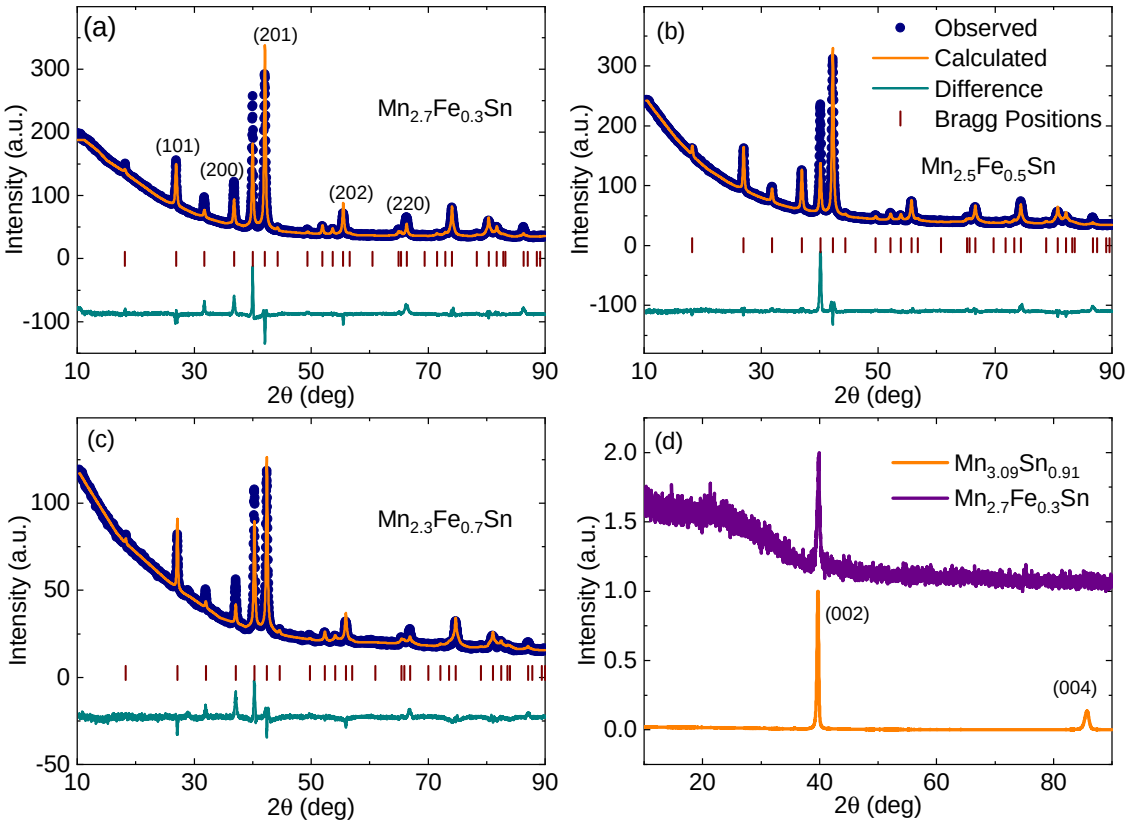

Figure 4.1: XRD patterns with Rietveld refinement for the polycrystalline (a) $Mn_{2.7}Fe_{0.3}Sn$, (b) $Mn_{2.5}Fe_{0.5}Sn$, and (c) $Mn_{2.3}Fe_{0.7}Sn$ samples. Some high intensity peaks are labeled in (a). The legends for the first three plots are shown in (b). (d) XRD pattern as recorded for the (001) face of single crystal samples.

4.1 Structural characterization of $Mn_{3-x}Fe_xSn$ samples

The polycrystalline samples are prepared for the series $Mn_{3-x}Fe_xSn$, for x = 0.3, 0.5 and 0.7. The single crystal of $Mn_{3.09}Sn_{0p91}$, $Mn_{2.7}Fe_{0.3}Sn$ and $Mn_{2.5}Fe_{0.5}Sn$ are also synthesized. Figure 4.1 shows the powder XRD patterns for the polycrystalline samples. The Rietveld refinement for all the samples are also shown in the figure. All the observed reflections are well accounted for the hexagonal crystal structure of the sample.

The XRD analysis confirms that the electron doping does not alter the crystal structure of the samples. The extracted lattice parameters are tabulated in the Table 4.1. The lattice parameters a and c monotonically decrease with increasing Fe doping levels.

Table 4.1: Lattice parameters of $Mn_{3-x}Fe_xSn$ samples.

	a	c
Mn_3Sn	5.65	4.52
$Mn_{2.7}Fe_{0.3}Sn$	5.63	4.50
$Mn_{2.5}Fe_{0.5}Sn$	5.60	4.49
$Mn_{2.3}Fe_{0.7}Sn$	5.59	4.47

For the single crystalline samples, Fig. 4.1 (d) shows the recorded XRD patterns. It can be seen from the figure that the XRD patterns of $Mn_{3.09}Sn_{0p91}$ and $Mn_{2.7}Fe_{0.3}Sn$ only show the (002) and (004) peaks. As the XRD pattern was taken on the c plane of crystals, the observation of only two high intense reflections confirms the single crystalline nature of the samples. A good XRD pattern for the $Mn_{2.5}Fe_{0.5}Sn$ could not be recorded due to very small size of the obtained crystals. However, the morphology and the subsequent magnetic characterization confirm the samples to be of single crystalline nature.

EBSD charaterization of single crystal samples : Additionally, the Electron Backscatter Diffraction (EBSD) measurements[82] are performed to check the single-crystalline nature of the samples. The EBSD patterns are recorded on different samples at various positions. All the samples show the same orientation of the crystals. Figure 4.2 shows the EBSD patterns for the three samples recorded on the [0001] face of crystals. The EBSD data also confirms the [0001] orientation of samples, as is visible from the graphs. The data of $Mn_{2.5}Fe_{0.5}Sn$ sample is comparatively noisy due to the small size of the crystal, which makes it challenging to obtain a well-polished face to perform EBSD measurements.

4.2 Compositional analysis

To check the compositional homogeneity, the FESEM measurements are performed on the $Mn_{3-x}Fe_xSn$ sample as shown in Figure 4.3. The homogeneous contrast of these images confirms the formation of single phase for all the samples. The exact

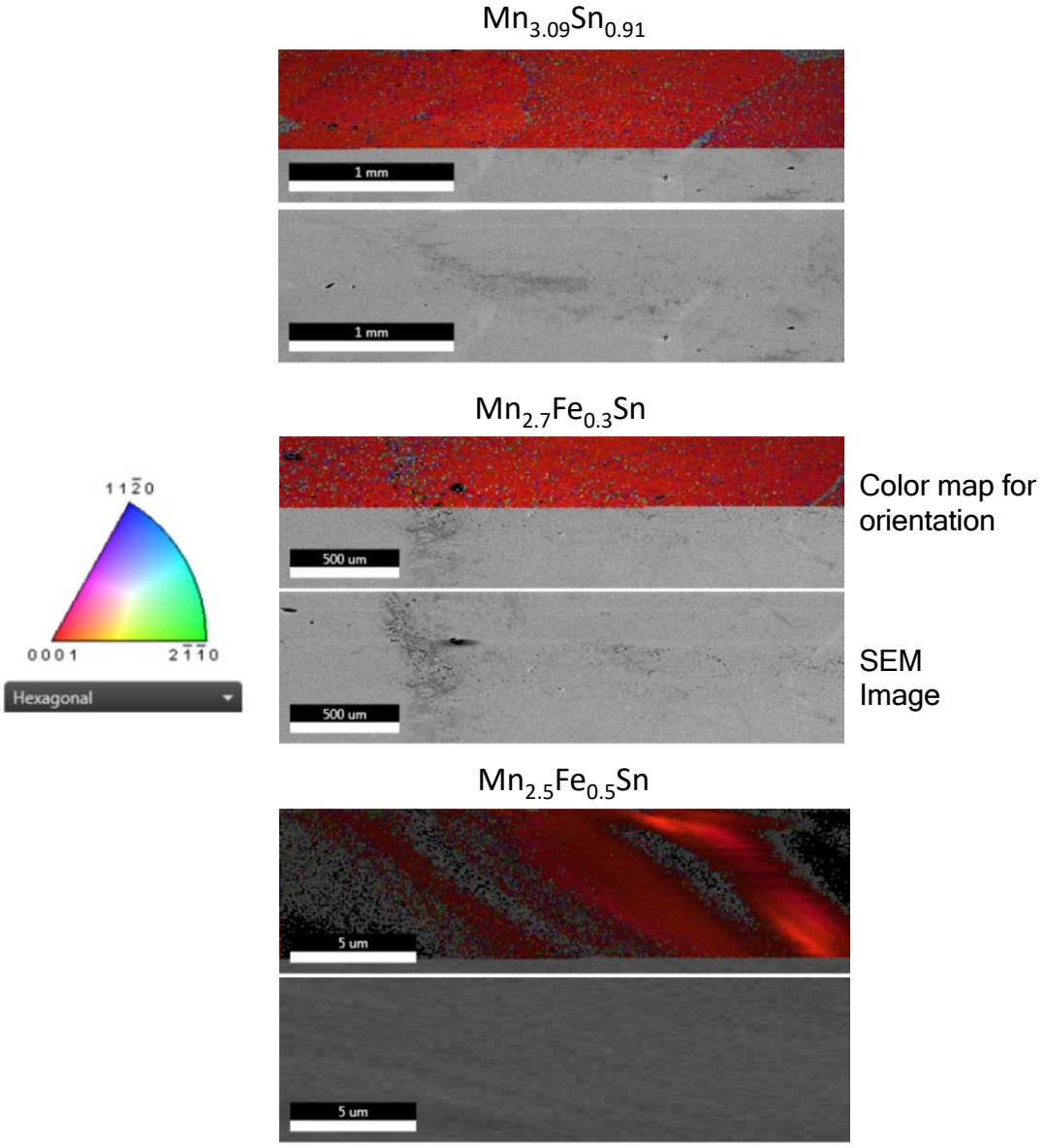

Figure 4.2: Recorded EBSD patterns for (a) $Mn_{3.09}Sn_{0p91}$, (b) $Mn_{2.7}Fe_{0.3}Sn$ and (c) $Mn_{2.5}Fe_{0.5}Sn$ samples.

stoichiometry of the samples is studied with help of the EDS measurement and nearly matched with the expected value.

(a) $Mn_{3.09}Sn_{0.91}$

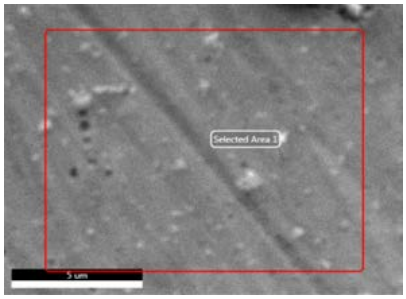

Element	Weight %	Atomic %	Error %
SnL	37.5	21.7	2.2
MnK	62.5	78.3	2.4

(b) $Mn_{2.7}Fe_{0.3}Sn$

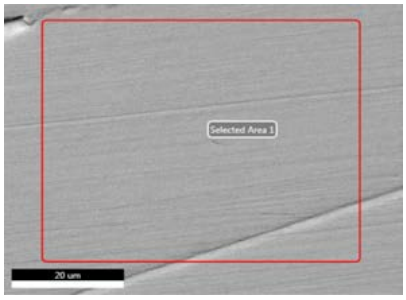

Element	Weight %	Atomic %	Error %
SnL	38.4	22.4	2.2
MnK	56.2	70.9	2.5
FeK	5.4	6.8	5.7

(c) $Mn_{2.5}Fe_{0.5}Sn$

Element	Weight %	Atomic %	Error %
SnL	38.8	22.8	2.2
MnK	52.8	66.8	2.5
FeK	8.4	10.5	4.4

Figure 4.3: The FESEM images and corresponding EDS results for $Mn_{3-x}Fe_xSn$ samples.

4.3 Magnetic properties of samples

The magnetic measurements are performed both on the single crystal and polycrystalline samples. Hereafter, the measurements on the single crystalline samples are mainly focused.

Figure 4.4 displays the $M(T)$ data for three single crystalline samples measured in the ZFC and FC modes at a field of 1000 Oe. The left column in Fig. 4.4 shows the measured data when the magnetic field is applied parallel to the c-axis of the hexagonal unit cell, while the data for $H \perp c$ are plotted in the right column. Let

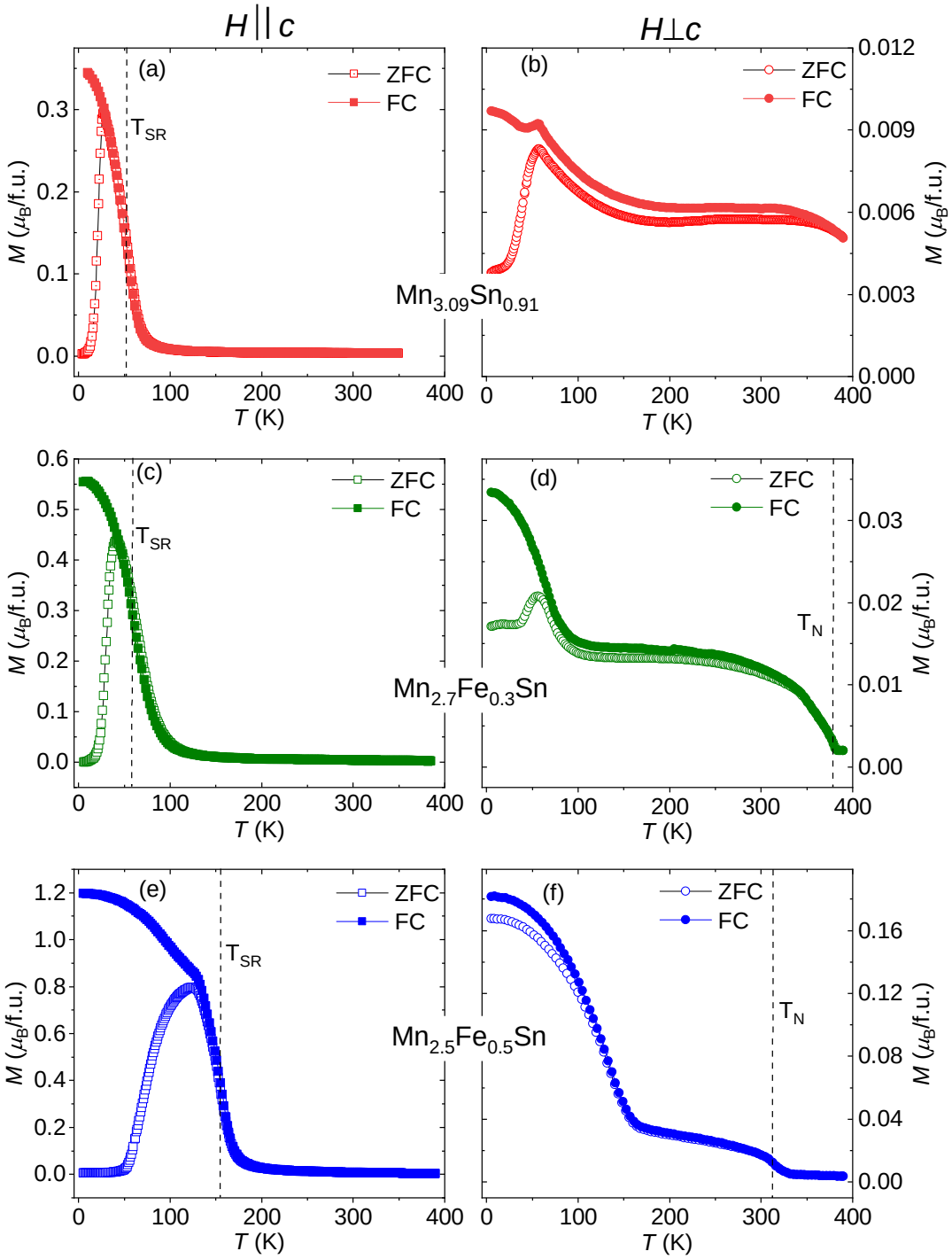

Figure 4.4: Temperature dependent ZFC and FC $M(T)$ curves for (a-b) $Mn_{3.09}Sn_{0.91}$, (c-d) $Mn_{2.7}Fe_{0.3}Sn$ and (e-f) $Mn_{2.5}Fe_{0.5}Sn$ samples measured in two different orientations. The left column shows measurements for fields applied along the c-axis, and the right column shows data for fields perpendicular to c-axis.

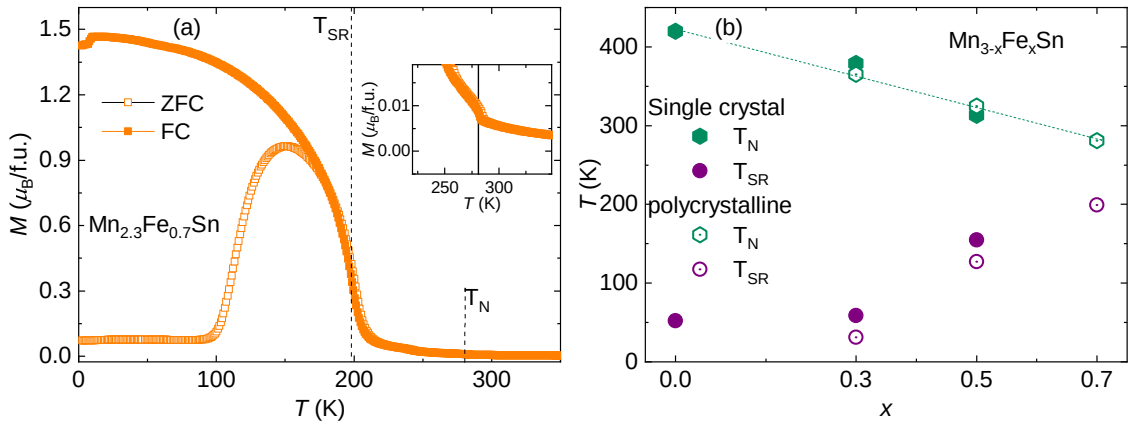

Figure 4.5: (a) ZFC and FC $M(T)$ plots for polycrystalline $Mn_{2.3}Fe_{0.7}Sn$ sample. The inset shows zoomed in view of the Neel temperature. (b) Fe doping dependence of spin reorientation transition temperature T_{SR} and magnetic ordering temperature T_N.

us go through these plots individually. Figure 4.4 (a) and (b) show the $M(T)$ data for the $Mn_{3.09}Sn_{0p91}$ sample. The data for the field applied perpendicular to the c-axis exhibit a very small magnetic moment in the whole temperature range. For the $H \perp c$, the data above 100 K remains essentially constant and featureless. No signature of magnetic ordering temperature is visible in the measured data, as the Neel temperature T_N for the parent Mn_3Sn is reported to be above 400 K.[83]

For the $M(T)$ measurements performed for $H \parallel c$, it is observed that the magnetization stays at a small value above 100 K. The magnetic moments in the iT-AFM structure of the Mn_3Sn sample lie in the basal plane of the hexagonal lattice structure. Hence, a vanishing magnetic moment is expected along the c-axis, which matches well with the observation of negligible magnetic moment above 100 K. However, when the temperature is decreased below 100 K, the magnetization value rises dramatically. A significant bifurcation is also visible in the ZFC and FC $M(T)$ curves at low temperatures. The massive bifurcation points toward the presence of high magnetic anisotropy in the sample. These results indicate that the samples undergo a spin reorientation transition below 100 K. The spin reorientation temperature T_{SR} is obtained from the first derivative of the FC curve and is marked by a dotted line in the plots.

Now moving on to the Fe (higher electron) doped samples, Fig. 4.4 (c-d) and (e-f) shows the $M(T)$ plots for $Mn_{2.7}Fe_{0.3}Sn$ and $Mn_{2.5}Fe_{0.5}Sn$ samples, respectively. For these samples, the data for $H \perp c$ show a clear signature of the Neel temperature. The ordering temperature T_N is marked in respective plots. The T_N decreases with increasing electron doping. Moreover, the $H \parallel c$ measurements show a similar nature of magnetization variation to that of the $Mn_{3.09}Sn_{0p91}$ sample, with an increase in the spin reorientation temperature T_{SR}. The magnetic moment and the extent of bifurcation between the ZFC and FC $M(T)$ curves also increases. The single crystal samples could only be synthesized up to Fe doping of 0.5. However, polycrystalline sample of $Mn_{2.3}Fe_{0.7}Sn$ is successfully obtained. Figure 4.5 (a) shows the $M(T)$ for the polycrystalline $Mn_{2.3}Fe_{0.7}Sn$ sample, which shows both the spin reorientation transition and the ordering temperature T_N. The T_{SR} increases further for the $Mn_{2.3}Fe_{0.7}Sn$ sample while the T_N decreases further. These results are summarized in Fig. 4.5 (b), where the variation of T_{SR} and T_N with Fe doping is plotted for both the single crystals as well as the polycrystalline samples. For the $Mn_{2.3}Fe_{0.7}Sn$ samples, T_{SR} is approximately 200 K and nearly covers the entire magnetic ordered phase.

The $M(H)$ measurements for the three samples are shown in Fig. 4.6. Like the $M(T)$ measurements, $M(H)$ data are also taken by applying fields parallel and perpendicular to the c-axis. The $M(H)$ loop for the $Mn_{3.09}Sn_{0p91}$ sample with field applied perpendicular to the c-axis shows a linear behavior, with a small hysteretic loop at low magnetic fields [Fig. 4.6 (b)]. The behavior of the $M(H)$ loop stays nearly the same at 5 K. The nature of the $M(H)$ loops for H perpendicular to c matches well with that obtained for the iT-AFM spin structure.

For $H \parallel c$ [Fig. 4.6 (a)], the room temperature data shows a perfect linear $M(H)$ loop, as the magnetic moments in the iT-AFM state lye in the basal plane. Thus, the application of a magnetic field only tilts the Mn moments along the c-axis by a minuscule value and results in the linear nature of the loop. Upon decreasing the temperature, slope of the linear $M(H)$ loop keeps on increasing. At 75 K, a slight ferromagnetic hysteresis character starts to appear. Further reduction in

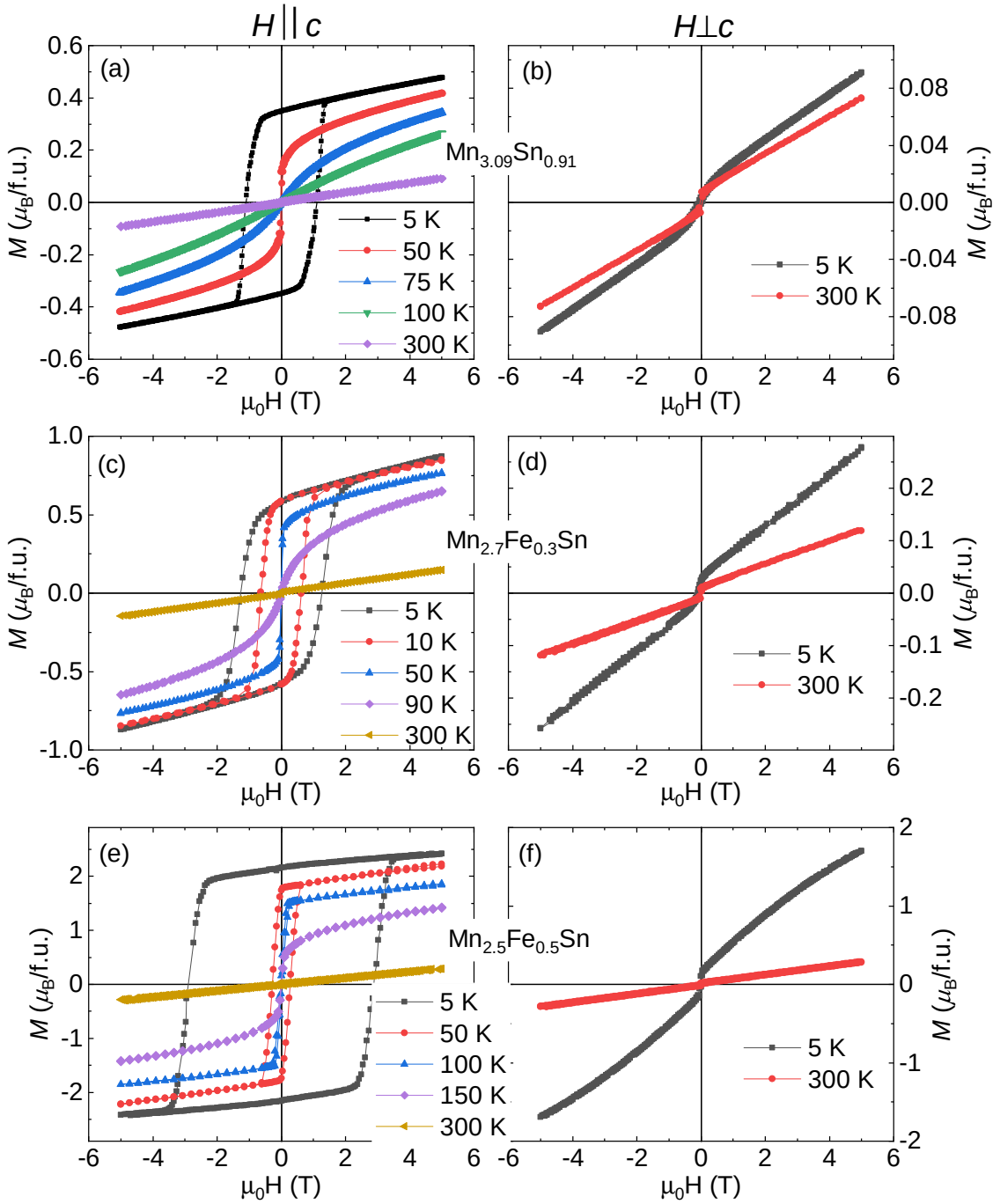

Figure 4.6: Field dependent isothermal $M(H)$ loops for (a-b) $Mn_{3.05}Sn_{0.95}$, (c-d) $Mn_{2.3}Fe_{0.7}Sn$ and (e-f) $Mn_{2.5}Fe_{0.5}Sn$ samples at various temperatures. The left column shows measurements for fields applied parallel to c-axis, and right column shows data for $H \perp c$-axis.

temperature leads to a ferromagnetic-like loop at 50 K. At 5 K, the sample shows a large hysteresis loop with a large coercive field. As is evident from the $M(H)$ plots, the zero filed extrapolated moment, as well as the magnetic moment at 5 T, keeps increasing with decreasing temperature. These results suggest the presence of a c-axis oriented long-range ferromagnetic order. It is important to mention here that the non-linear nature of the $M(H)$ loop only starts appearing at the spin reorientation transition shown in the $M(T)$ measurements.

For the $Mn_{2.7}Fe_{0.3}Sn$ sample [Fig. 4.6 (c-d)], the in-plane $M(H)$ loop exhibits a linear behavior with small hysteresis at low as well as high temperatures. The room temperature $M(H)$ loop for $H \parallel c$ shows a linear behavior, while the reduction in temperature imparts a hysteretic nature below the T_{SR}. The magnetic moment along the c-axis also increases for $Mn_{2.7}Fe_{0.3}Sn$ in comparison to that of $Mn_{3.09}Sn_{0p91}$. The $Mn_{2.5}Fe_{0.5}Sn$ sample follows the same trend [Fig. 4.6 (e-f)]. The coercive field value reaches a very large value for the $H \parallel c$ data, and the sample exhibits a magnetic moment of nearly $2\mu_B$ $f.u.$. The size of the moment for in-plane measurements also increases significantly.

The magnetic measurements can be summarized as follows

1. The samples undergo a spin reorientation transition from in-plane to along the c-axis at T_{SR}.

2. The Samples exhibit a large coercive field and magnetic moment below the T_{SR}.

3. The in-plane characteristic of the magnetic moments stays nearly similar for all samples

4. The out-of-plane and the in-plane magnetic moments increase with increasing Fe doping.

Now let us try to comprehend these results. Based on the magnetic data, the aim is now to build a model spin structure for the ground magnetic state below the

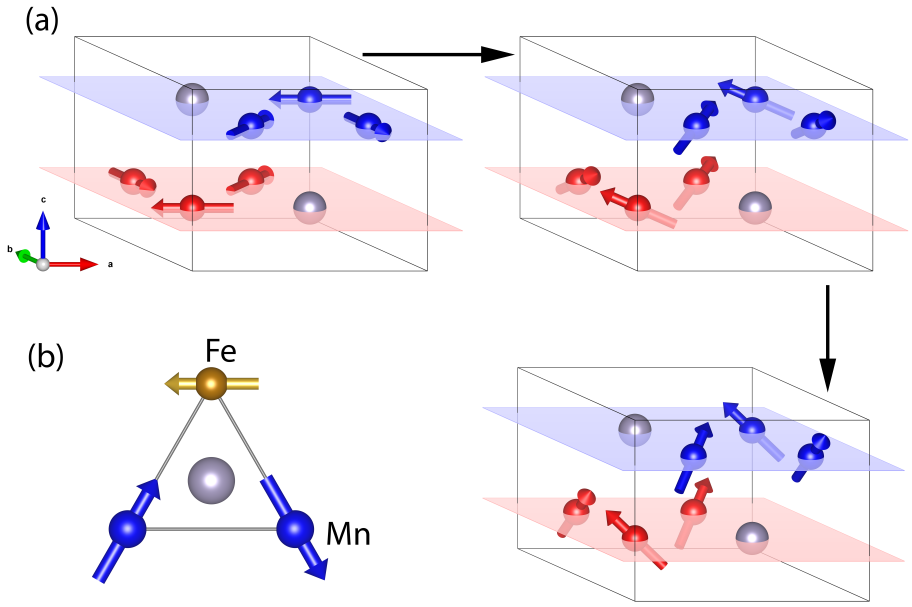

Figure 4.7: (a) Schematic of the proposed model of spin reorientation transition for the hexagonal Mn_3Sn. (b) The triangular lattice site with two large Mn and one smaller Fe moment.

spin reorientation transition. Subsequently, the proposed model will be validated by using further theoretical and experimental studies.

4.4 'True' magnetic ground state of Mn_3Sn

4.4.1 Proposed magnetic ground state

The room temperature iT-AFM structure of Mn_3Sn is shown in Fig. 4.7 (a). All the moments lie in the *ab*-plane of the hexagonal unit cell. In the 120° spin structure of the iT-AFM structure, the total magnetic moment of a triangle perfectly cancels each other out. The magnetic measurements indicate that a spontaneous magnetic moment is present along the *c*-axis below T_{SR}. This observation can be accounted for by a simple canting of all the spins by an angle ϕ along the *c*-axis. Figure 4.7 (a) shows a schematic of such a canting of spins. The in-plane component of the magnetic moment of such a canted state continues stabilizing the iT-AFM state, and

thus the in-plane magnetic moment remains zero. The magnetic properties observed for the $Mn_{3.09}Sn_{0p91}$ sample are well accounted for by this model.

Furthermore, an increase in the out-of-plane canting angle may cause the rise of the magnetic moment along the *c*-axis with Fe doping. The increased in-plane magnetic moment with Fe doping is probably a consequence of a smaller magnetic moment on the Fe atoms compared to that of Mn. A schematic of such a situation is shown in Fig. 4.7 (b), where the small magnetic moment of Fe ion leads to an uncompensated magnetic moment perpendicular to *c*.

4.4.2 Neutron diffraction study of ground state

Neutron diffraction (ND) measurement is carried out to confirm the presence of the purposed magnetic ground state at low temperatures. For this purpose, the sample with composition $Mn_{2.5}Fe_{0.5}Sn$ is utilized. The ND data for $Mn_{2.5}Fe_{0.5}Sn$ are collected at different temperatures including that of above the T_N. Before analyzing the neutron diffraction data, the effect of the out-of-plane canting on the neutron pattern is simulated, as plotted in Fig. 4.8 (a). The data are simulated for a wavelength of 1.24430 . The simulated data reveals an appreciable intensity redistribution in the neutron data for (200) and (201) peaks for different out-of-plane canting angel.

The (201) and (200) peaks for the recorded data are shown in Fig. 4.8 (b-c) at different temperatures. The neutron diffraction data are collected for neutron wavelength $\lambda = 2.43955$. It can be seen that the intensity of both the peaks practically remains constant from room temperature to 150 K. Below 150 K, the peak intensity starts to rise sharply. Finally, at the lowest temperatures, the peak intensity enhances significantly for both the reflections compared to the data above 150 K. The increase in peak intensity is even more evident in Fig. 4.8 (d), where the area of both peaks is plotted as a function of temperature. The area is assessed using a Gaussian fit of the peaks. It is seen that the area of both peaks begins to rise below 150 K and keeps rising all the way down to very low temperatures. This

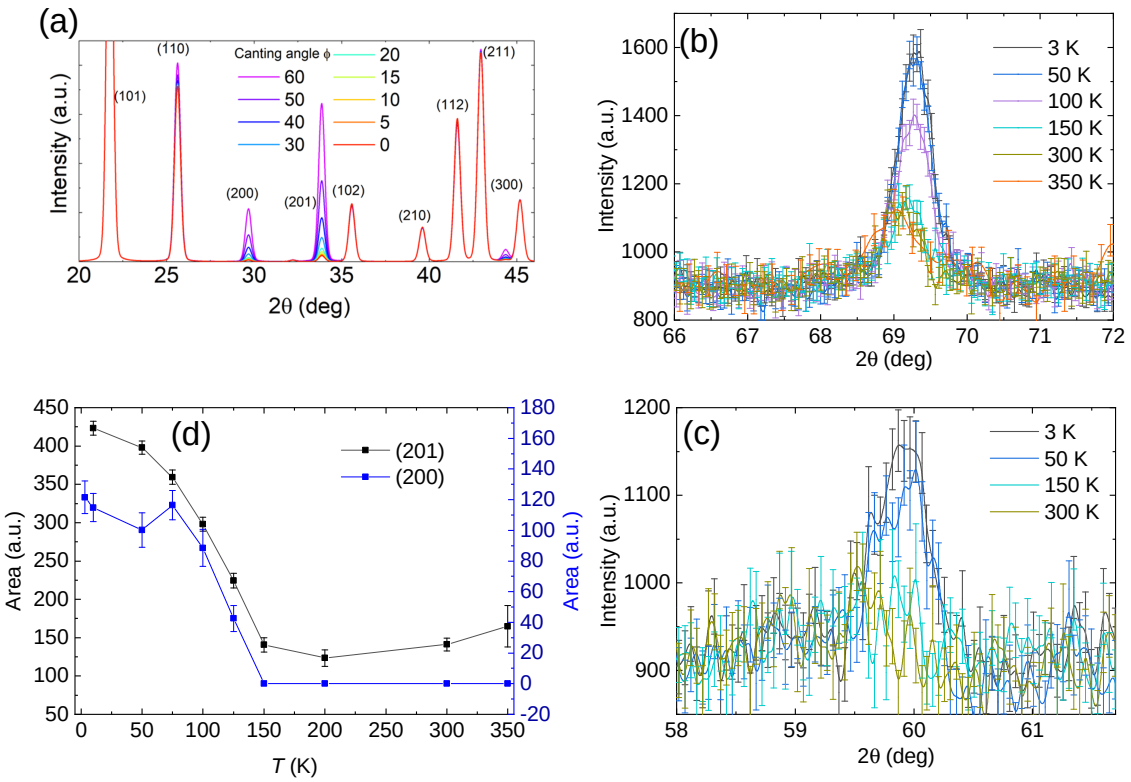

Figure 4.8: (a) Simulated neutron diffraction data for different out-of-plane canting angles. ND data at different temperatures for (b) (201) and (c) (200) reflections. (d) Temperature dependent area of the (201) and (200) peaks as evaluated by a Gaussian fitting of the peaks.

finding follows well the trend observed in simulated data that a canting of spins along the c-axis enhances the peak intensity of (200) and (201) reflections.

The $Mn_{2.5}Fe_{0.5}Sn$ sample displays a magnetic ordering temperature of 320 K. The ND data taken at 350 K is shown in Fig. 4.9 (c). As the sample shows no magnetic ordering at 350 K, the data at 350 K is used to refine the structural details of the sample. Once the 350 K data is refined, the refinement parameters are fixed. Subsequently, the magnetic phase is added and refined using these parameters to fit the data at low temperatures. From the structural part, only the lattice parameters are refined for the lower temperatures. The Rietveld refinement of the 350 K data shows a good fit with the hexagonal unit cell of the sample. The refined lattice parameters are $a = 5.6216$ and $c = 4.4944$. The Wyckoff parameter x for the $6h$(x,2x,0.25) ionic position of the Mn atom is 0.1585.

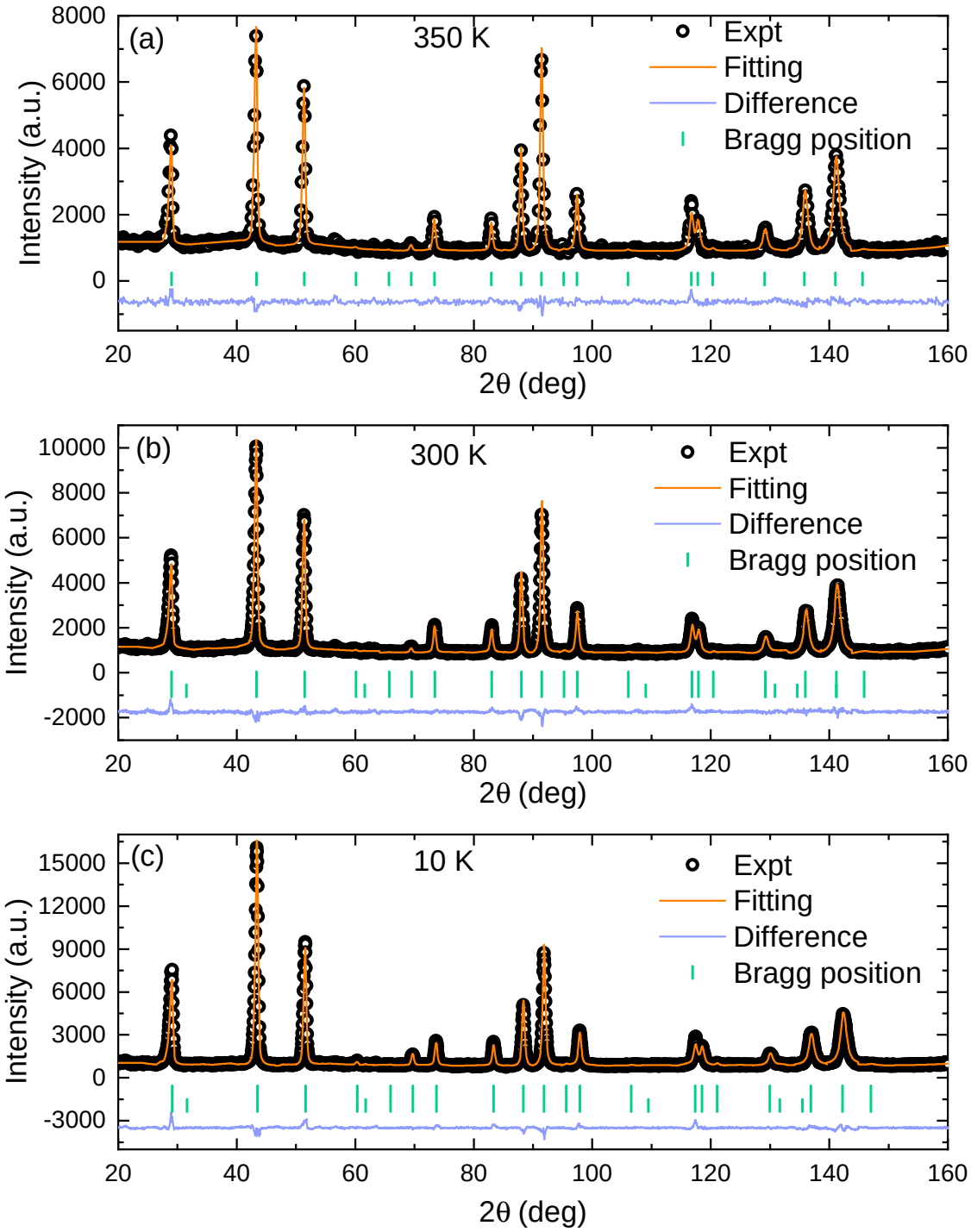

Figure 4.9: Neutron diffraction data with Rietveld refinement at different temperatures for $Mn_{2.5}Fe_{0.5}Sn$ sample. (a) The 350 K data with only structural fit. (b) The ND data at 300 K fitting with iT-AFM structure. (c) The fitting of 10 K data with canted iT-AFM structure.

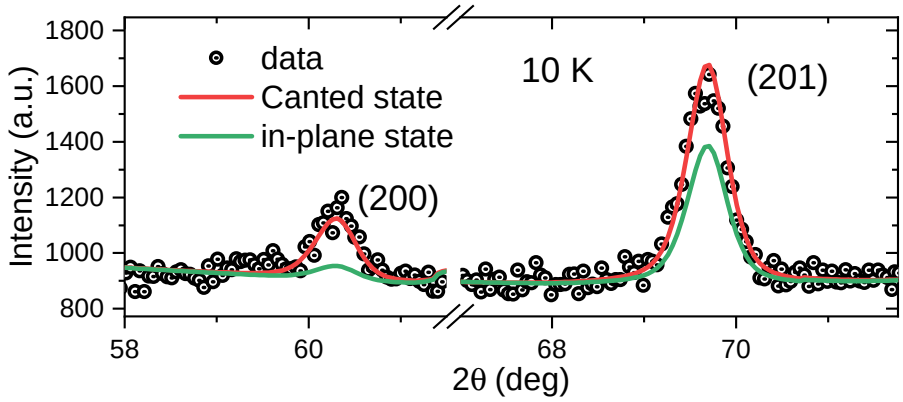

Figure 4.10: Fitting of the 10 K ND data with and without canting. 2θ range for the (201) and (200) peaks is shown.

The magnetic ground state for the sample up to 150 K can be nicely fitted with the 120° iT-AFM structure. Figure 4.9 (b) shows the plots for room temperature ND data. The data is well fitted with the iT-AFM structure. Below 150 K, the data is only best fitted by including an out-of-plane canting of the magnetic spins. The data at 10 K, along with Rietveld fitting, is shown in Fig. 4.9 (c). The canting angle from the refinement comes out to be approximately 15°. Figure 4.10 shows a comparison of the data fitted with and without canting for the (200) and (201) peaks at 10 K, which establishes the better inclusion of data with a canted state. Thus the neutron diffraction measurements confirms the presence of the canted state as the ground state.

Discussion on 'True' magnetic ground state: Now that the magnetic structure below T_{SR} is resolved, let us discuss in details about the consequence of the present magnetic ground state. Due to the canted nature of the magnetic structure, a non-coplanarity is induced. As discussed in chapters 1, a non-coplanar magnetic state can contribute to an additional component to the Hall voltage. It is known that Mn_3Sn exhibits a large AHE due to the cluster octupole order of the non-collinear magnetic ground state at room temperatures (chapter 1). For the canted ground state, the in-plane component of the magnetic state remains the same. This implies that one should be able to measure the octupole order-induced Hall signal in the

samples at all temperatures down to the lowest one. Below the T_{SR}, the spins cant along the c-axis and generate a state with finite scalar spin chirality (SSC). The scalar spin chirality is a measure of the non-coplanar nature of the spin structure and is calculated as $S_i.(S_j \times S_k)$. The SSC of a triangular unit of kagome lattice is plotted in Fig. 4.11 (b) as a function of canting angle ϕ. It is clear that the SSC increases with canting of the spins and reaches a maximum at 35°. Above this value, the SSC again reaches zero at 90° (ferromagnetic order). Thus the sample could show a finite Hall signal due to this SSC, which can exist along with the Hall signal generated by the octupole order. To confirm these deductions, the transport measurements are performed on three samples as discussed below.

4.5 Transport properties of canted ground state

A schematic of the magnetic state below and above the T_{SR} is shown in Fig. 4.11 (a). The fictitious magnetic field due to the octupole order lies in the plane of the kagome lattice. The octupole order domains can be aligned by applying a magnetic field in the kagome plane. Thus, this octupole order induced Hall signal can be detected in the ρ_{xz} component of Hall resistivity, where the field is applied along the y direction. On the other hand, the ferromagnetic component domains are aligned by the application of a magnetic field along the c-axis. Hence the Hall signal due to this component can show up in the ρ_{xy} component. A schematic of the ρ_{xy} and ρ_{xz} measurement is shown in Fig. 4.11 (d). The Hall bar are prepared from the single crystals with x as $[2\bar{1}\bar{1}0]$ and y as $[01\bar{1}0]$ direction. Figure (c) shows the chosen direction in reference to a hexagonal structure. The z direction corresponds to the c-axis of the unit cell.

The octupole order induced ρ_{xz} component of the Hall signal is plotted in Fig. 4.12 for the three samples. The $Mn_{3.09}Sn_{0p91}$ sample shows a large Hall signal at room temperature, similar to that is observed earlier. The Hall signal shows a robust nature upon reduction in temperature and is observed up to 5 K temperature, with a maximum value at 200 K. The conductivity plots are also shown in Fig. 4.12 (b).

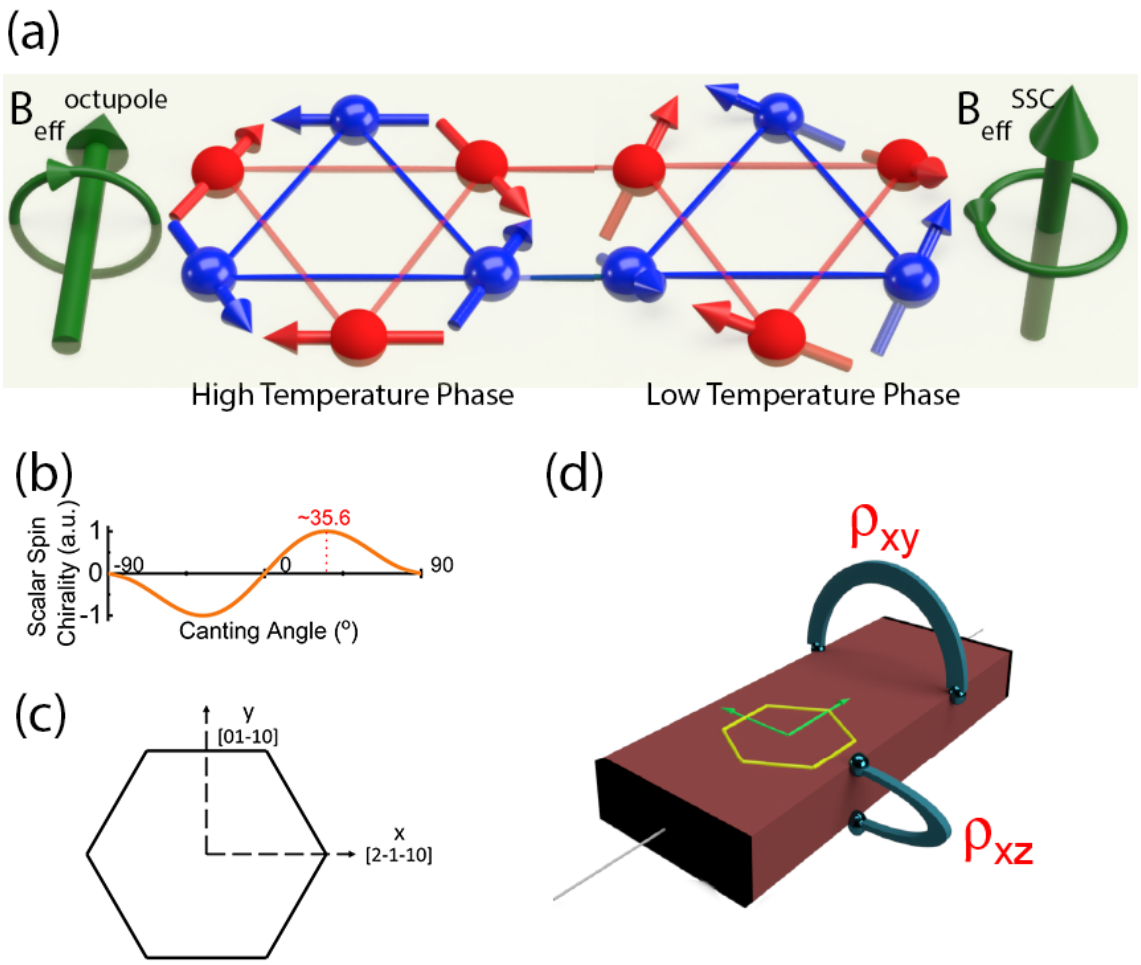

Figure 4.11: (a) Schematic of the high-temperature, in-plane iT-AFM state (left) and the canted low-temperature magnetic state (right). The green arrows represent the direction of the fictitious magnetic field generated by octupole order (left) and the non-coplanar canted state (right). (b) The SSC on a triangular unit as a function of out-of-plane canting angle. (c) The hexagonal structure with marked directions that are chosen as x and y for transport measurements. (d) 3D schematic of a rectangular shaped Hall bar showing the ρ_{xy} and ρ_{xz} measurement connections.

The conductivity values of the samples also match well with the earlier reported ones. Both the Fe doped samples exhibit a robust ρ_{xz} signal down to 5 K. The Hall resistivity value decreases with larger Fe doping. Hall conductivity also follows a similar trend, where it reduces to a very small value for the $Mn_{2.5}Fe_{0.5}Sn$ sample. The presence of the ρ_{xz} signal for the three samples in the whole temprature range implies a stable octupole order in the electron doped samples.

Next, the ρ_{xy} measurements are carried out on the three samples, as shown in Fig.

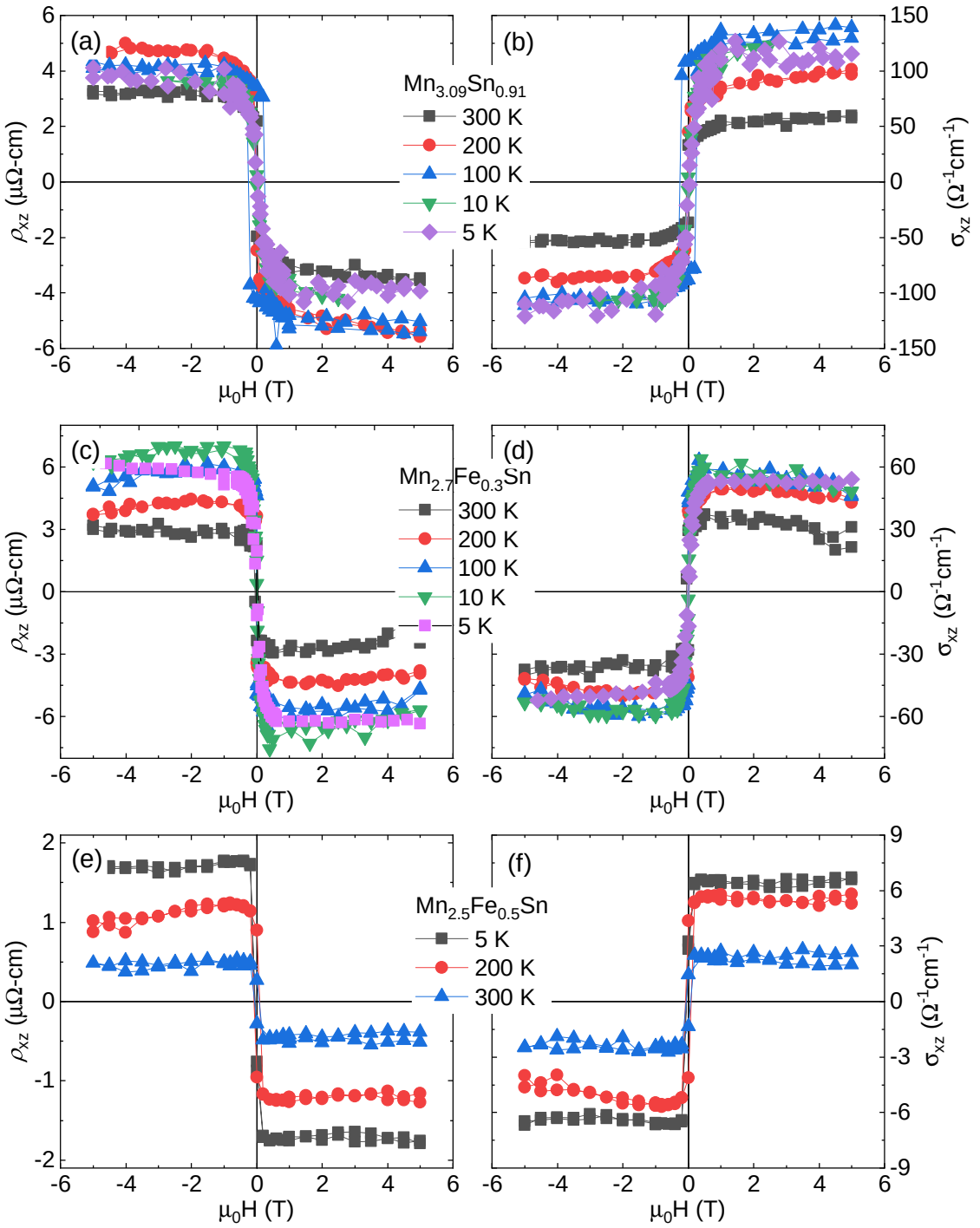

Figure 4.12: Field dependent ρ_{xz} component of Hall resistivity (left column) and Hall conductivity (right column) for (a-b) $Mn_{3.05}Sn_{0.95}$, (c-d) $Mn_{2.3}Fe_{0.7}Sn$ and (e-f) $Mn_{2.5}Fe_{0.5}Sn$ samples at different temperatures.

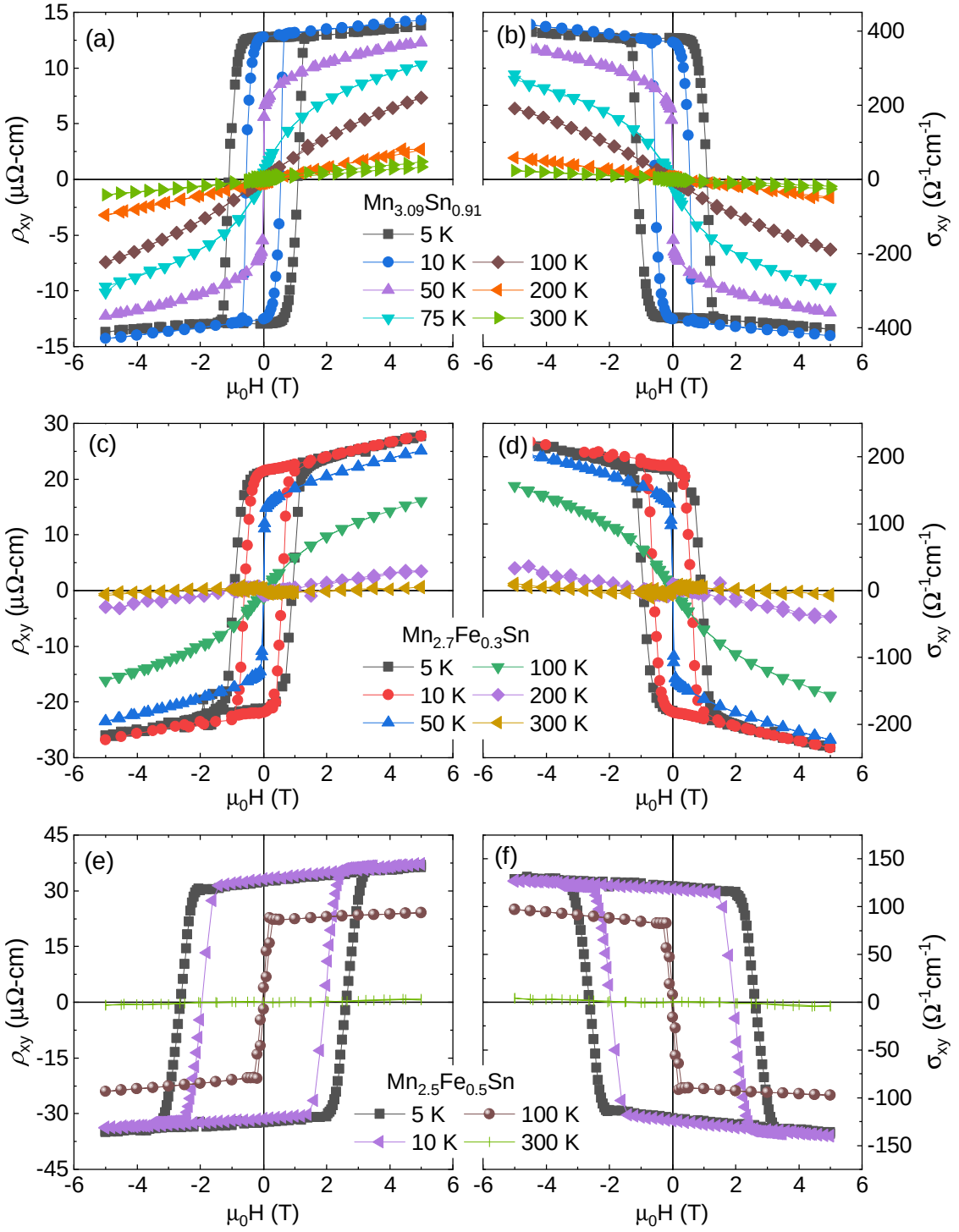

Figure 4.13: Field dependent ρ_{xy} component of Hall resistivity (left column) and Hall conductivity (right column) for (a-b) $Mn_{3.05}Sn_{0.95}$, (c-d) $Mn_{2.3}Fe_{0.7}Sn$ and (e-f) $Mn_{2.5}Fe_{0.5}Sn$ samples at different temperatures.

4.13. The $Mn_{3.09}Sn_{0p91}$ sample does not show any ρ_{xy} signal at room temperature, which is expected for the iT-AFM state above T_{SR}. The Hall signal above the T_{SR} shows a linear trend, similar to $M(H)$ measurements. Below T_{SR}, a huge ρ_{xy} signal starts to arise in the sample. It reaches a very large value of 13 $\mu\Omega$-cm at 5 K. The Hall conductivity plots shown in Fig. 4.13 (b) exhibits a very large. This 'new' ρ_{xy} signal is even larger than the earlier observed Hall signal due to octupole order. The Fe doped samples also show a similar nature for the ρ_{xy} plots, where a finite Hall signal is seen below T_{SR}. The ρ_{xy} value increases for higher Fe doping and reaches a maximum of 35 $\mu\Omega$-cm for the $Mn_{2.5}Fe_{0.5}Sn$ sample. These values correspond to nearly the highest values for a metallic sample. However, the Hall conductivity v shows a reduction in magnitude for higher Fe-doped samples. Although one would expect larger values of conductivity for the Fe-doped samples with enhanced SSC, the exact value of SSC induced Hall signal depends on a multitude of variables like band filling.[84]

Nevertheless, the results presented in this section reveal the presence of a 'new' SSC induced Hall signal below T_{SR} in the Mn_3Sn series of samples. The values obtained here are specifically huge for the systems exhibiting an SSC phenomenon-induced Hall signal. Moreover, the Hall signal reported here is a spontaneous property of the magnetic ground state.

4.5.1 Confirmation of the scalar spin chirality mechanism

The large anomalous Hall signal (ρ_{xy}) reported in the last section originates from the non-coplanar magnetic phase of $Mn_{3-x}Fe_xSn$ samples. However, the SSC-based mechanism is not the only candidate which can generate this Hall signal. Topological features in the band structure of various materials have been extensively studied regarding the presence of large AHE. The topological nature of band structure leads to an intrinsic contribution to the Hall signal. Thus, let us first examine the extent of intrinsic and extrinsic contributions to the ρ_{xy} signal.

The intrinsic and extrinsic contributions to the Hall signal can be extracted

using the scaling relations, which are discussed in section 1.3.3. A plot of $\log(\rho_{xy})$ vs. $\log(\rho_{xx})$ should yield a slope of 2 for the intrinsic nature of AHE, while a slope of 1 is expected when the contribution is extrinsic. The $\log(\rho_{xy})$ vs $\log(\rho_{xx})$ plots for $Mn_{2.7}Fe_{0.3}Sn$ and $Mn_{2.5}Fe_{0.5}Sn$ samples are shown in Fig. 4.14 (a-b). An anlysis for the $Mn_{3.09}Sn_{0p91}$ sample could not be performed due to the Kondo effect seen for that samples at low temperatures. A linear fit of data below $T_S R$ for $Mn_{2.7}Fe_{0.3}Sn$ and $Mn_{2.5}Fe_{0.5}Sn$ samples reveals unusually large values of slope for both the samples. These values are unacceptable for the AHE scaling relations. To improve the scaling, the presence of finite SSC of the ground state is incorporated into the data. If the source of the present AHE signal is the finite SSC of the magnetic ground state, then a plot of $\log(\rho_{xy}/\text{SSC})$ instead of $\log(\rho_{xy})$ should help the fitting. The division by SSC is performed because with reducing temperature, the magnetic moments slowly start to cant along the c-axis before reaching a maximum value at low temperature. The slow canting is evident from the $M(T)$ and $M(H)$ measurements. The SSC, which is the source of the Hall signal, and depends on the canting angle ϕ, also changes with temeprature. A division of the Hall signal with SSC gives us Hall resistivity per unit SSC value, which should not change with temperature. The SSC at different temperatures is calculated from the magnetization measurements and a new plot of $\log(\rho_{xy}/\text{SSC}$ vs $\log(\rho_{xx})$ is shown in Fig. 4.14 (c-d). A line corresponding to a slope of 2 is also plotted in the same figures. It can be seen that the new data fits nicely with a line of slope 2, confirming that the AHE is of intrinsic nature. Moreover, the fitting could only be achieved after normalizing ρ_{xy} by SSC, which indicates that the Hall signal is driven by the finite SSC of the magnetic ground state.

To further confirm the SSC-induced mechanism of the ρ_{xy} signal, a fitting of the anomalous Hall signal with the magnetization of the sample is performed. The Hall resistivity for intrinsic contribution can be written as

$$\rho_{xy} = R_0 H + b\rho_{xx}^2 M, \tag{4.1}$$

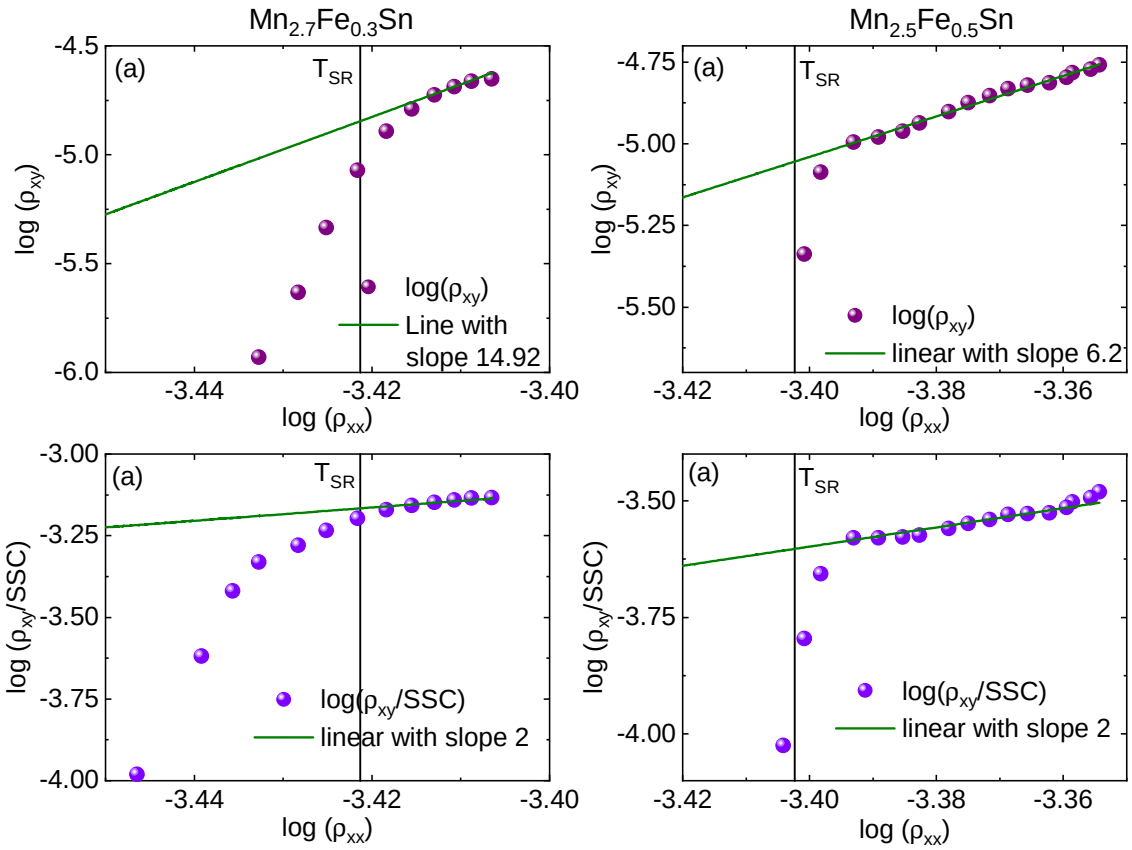

Figure 4.14: (a-b) AHE scaling plots for $Mn_{2.7}Fe_{0.3}Sn$ and $Mn_{2.5}Fe_{0.5}Sn$ samples. The scattered data points represent the experimental $\log(\rho_{xy})$ values and the line correspond to a linear fit of the data. The vertical grid line mark the spin reorientation transition temperature. (c-d) The $\log(\rho_{xy}/\mathrm{SSC})$ plots for the two samples and a line corresponding to slope of 2.

where R_0 is the normal Hall coefficient, b is a scaling factor, H is the applied external magnetic field, and M is the magnetization. If the observed Hall signal originates due to the net magnetization of the sample, an exact fit of the observed Hall signal with the above equation is expected. To evaluate constants R_0 and b, let us rewrite Eq. 4.2 as

$$\frac{\rho_{xy}}{H} = R_0 + \frac{b\rho_{xx}^2 M}{H}. \tag{4.2}$$

Thus the slope and intercept of a linear fit of $\frac{\rho_{xy}}{H}$ vs. $\frac{b\rho_{xx}^2 M}{H}$ plot gives the value of b and R_0. This fitting is carried out at high fields in the range of 2-5 T.

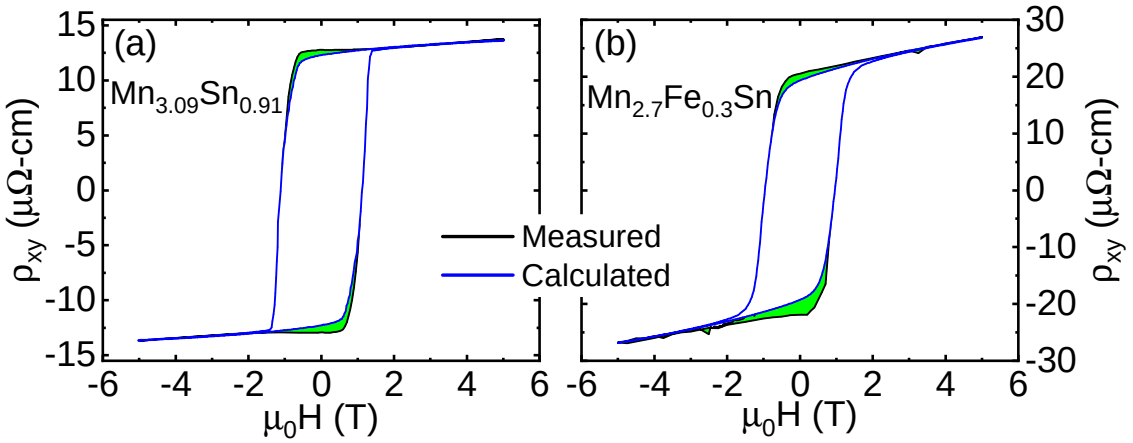

Figure 4.15: (a-b) The measured and calculated Hall resistivity for (a) $Mn_{3.09}Sn_{0.91}$ and (b) $Mn_{2.7}Fe_{0.3}Sn$ sample at 5 K. The shaded region highlights the mismatch between two curves.

The calculated and measured Hall resistivity data are plotted in Fig. 4.15 for (a) $Mn_{3.09}Sn_{0.91}$ and (b) $Mn_{2.7}Fe_{0.3}Sn$ sample at 5 K. It can be seen that the fitting is good for the high field range from where the parameters are extracted. However, a significant mismatch is found in the measured and calculated Hall data in the low field range. Now, if the source of the Hall signal is the magnetization of the sample, then the calculated Hall and measured signal should match each other. However, the SSC only depends on the out-of-plane canting angle of the magnetic moment. Thus, the observed mismatch could result from a dissimilar change in the magnetization and the magnitude of SSC with application of magnetic field. These measurements show that the observed Hall signal mostly originates from the SSC mechanism rather than the magnetization of the sample.

4.6 Dual magnetic order

The presence of two different Hall signals in the non-coplanar phase of the Mn-Fe-Sn system is shown in the previous section. Thus, the Hall resistivity of samples are highly anisotropic in nature. Many samples reported in the literature show a large anisotropy in the Hall signal. The room temperature phase of Mn_3Sn and Mn_3Ge is

among them. However, the anisotropic Hall signal of the non-coplanar state differs from those observed in earlier reports in a crucial way. For nearly all the samples studied in the literature, there always exists a single source of Hall signal. This statement implies that whenever an anisotropy is observed in the Hall signal, it mostly originates from the change in symmetries when the magnetic field is applied in a different direction of an anisotropic crystal. However, the net magnetization is always the source of the Hall signal, generating dissimilar Hall signals in a different directions. For the results presented here, the Hall signal arises from two different sources: octupole order and SSC of the dipole moments. Thus, the non-coplanar magnetic ground state of these samples exhibits a phenomenon of dual magnetic ordering in the system.

A fundamental question now arises regarding the dual-ordered magnetic state of the current samples. Are these two orders coupled or independent? To explore this, the Hall setup is prepared in such a way as to measure both the Hall signals simultaneously. A picture of the sample with contact connections is shown in Fig. 4.16, as well as the schematic in Fig. 4.11 (d). The setup is mounted on a rotator to facilitate the application of magnetic fields in different directions of the $y-z$ plane. The two extreme orientations are shown schematically in Fig. 4.17. In the first case, the magnetic field is applied along the c-axis, which aligns the SSC domains, leading to a field reversible observation of the SSC-induced Hall signal. In the other orthogonal orientation, the field aligns the octupole order domains, and the ρ_{xz} component can be reversed with the application of a magnetic field. As the connections are made for both the Hall signals, a simultaneous measurement of ρ_{xy} and ρ_{xz} is possible.

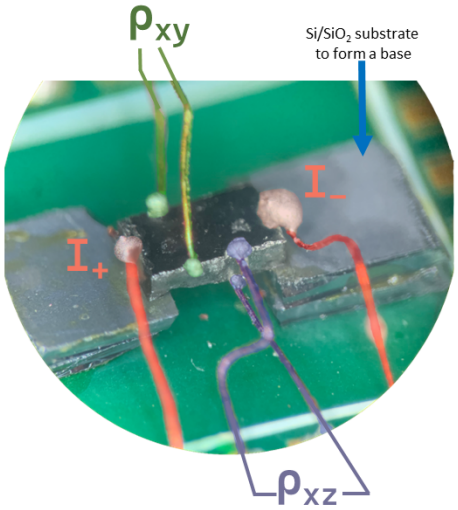

Figure 4.16: Picture of the Hall connection made to measure ρ_{xy} and ρ_{xz} component simultaneously.

For the measurement, first, the SSC domains are aligned by applying a saturating

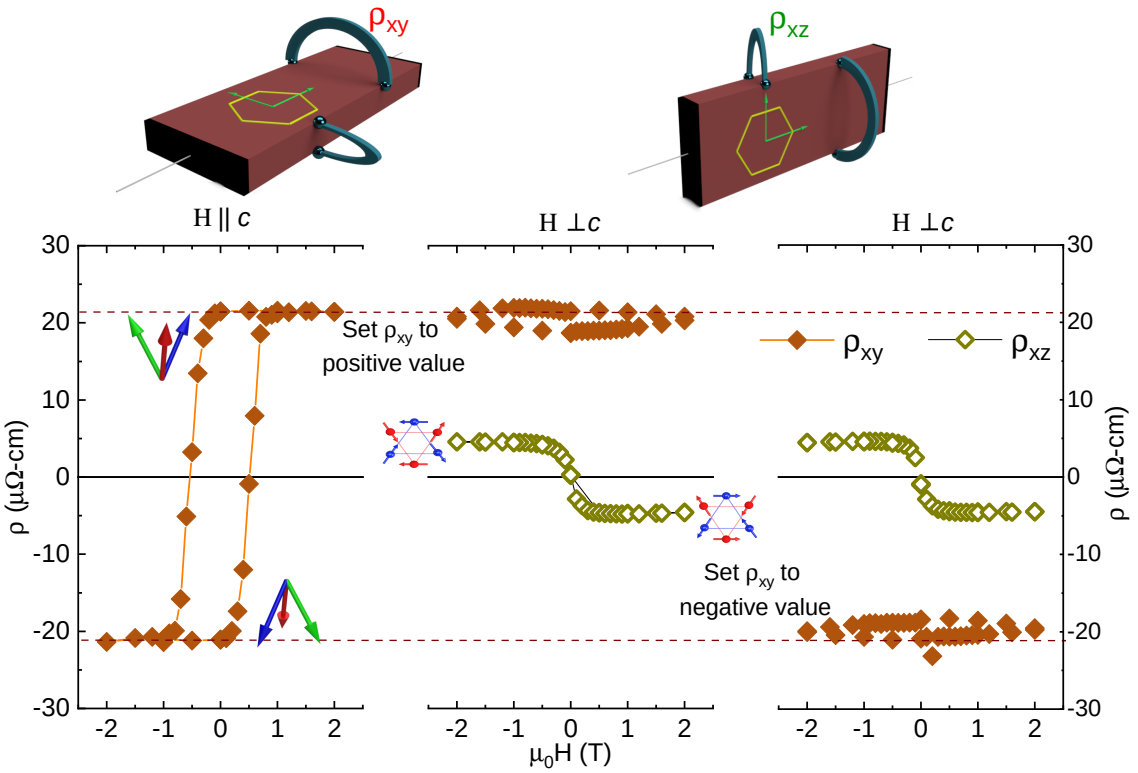

Figure 4.17: The Hall measurements data to probe characteristics of dual order are plotted. Brown and green data corresponds to the ρ_{xy} and ρ_{xz} signal respectively. A schematic at top is shows the measurement protocol. See text for more details.

field along the c-axis. The SSC-induced Hall signal is shown in the left plot of Fig. 4.17. The applied field is then made to zero. As the SSC domains show a sizable coercive field, the SSC domains remain aligned even after reducing the magnetic field to zero. In this remnant state of the SSC domains, the sample setup is rotated, and the field is now applied in the plane of the hexagonal structure. The in-plane magnetic field can align the octupole domains, and the ρ_{xz} component of Hall resistivity can be measured. The ρ_{xz} signal is shown in the middle part of the Fig. 4.17. As the connection for both ρ_{xy} and ρ_{xz} are made, the setup allows us to measure both components. It can be seen that with a sweep of the in-plane magnetic field, the octupole order induced Hall changes sign with the reversal of the magnetic field. In contrast, the saturated SSC-induced Hall signal stays at the positive value. Afterward, the SSC signal is saturated by a negative magnetic field. For the negative saturation, it can be seen that the octupole signal is reversed while

the SSC signal stays at a negative saturation value (right part of the figure). This implies that the octupole and SSC domains can be easily switched independent of each other. Thus, the present system possesses a four-fold degenerate domain state rather than the normal two-fold degenerate state found in magnetic systems.

4.7 Theoretical study of magnetic ground state

4.7.1 Ground state from $ab-initio$ studies

The non-collinear version of the VASP code is used in conjunction with the constrained magnetic calculations to probe the minimum energy ground state for different samples. The calculation details can be found in chapter 2. The total energy of the Mn_3Sn system is calculated for different canting angles ϕ using the constrained moment calculations. The magnetic structure of the Mn_3Sn unit cell is initially fixed as the iT-AFM state, and the DFT calculated energy of this spin configuration is obtained. Afterward, all the magnetic moments in the unit are canted along the c-axis by different magnitudes of out-of-plane canting angles ϕ. The total energy of the system for different canting angles is then recorded for different canting angles. Following the same procedure, a series of calculations are performed for the $Mn_{3-x}Fe_xSn$ series of samples with x ranging from 0 to 3. The Fe doping is incorporated using the virtual crystal approximation (VCA) scheme available in the VASP code. For simplicity, the ideal kagome lattice structure without trimerization is used for the calculations.

Figure 4.18 (a-c) shows the ϕ vs. change in energy curves for the $Mn_{3-x}Fe_xSn$ samples. The iT-AFM state with $\phi = 0$ is taken as the reference state, whose energy is subtracted from the energies of the system at different canting angles. It can be seen from plot (a) that the minima in energy lie at 0° for Mn_3Sn. The energy cost to stabilize the canted state is visibly high; thus, the pristine Mn_3Sn should be stabilize in an in-plane iT-AFM structure.

Figure 4.18 (b) shows the calculated energy curve for the Fe-doped samples. For

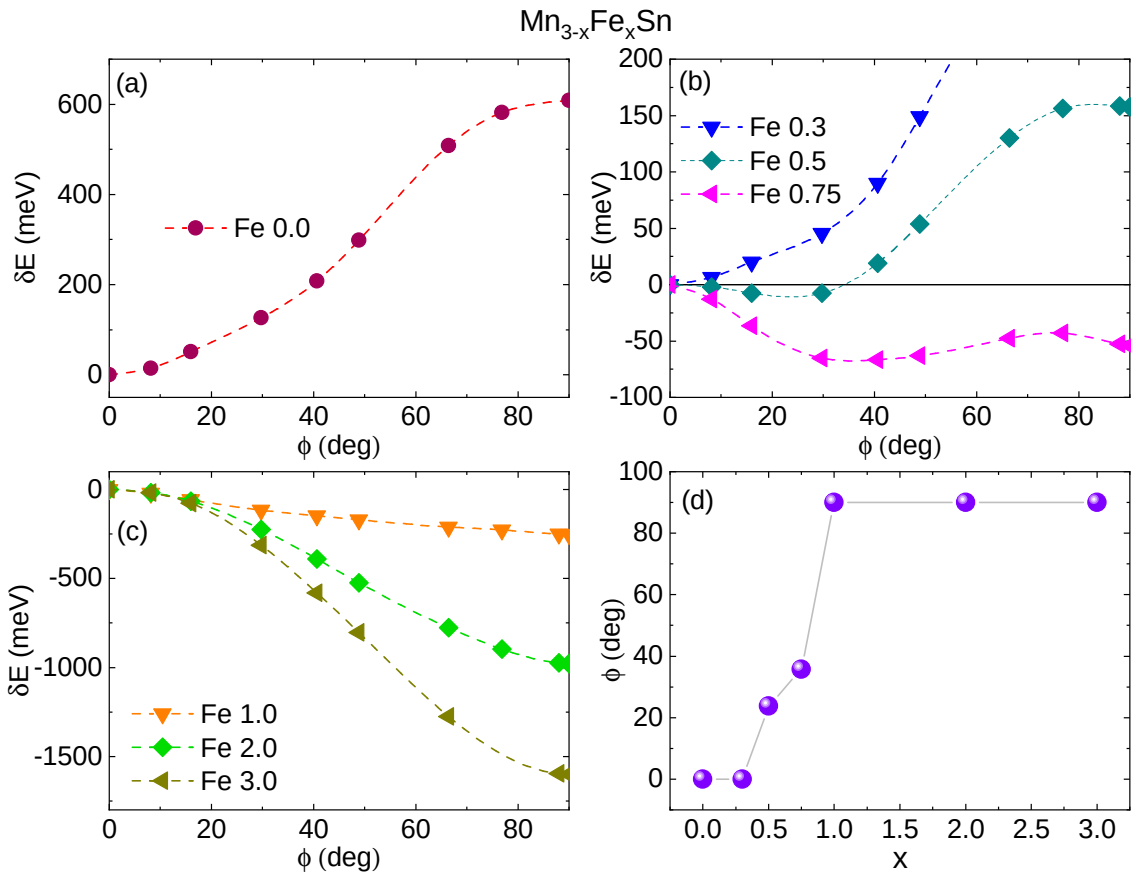

Figure 4.18: (a-c) The change in energy as a function of out-of-plane canting angle ϕ computed using the ab-initio calculation for $Mn_{3-x}Fe_xSn$ series of samples. The dotted lines are a guide to the eye. The calculations are for an ideal kagome lattice without trimerization. (d) The value of ϕ corresponding to the energy minima for different values of x.

Fe 0.3, the minimum energy ground state is still at $\phi = 0°$, with a ferromagnetic state with $\phi = 90°$ being the most energy costly. However, the energy cost for the stabilization of the canted state is reduced compared to the pristine Mn_3Sn. On further increasing the Fe content, the shape of the curve changes for $x = 0.5$ sample. The energy minima now lie at a finite value of ϕ, approximately 10 meV below the in-plane iT-AFM state. The ferromagnetic state with $\phi = 90°$ remains the most energy costly state, with a further decrease in the overall energy cost. For the energy curve for $x = 0.75$ sample, a complete reshuffling of the magnetic ground state takes place. The minimum in energy is at a finite value of angle ϕ, approximately 65 meV

below the iT-AFM structure. More interestingly, the ferromagnetic ordering now becomes more stable than the iT-AFM state and lies 55 meV below it.

Increasing the Fe doping beyond 0.75 leads to the stabilization of a ferromagnetic ground state. For x = 1.0, 2.0, and 3.0 samples [Fig. 4.18 (c)], the minima is at a value of $\phi = 90°$. The differnece between the $\phi = 0°$ and 90° magnetic state continues to increase with Fe doping. The results are summarized in Fig. 4.18 (d), where the value of ϕ corresponding to minimum energy state is plotted as a function of x.

Thus, with the electron doping by means of Fe substitution, the magnetic ground state of the sample changes from the iT-AFM state to a finite canted ground state, which further transforms to a ferromagnetic ground state with Fe doping of 1.0. Thus the theoretical results also support the presence of a canted ground state. The qualitative difference between the composition range supporting the canted state and the stability of the canted state for $Mn_{3.09}Sn_{0.91}$ sample most likely arises from the off-stoichiometry of the sample, which is not incorporated into the calculations.

A mystery that remains to be understood is the driving mechanism responsible for stabilization of the canted magnetic ground state. As we learn in the chapter 1 and 3, the exchange interactions in the Mn_3Sn sample are such that the iT-AFM state is the ground state. Analysis of exchange parameters up to six nearest neighbors do not reveal any possible way to stabilize a canted magnetic ground state. The only closest example found in the literature that shows somewhat similar properties is that of a topological material $Co_3Sn_2S_2$. $Co_3Sn_2S_2$ undergoes a temperature-dependent transition from the in-plane AFM state to a *c*-axis oriented ferromagnetic exchange.[85] The presence of anisotropic exchange interactions was found to drive this transition.[86] However, it has been reported that the anisotropic exchange interactions drive a sudden transition between the AFM and FM state without stabilizing a canted ground state. Thus, to find the reason for the stabilization of the canted ground state, we must look beyond the usual Heisenberg exchange interactions. In this context, the possibility of the presence of higher-order exchange interactions, introduced in chapter 1, will be discussed next.

Before proceeding with the analysis, let us first label the different higher-order exchange interactions for the kagome lattice of Mn_3Sn. Figure 4.19 shows a schematic of a single layer of the kagome lattice. The Heisenberg exchange interaction can be

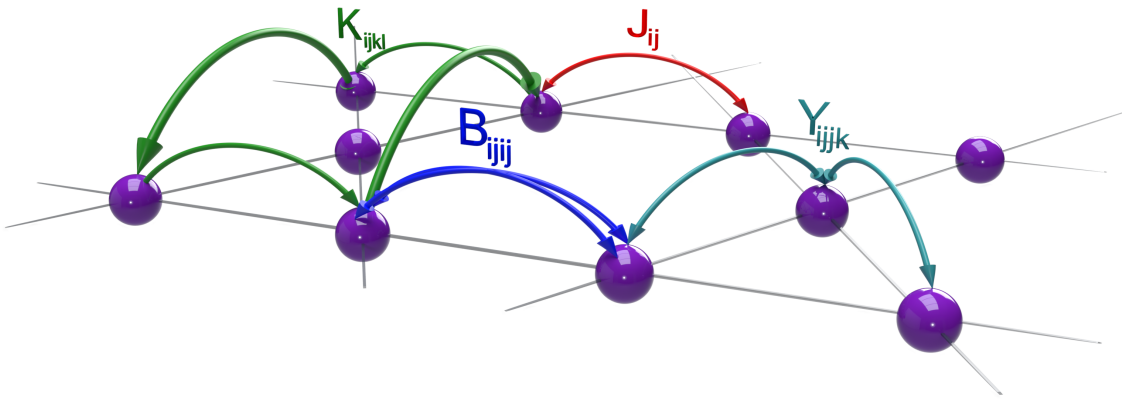

Figure 4.19: The Heisenberg exchange and the different 4-spin higher order exchange interaction on kagome lattice.

present between any two pairs of atoms and is marked by a red arrow for the nearest neighbor pair. The Heisenberg exchange interaction can also be called a 2-spin-two-site (J_{ij}) interaction. The next order of exchange interactions that can be present are the 4-spin interactions. As discussed in chapter 1, the four spin interactions can exist in three different forms, namely the 4-spin-two-site (B_{ijij}), 4-spin-three-site (Y_{ijjk}) and 4-spin-four-site (K_{ijkl}) interactions. These exchanges are marked on the kagome lattice in Fig. 4.19 with different colors. Only the 'nearest neighbor' of the 4-spn exchange interactions will be considered. While the two-site B_{ijij} and three-site Y_{ijjk} are connected by a path made up of nearest neighbor bonds, the four-site K_{ijkl} is mediated through a pair of two different bond lengths (thick and thin green arrows in Fig. 4.19).

4.7.2 Effects of higher order exchange interactions on the iT-AFM ground state

A method to evaluate exchange interaction in a material is to map the DFT calculated energies of different magnetic configurations onto an exchange Hamiltonian. Such an analysis is also performed in chapter 3 to evaluate the exchange interactions. Before starting with the analysis of the DFT calculations, let us first evaluate what sort of effects on the magnetic state can be expected upon the inclusion of higher-order exchange in the system. The Hamiltonian for the 2-spin and 4-spin

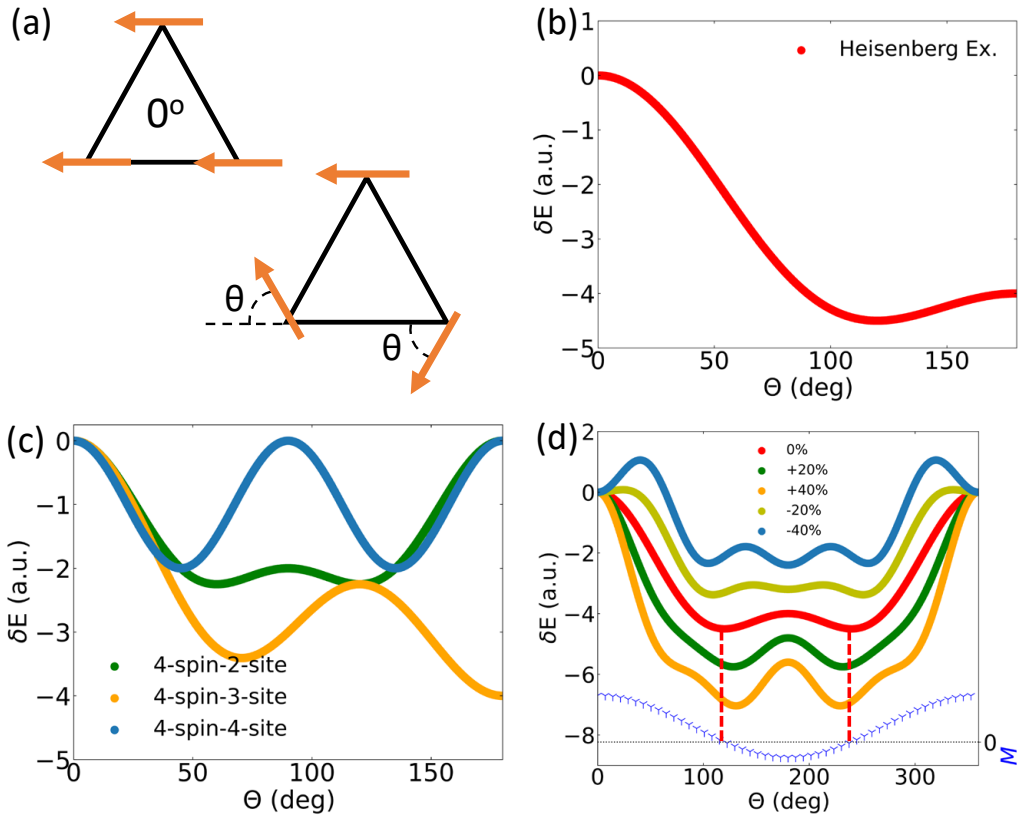

Figure 4.20: (a) Schematic of the in-plane magnetic configuration considered. (b) Energy change as a function of canting angle Θ for a set of three coplanar spins for Heisenberg exchange and (c) for 4-spin exchange interactions. (d) Energy change plots for different values for 4-spin exchange added to the Heisenberg exchange.

exchange interactions can be written as

$$H = \sum_{ij} J_{ij}(S_i.S_j) + \sum_{ij} B_{ij}(S_i.S_j)^2 + \sum_{ijk} Y_{ijk}[(S_i.S_j)(S_j.S_k) + (S_j.S_i)(S_i.S_k) + (S_i.S_k)(S_k.S_j)] + \sum_{ijkl} K_{ijkl}[(S_i.S_j)(S_k.S_l) + (S_i.S_l)(S_j.S_k) - (S_i.S_k)(S_j.S_l)] + \sum_{ijk} X_{ijk}(S_i.S_j)(S_k.S_l)(S_l.S_i). \quad (4.3)$$

The room temperature magnetic ground state of the kagome lattice in Mn_3Sn is the iT-AFM structure. Let us assess the possible modification of this ground state in two steps. First, any modification to the in-plane ground state will be studied, followed by an analysis of possible out-of-plane modifications. The analysis for the

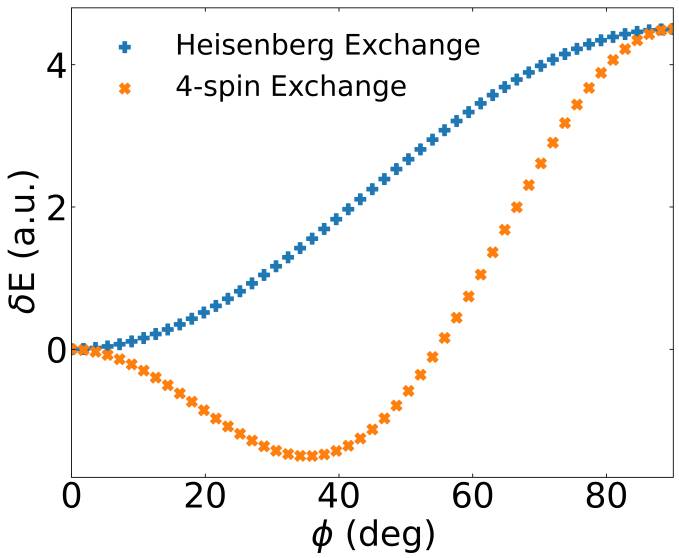

Figure 4.21: The change in energy as a function of out-of-plane canting angle ϕ for 2-spin and 4-spin exchange interactions.

in-plane magnetic state is performed as follows. The total exchange energy of three spins on a triangle is calculated by rotating the magnetic spin in the plane of the triangle. The starting position is chosen as a ferromagnetic alignment of spins, from which the two spins are rotated by an angle θ in an opposite fashion. A schematic depicting the process is shown in Fig. 4.20 (a). Figure 4.20 (b) shows the energy change from the reference state of $\theta = 0$ for only the Heisenberg exchange. It can be seen that the minimum in energy is at $\theta = 120°$ for the AFM exchange interaction (positive J for Hamiltonian 4.3). This result is expected as the ground state of three spins on a triangle with antiferromagnetic exchange is a triangular spin state.

Moving to the 4-spin exchange interactions, the same plot for different 4-spin exchange interactions is shown in Fig. 4.20 (c). It can be seen that different forms of 4-spin exchanges lead to unique energy curves for each form of the high-order interaction. It is tough to assess what kind of modification may be present by analyzing these plots. Thus, a perturbative way is explored to analyze the addition of higher-order exchange interactions. The energy is determined by perturbatively adding an equal contribution from the 4-spin components to the Heisenberg Hamiltonian. Mathematically speaking, Θ vs. energy change is plotted for $B = K = Y =$ x*J, for different values of x. The results are plotted in Fig. 4.20 (d). The plot for $x = 0$ leads to the previously discussed result with a minimum at 120°. It can be seen that the position of the minima slightly moves from the 120° with the addition

of contributions from 4-spin terms. However, the ground state is not altered drastically for smaller values of the 4-spin exchange terms. Moreover, the net in-plane magnetization is also plotted in the same figure. It can be observed that any change in magnetic state form 120° leads to a finite magnetization value. The $Mn_{3.09}Sn_{0p91}$ sample show a negligible in-plane magnetic moment. Thus it can be concluded that the effect of these interactions on the in-pane structure of samples studied here is minimal.

Next, the effect of out-of-plane canting is evaluated on the triangular spin structure. Figure 4.21 shows the out-of-plane canting angle ϕ vs. energy change plots for different exchange interactions. The $\phi = 0$ in-plane triangular spin structure is taken as the starting point, from where all the spins are canted out-of-plane by an angle ϕ. The Heisenberg exchange interaction shows a minimum at $\phi = 0$. However, all the forms of the higher-order exchange interactions show a minimum at a finite angle ϕ. Thus, the presence of higher-order exchange interaction in the kagome lattice of Mn_3Sn can modify the in-plane iT-AFM state to a canted state along the c-axis.

Now that the possibility of stabilizing a canted state by inclusion of higher order exchange interactions is demonstrated, let us analyze the DFT data obtained for different samples.

4.7.3 Analysis of the data from DFT calculations

Let us now analyze the DFT calculation performed for $Mn_{3-x}Fe_xSn$ series of samples using an ideal kagome lattice. The results are earlier presented in Fig. 4.18 where it is observed that a canted ground state can be stabilized for the intermediate values of Fe doping. The aim is to try and fit the data presented in Fig. 4.18 using the Hamiltonian 4.3. However, with the presence of multiple Heisenberg exchange interactions and possible inter-layer and intra-layer higher-order interactions, it is incredibly challenging to calculate all the exchange parameters individually. To solve this problem, a minimal model is calculated to facilitate the fitting of the DFT data. The different in-plane and out-of-plane 2-spin and 4-spin exchange interactions are marked in Fig. 4.22 (b-d).

When we look closely at all the labeled exchange interactions, it can be seen that the magnetic moment at sites connected by all of the 2-spin exchange interactions lie either parallel to each other or are at an angle of 120°. The same is true for the 4-spin exchange terms, where the spins for the B_{ijij} follow the same trend as for the Heisenberg exchange. The moment for all the paths connected by 4-spin-three-

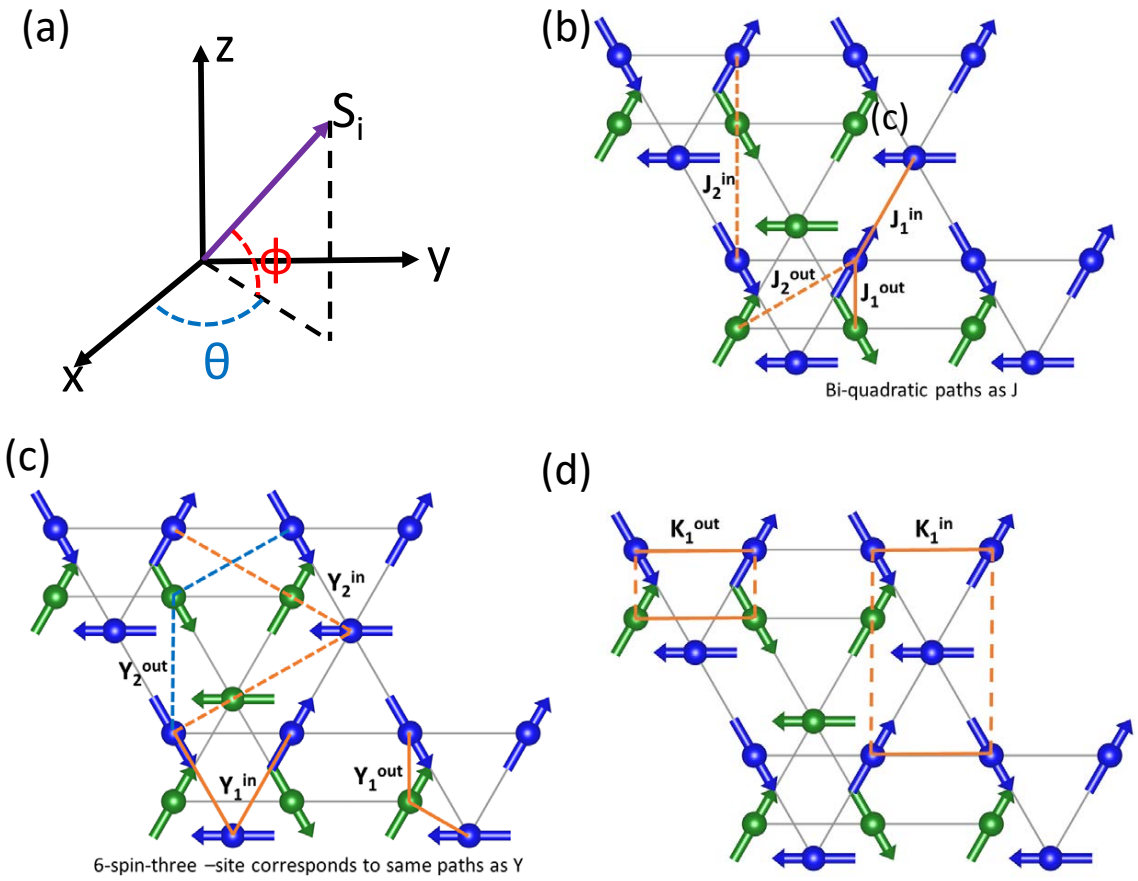

Figure 4.22: (a) Representation of the moment S_i on a coordinate system. (b-d) Different in-plane and our-of-plane 2-spin and 4-spin exchange interaction on the kagome lattice of Mn_3Sn.

site and 4-spin-four-site are all at an angle of 120°. Now, when we start from this iT-AFM ground state and cant all the moments along the c-axis, there will be no change in the energy for the moments that are initially parallel, as all the moments are canted by the same angle. Thus, the parallel moment remains parallel. The other moments at 120° to each other can be coupled together to calculate the effective contribution due to different order of exchange interactions, as shown below.

Consider a coordinate system as shown in Fig. 4.22 (a). Two magnetic moments at neighboring sites S_i and S_j can be written as

$$\begin{aligned} S_i &= \cos(\theta_1)\cos(\phi)\hat{x} + sin(\theta_1)\cos(\phi)\hat{y} + sin(\phi)\hat{z} \\ S_j &= \cos(\theta_2)\cos(\phi)\hat{x} + sin(\theta_2)\cos(\phi)\hat{y} + sin(\phi)\hat{z}. \end{aligned} \tag{4.4}$$

The dot product of these two spins can be evaluated as

$$(S_i.S_j) = \cos(\theta_1)\cos(\theta_2)\cos^2(\phi) + sin(\theta_1)sin(\theta_2)cos^2(\phi) + sin^2(\phi). \tag{4.5}$$

Now, using the fact that all pairs of spins lie at 120° to each other, we can use $\theta_2 = \theta_1 + 120°$. The Eq. 4.5 becomes

$$\begin{aligned}(S_i.S_j) &= [\cos(\theta_1)\cos(\theta_1 + 120) + sin(\theta_1)sin(\theta_1 + 120)]\cos^2(\phi) + sin^2(\phi) \\ &= [\cos(120)]\cos^2(\phi) + sin^2(\phi) \\ &= \mathbf{1} - \frac{\mathbf{3}}{\mathbf{2}}\cos^{\mathbf{2}}(\phi)\end{aligned} \tag{4.6}$$

The Hamiltonian for the Heisenberg exchanges shown in Fig. 4.22 (b) can be written as

$$H_{2-spin-two-site} = 4J_1^{in}(S_i.S_j) + 4J_2^{in}(S_i.S_j) + 4J_1^{out}(S_i.S_j) + 6J_2^{out}(S_i.S_j) \tag{4.7}$$

Using Eq. 4.6 and the fact that J_2^{out} spins are parallel to each other, Eq. 4.7 becomes

$$\begin{aligned}H_{2-spin-two-site} &= 4[J_1^{in} + J_2^{in} + J_1^{out}][1 - 1.5\cos^2(\phi)] + 6J_2^{out} \\ &= 4J_{eff}[1 - 1.5\cos^2(\phi)] + 6J_2^{out}\end{aligned} \tag{4.8}$$

Thus, the contributions from all the Heisenberg exchange interactions can be clubbed into a single functional form. To check the validity of the current approach, the DFT data for the Mn_3Sn sample is fitted using Eq. 4.8. The data and the fitted curve are shown in Fig. 4.23. It is clear that the DFT data can be fitted with the effective minimal energy model. The fitting functional for higher-order exchange interactions are also calculated following the same method. The calculated effective model Hamiltonian is written below.

$$H_{4-spin-two-site} = 4[B_1^{in} + B_2^{in} + B_1^{out}][1 - 1.5\cos^2(\phi)]^2 + 6B_2^{out} \tag{4.9}$$

$$\begin{aligned} H_{4-spin-three-site} &= \sum_{ijk} Y_{ijk}[(S_i.S_j)(S_j.S_k) + (S_j.S_i)(S_i.S_k) + (S_i.S_k)(S_k.S_j)] \\ &= \sum_{ijk} 3Y_{ijk}[1 - 1.5\cos^2(\phi)]^2 \\ &= 3[Y_1^{in} + Y_2^{in} + Y_1^{out}][1 - 1.5\cos^2(\phi)]^2 + Y_2^{out} \end{aligned} \tag{4.10}$$

$$\begin{aligned} H_{4-spin-four-site} &= \sum_{ijkl} K_{ijkl}[(S_i.S_j)(S_k.S_l) + (S_i.S_l)(S_j.S_k) - (S_i.S_k)(S_j.S_l)] \\ &= \sum_{ijkl} K_{ijkl}[[1 - 1.5\cos^2(\phi)]^2 + [1 - 1.5\cos^2(\phi)]^2 - 1] \\ &= \sum_{ijkl} K_{ijkl}[2[1 - 1.5\cos^2(\phi)]^2 - 1] \end{aligned} \tag{4.11}$$

The same procedure can be applied to even higher order of exchange interactions, like the 6-spin exchange. Finally, ignoring the constant terms, a fitting equation for different order of exchange interactions is written as

$$\begin{aligned} \delta E = E_{2-spin}(1 - 1.5\cos^2(\phi)) + E_{4-spin}(1 - 1.5\cos^2(\phi))^2 \\ + E_{6-spin}(1 - 1.5\cos^2(\phi))^3 + ... \end{aligned} \tag{4.12}$$

Figure 4.23 shows the calculated data and a fitting with Eq. 4.12. All the plots are well fitted. It is found that the data for $x = 0.3$ sample can be fitted with contributions from the 2-spin and 4-spin terms. However, a good fit is achieved for higher doping by including the 6-spin terms. The extracted total energy contribution from each exchange interaction order is summarized in Fig. 4.24. It can be seen that the effective 2-spin energy contribution changes sign around $x = 0.75$. It must be said here that the change in effective/total energy contribution does not imply that the Heisenberg exchanges have all changed from AFM to FM. Instead, the change in sign signifies a weakening of AFM exchange in comparison to the FM. The change in sign of nearest coupling does happen at the end, signified by a large negative value of E_{2-spin}.

A finite contribution of higher-order energy contribution confirms that the canted ground state is stabilized by the competition of different orders of exchange terms.

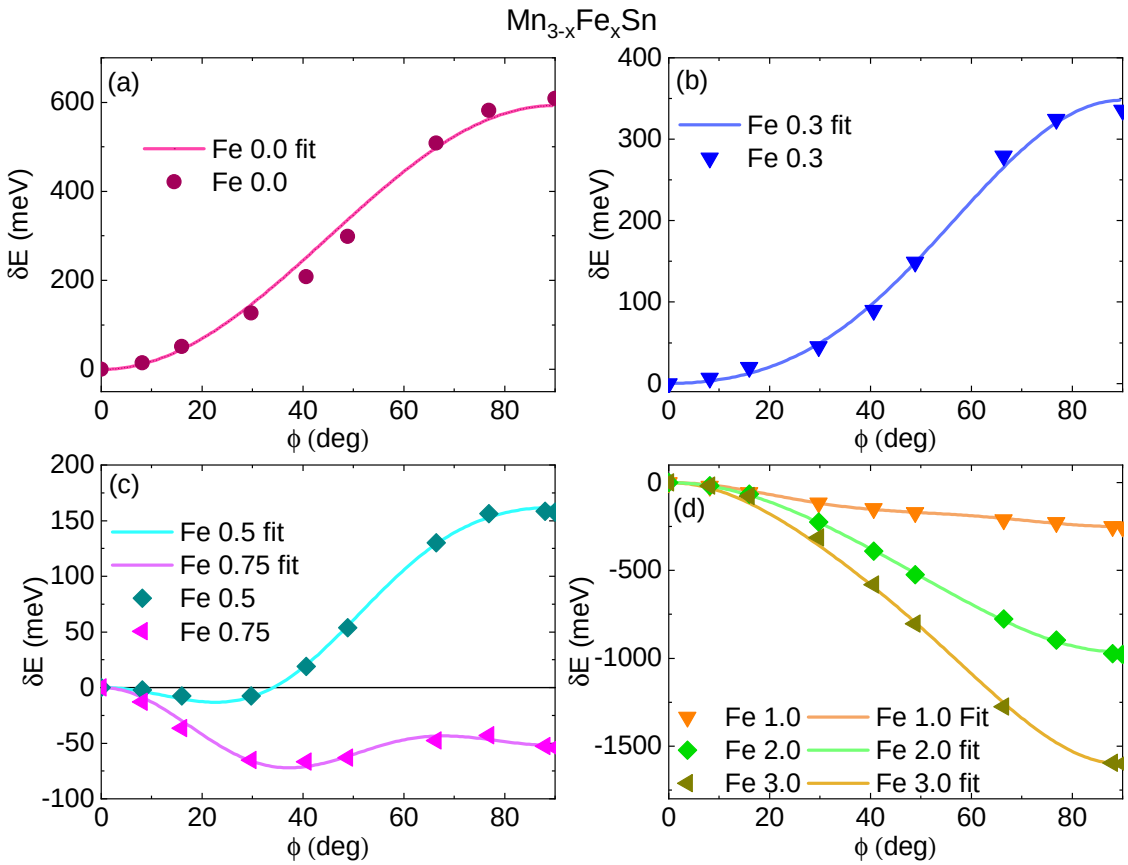

Figure 4.23: Out-of-plane canting angle dependent change in energy and fitting with Eq. 4.12 for $Mn_{3-x}Fe_xSn$ series of samples.

The higher-order exchange contribution peaks at the x=1.0 mark, which incidentally is the point where precisely one Mn atom on a triangle is replaced with a Fe atom. The exact nature and mechanism of the increase in strength of higher-order interaction with Fe doping in the current system needs further examination and is not clear as of now. The DFT results presented till now are for an ideal kagome lattice structure. As we learned in chapter 3, the trimerization can also modify the ground state of the Mn_3Sn sample. To verify the robustness of the present results, the DFT energy calculations are repeated for a relaxed kagome lattice. In this case, the ionic positions are first relaxed to obtain a minimum energy ground state. The relaxation imparts finite trimerization to the kagome lattice. The out-of-plane canting calculations are performed on the trimerized lattice, and the results are presented in Fig. 4.25. It can be seen that the energy curves for the trimerized kagome lattice show a similar nature to that of the ideal case, although with small qualitative changes. Thus the present analysis also holds true for a trimerized kagome lattice.

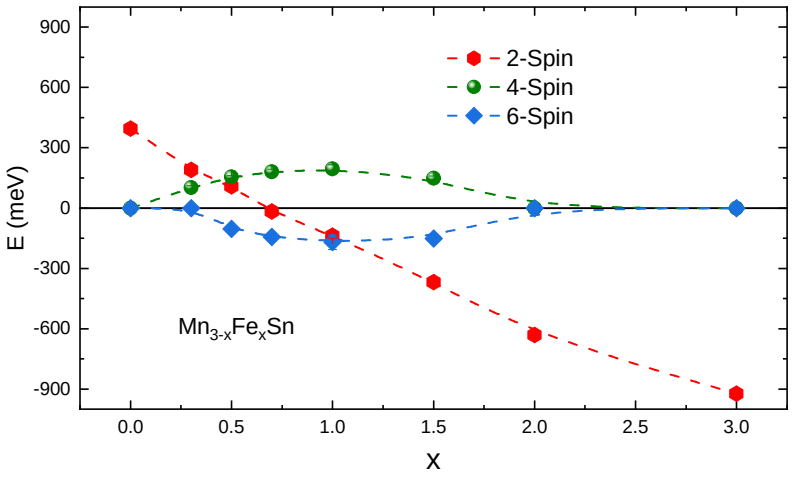

Figure 4.24: Energy contribution for different order of exchange interactions by fitting the DFT data presented in Fig. 4.23.

4.8 Conclusion

The low-temperature ground state of Mn_3Sn samples was unknown for a long time. In this chapter, the search for the 'true' ground state of highly electron-doped $Mn_{3.09}Sn_{0.91}$ and $Mn_{3-x}Fe_xSn$ samples reveal that a canted spin structure is the ground state at low temperatures. The canting of the ground state is revealed using a combination of bulk magnetization, neutron diffraction, and theoretical calculations. All the spins on the kagome lattice cant along the *c*-axis in this canted state. The canted magnetic state preserves the famous in-plane non-collinear order of Mn_3Sn. The Hall signal originating due to the octupole order of the in-plane spin structure remains robust in the canted state. In addition to the Hall signal of octupole magnetic order, a new Hall signal is found due to the finite scalar spin chirality of the canted state. Both these signals co-exist, leading to dual magnetic order in the sample. Individual manipulation of dual order reveals that these two orders are not coupled to each other and can be freely switched without perturbing the other. Theoretical calculations show that the presence of higher-order exchange interaction stabilizes the out-of-plane canting.

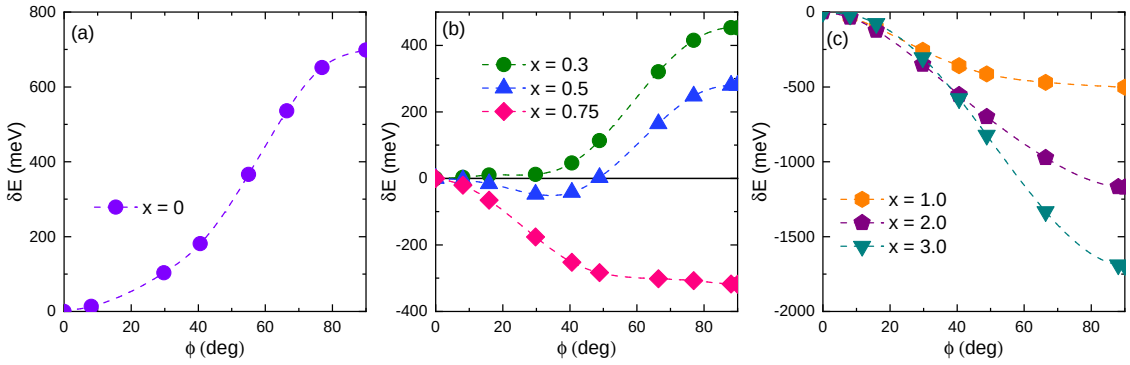

Figure 4.25: (a-c) The change in energy as a function of out-of-plane canting angle ϕ computed using the ab-initio calculation for $Mn_{3-x}Fe_xSn$ series of samples. The dotted lines are a guide to the eye. The calculations are for an relaxed kagome lattice that exhibit finite trimerization.

Chapter 5

Magnetic properties of Sb doped Mn_3Sn samples

The previous chapter examines the low-temperature ground state of highly electron-doped Mn_3Sn samples. A combination of experimental and theoretical studies found the stabilization of a canted magnetic state. The canted state is stabilized by the presence of 4-spin and 6-spin higher-order exchange interactions. Theoretical results reveals that the higher-order exchange interactions plays a important role in the electron doped samples. The doping by Fe atoms leads to the addition of an electron to the system. However, the exact role of Fe doping, hence the additional electron(s), in strengthening the higher-order terms is still unknown. One central question that arises from the perspective of electron doping: Is it always the case that additional electrons would increase the strength of higher-order exchange interaction? To find an answer to this question, this chapter takes an alternate route toward electron doping. Instead of replacing the d element with another electron-rich atom, the addition of electrons is carried out by doping the p element, i.e., the Sn atom. A natural candidate for such doping is antimony, which has an extra electron than the

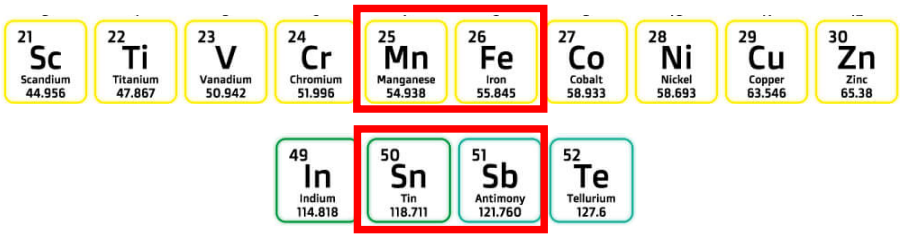

Figure 5.1: Picture of the $3d$ row and some $5p$ elements of the periodic table.

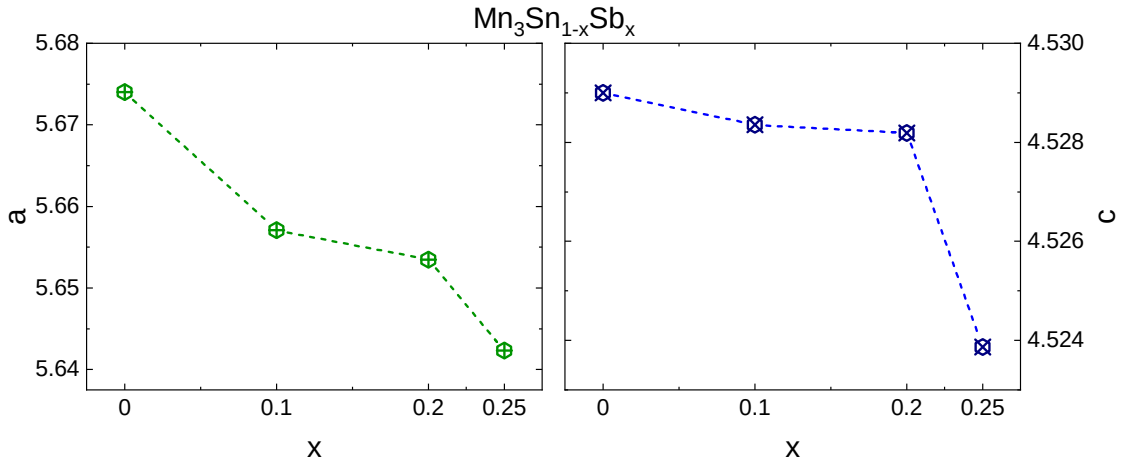

Figure 5.2: Variation of lattice constants a and c with Sb doping for $Mn_3Sn_{1-x}Sb_x$ samples.

Sn atom (Fig. 5.1). Thus, polycrystalline samples of form $Mn_3Sn_{1-x}Sb_x$ are synthesized using the arc melt furnace. The Sb doping is carried out for the $Mn_{3.03}Sn_{0.97}$ samples. Throughout this chapter, the $Mn_{3.03}Sn_{0.97}$ samples will be mentioned and written as Mn_3Sn samples unless specified otherwise.

5.1 Structural characterization of Sb doped samples

The Sb doped samples are synthesized for three different compositions with Sb = 0.1, 0.2, and 0.25. Samples above 0.25 could not be obtained with a single phase. Figure 5.4 shows the XRD patterns of these three samples. The Rietveld refinement is also shown for the samples. It can be seen that the samples crystallize in the hexagonal kagome structure of Mn_3Sn. No extra peaks can be observed in the patterns, confirming a single phase of the samples. The extracted a and c values of the lattice parameters are plotted in Fig. 5.2 (a) and (b), respectively. It is observed that both the lattice parameters decrease slightly with increased doping. However, a noticeable feature for the change in c values is seen.

5.2 Compositional analysis

To check the compositional homogeneity, the FESEM measurements are performed on the $Mn_3Sn_{1-x}Sb_x$ sample as shown in Figure 5.3. The homogeneous contrast

(a) $Mn_3Sn_{0.9}Sb_{0.1}$

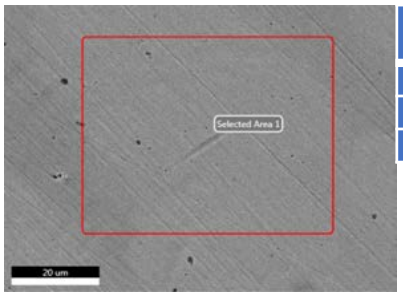

Element	Weight %	Atomic %	Error %
SnL	34.7	20.4	2.2
SbL	5.0	2.8	8.5
MnK	60.3	76.7	2.5

(a) $Mn_3Sn_{0.8}Sb_{0.2}$

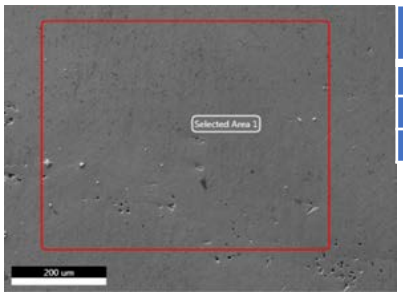

Element	Weight %	Atomic %	Error %
SnL	32.1	18.9	2.2
SbL	7.7	4.4	4.9
MnK	60.2	76.6	2.5

Figure 5.3: The FESEM images and corresponding EDS results for $Mn_3Sn_{1-x}Sb_x$ samples.

of these images confirms the formation of single phase for all the samples. The exact stoichiometry of the samples is studied with help of the EDS measurement and nearly matched with the expected value.

5.3 Magnetic properties of samples

After confirming the crystalline nature of the samples, the magnetic characterization of the samples is carried out. The $M(T)$ measurements are performed on the three samples in the ZFC and FC modes, as shown in Fig. 5.5 (a-c). The $Mn_3Sn_{0.9}Sb_{0.1}$ sample shows a similar $M(T)$ plot to that of the parent $Mn_{3.03}Sn_{0.97}$ sample. With the reduction of temperature, the magnetization suddenly falls at the helical phase transition. The temperature corresponding to the helical transition increases in comparison to that of $Mn_{3.03}Sn_{0.97}$ sample. With increased Sb doping, the $Mn_3Sn_{0.8}Sb_{0.2}$ sample also shows a further increase in the helical phase transition temperature. The ordering temperature T_N, corresponding to the transition of iT-AFM structure to paramagnetic phase, is also observed for this sample. In addition to the helical transition and ordering temperature, some slight features in the $M(T)$ plots are also observed below the helical phase transition. These features en-

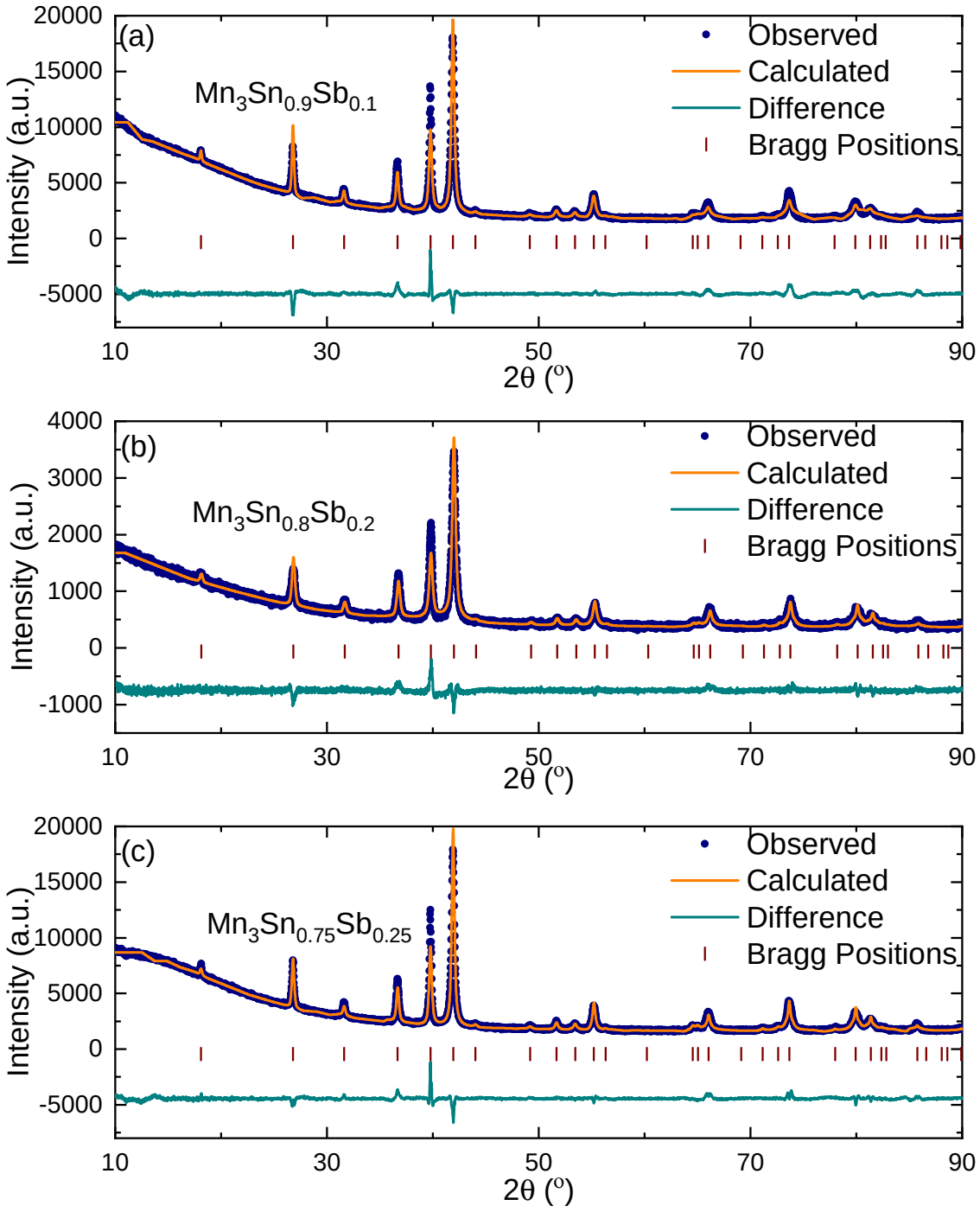

Figure 5.4: XRD pattern and Rietveld refinement data for the three samples of $Mn_3Sn_{1-x}Sb_x$ series.

hance sharply for the $Mn_3Sn_{0.75}Sb_{0.25}$ sample. The helical phase transition increases further, and the ordering temperature recedes for this sample. The transition temperatures corresponding to the helical phase and Neel temperature are plotted in

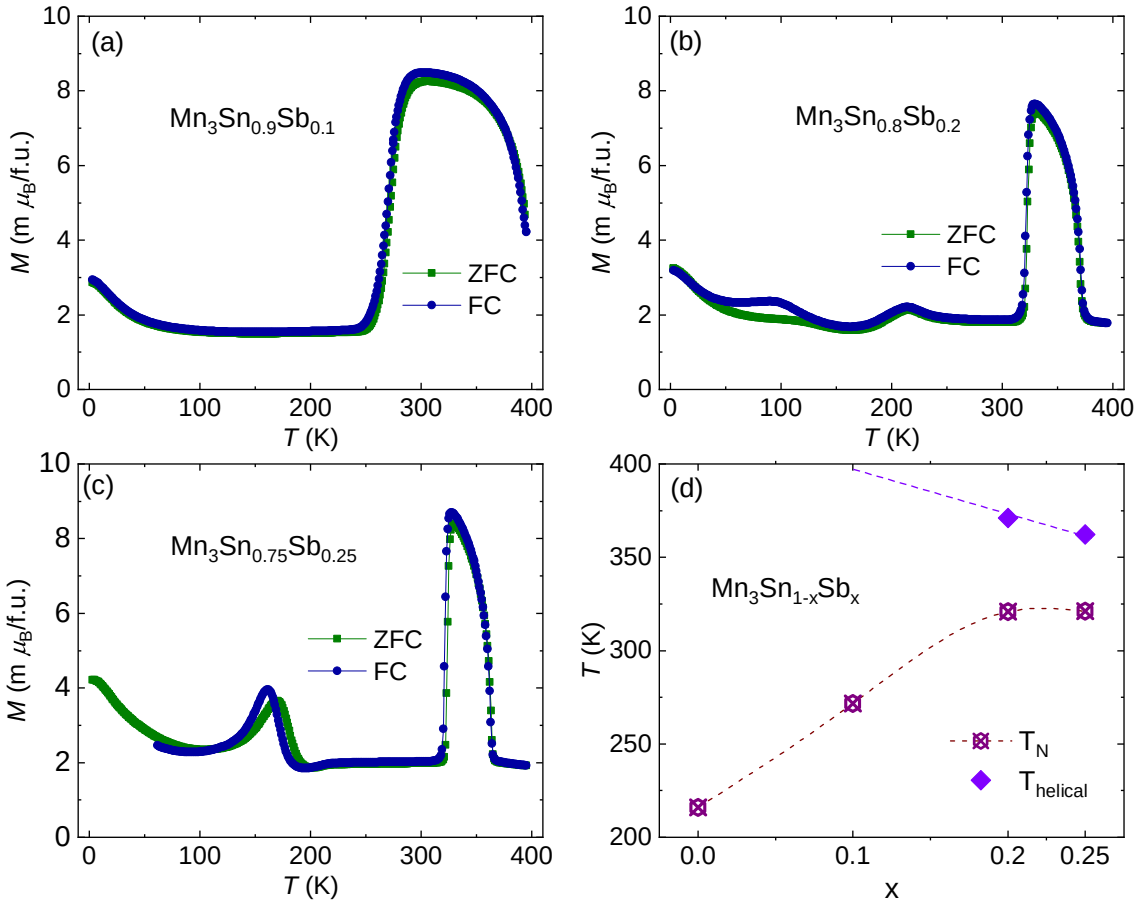

Figure 5.5: ZFC and FC $M(T)$ measurements at an applied field of 1000 Oe for (a) $Mn_3Sn_{0.9}Sb_{0.1}$, (b) $Mn_3Sn_{0.8}Sb_{0.2}$ and (c) $Mn_3Sn_{0.75}Sb_{0.25}$. (d) Dependence of T_N and temperature of helical transition with Sb doping.

Fig. 5.5 (d).

Thus, the Sb doping moves the helical phase transition to higher temperatures, whereas a reduction in the ordering temperature is also observed. Moreover, the $Mn_3Sn_{0.8}Sb_{0.2}$ and $Mn_3Sn_{0.75}Sb_{0.25}$ samples show additional transition(s) below the helical phase transition temperature.

5.4 Electronic transport properties

The longitudinal and transverse resistivity measurements are performed next on the Sb doped samples. Figure 5.6 shows the room temperature normalized resistivity data for the three samples. The samples show a metallic nature in the ρ_{xx} measurements. The normalized resistivity of samples at low temperatures increases

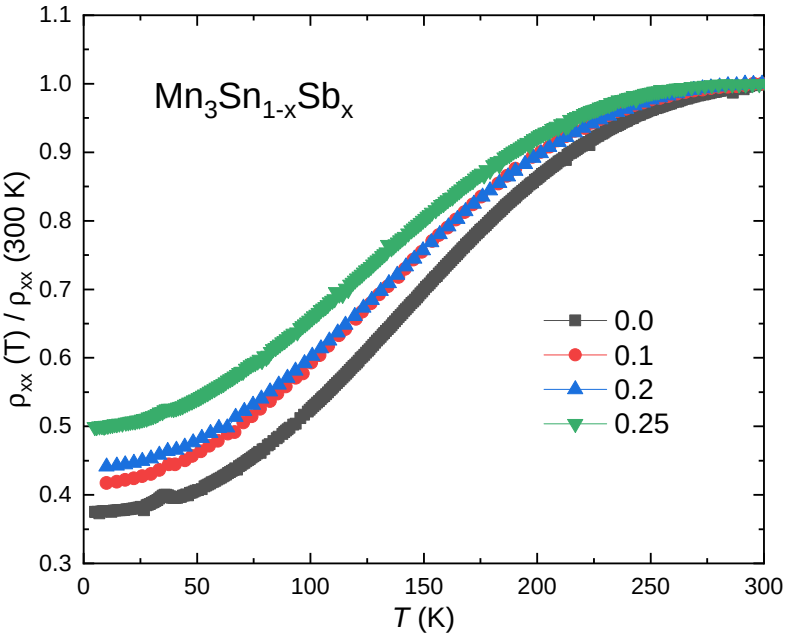

Figure 5.6: Room temperature normalized resistivity data for different samples of series $Mn_3Sn_{1-x}Sb_x$.

with increasing the Sb doping. This increase can be accounted by the fact that the doped Sb atoms in the samples can act as impurity centers in the crystal lattice. The scattering of electrons from these impurities can lead to the observed increase in the normalized resistivity data at low temperatures.

The Hall resistivity (ρ_{xy}) data for the $Mn_3Sn_{0.8}Sb_{0.2}$ and $Mn_3Sn_{0.75}Sb_{0.25}$ sample measured at different temperatures are plotted in Fig. 5.7 . The $Mn_3Sn_{0.8}Sb_{0.2}$ sample shows an anomalous Hall signal at room temperature and 330 K. Below the room temperature, no anomalous Hall signal is observed in the helical phase transition. The Hall signal for $Mn_3Sn_{0.8}Sb_{0.2}$ sample shows a similar trend as that of $Mn_{3.03}Sn_{0.97}$ sample. A finite Hall signal is observed above the helical phase transition, whereas the AHE signal is absent in the helical phase of the iT-AFM structure. The $Mn_3Sn_{0.75}Sb_{0.25}$ sample also shows similar Hall signal trends. However, no signature of the additional transition is found in the transport properties of these two samples. Hence, it can be concluded that the new transition in the helical phase of these samples does not alter the null Berry phase of the helical phase of the iT-AFM structure. Most importantly, unlike the finding of canted magnetic state in the Fe doped samples in the last chapter, the Sb doping does not help in the stabilization of noncoplanar magnetic state at low temperatures.

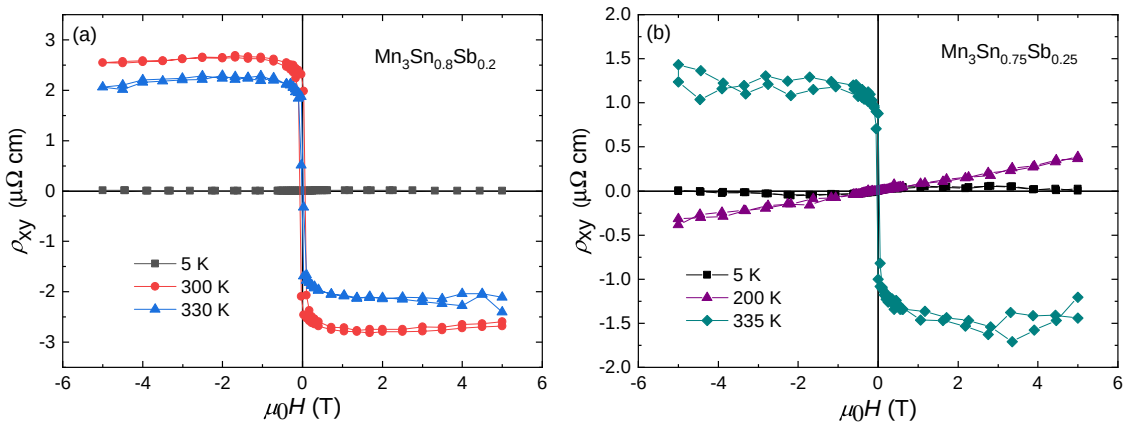

Figure 5.7: Field dependent Hall measurements at different temperatures for (a) $Mn_3Sn_{0.8}Sb_{0.2}$ and (b) $Mn_3Sn_{0.75}Sb_{0.25}$ sample.

5.5 Summary and Discussion of experimental results

The electron doping for the Mn_3Sn sample by substituting Fe in place of Mn leads to a predominance of the higher-order exchange interactions, evident from the non-coplanar magnetic ground state. However, the electron doping through substitution of Sn atoms by Sb atoms does not produce the same results. The ground state for the Sb doped samples shows a transition of the iT-AFM ground state to the helical phase. An increase in Sb doping leads to a more extensive temperature range for which the helical phase is stable. These observations display the importance that the doping of the Mn element by a similar *d* element carries.

Thus, in conclusion, although we have employed the electron doping as a means of modifying the ground state magnetic state of Mn_3Sn samples, the exact effect of the doping depends on the kind of dopant and at which site the doping has been performed. The substitution of Sn sites by the *d* element Mn in chapter 3 leads to the stabilization of canted state, whereas, the Sb doping leads to enhancement of the helical phase in large temperature region. These contrasting effect could be arising due to the different category of the Mn and Fe atoms, and also due to the fact that the Mn doping at Sn sites act as a magnetic defect, whereas Sb and Sn are similar in nature. The exact role of the magnetic mn defects in modifying the exchange constants and thus the magnetic ground state is still a mystery. Further studies of the electron doping by Fe atoms are required to understand how the higher-order exchange interactions can be tuned in a magnetic system. Moreover,

the Sb doped samples show a previously unnoticed magnetic transition in the helical phase of samples. The transport properties of the system do not change during this transition. This implies that the magnetic transition does not alter the Berry physics of the system. More studies of the Sb doped samples are required to find the exact nature of the new transition.

Chapter 6

Summary and conclusion

After rigorous presentation and examination of the experimentally recorded data and in-depth theoretical analysis, it is time to summarize the works that constitute this thesis. The main aim of the present thesis is to understand the temperature-dependent magnetic ground state of the kagome lattice compound Mn_3Sn. The inverse triangular spin structure of Mn_3Sn leads to a zero magnetic moment non-collinear magnetic ground state at room temperature. The iT-AFM state has been studied for various non-trivial properties of the antiferromagnetic (AFM) sample, the most notable and first of those being the presence of a large Anomalous Hall effect (AHE). The AHE is usually absent in the AFM samples with protected time-reversal symmetry. However, Mn_3Sn breaks this TRS due to the presence of cluster octupole order.

Although the room temperature magnetic state of Mn_3Sn is very well known, a complete understanding of the temperature dependent modification of the magnetic ground state has been lacking. The work in this thesis is focused on the understanding of the magnetic states. The literature analysis in chapter 1 reveals that the samples show two distinct types of magnetization trends with temperature. One is a dramatic decrease in magnetization at about 200 K, while the other is a sudden rise at 50 K. The understanding of these two magnetic transition is the main goal of the this thesis. Before presenting the work, the second chapter of thesis presents a detailed analysis of the experimental instruments used and the theoretical tools employed to carry out the present work.

The first task of the work is to synthesize the samples with two distinct temperature profiles. It is shown that a small electron doping can do it in the off stoichiometric $Mn_{3+x}Sn_{1-x}$ samples. The $Mn_{3.03}Sn_{0.97}$ sample shows a drop in the magnetization, and $Mn_{3.05}Sn_{0.95}$ sample exhibit the increase in magnetization with

decreasing temperatures. The magnetic transition corresponding to the drop in the magnetization has been studied earlier. It was revealed that a helical modulation of the iT-AFM along the *c*-axis of the hexagonal unit cell takes place below this transition. However, the exact interplay of exchange interactions for the stabilization of the helical phase was not known. Moreover, the low-temperature transition was a complete mystery except for the information that it shows a 'glassy ferromagnetism. A spin glass signature sits on top of the ferromagnetic long-range order in the glassy ferromagnetic phase.

Chapter 3 focuses on the exact mechanism and external control of the helical phase transition. The temperature-dependent XRD measurements revealed a sudden change in lattice parameters at the helical phase, which prompted a study of the properties of these samples under external pressure. The magnetic and transport measurements reveal that the application of pressure on the $Mn_{3.05}Sn_{0.95}$ sample without showing a helical phase can give rise to the stabilization of helical phase. This control leads to switching the AHE signal, which is highly sought after in the field of spintronics. The switching of AHE by pressure-induced magnetic phase transition reveals a unique way to manipulate the non-collinear AFM state. An analysis of the exchange Hamiltonian suggests that a helical phase can be stabilized due to the exchange frustration between different out-of-plane exchange interactions. The $ab-initio$ Density Functional Theory (DFT) studies show that the change in magnetic state with pressure is brought about by the pressure-induced trimerization of the kagome lattice. The kagome lattice comprises two corner-sharing triangles, usually equal in size. However, for Mn_3Sn, one triangle is smaller, and the other is larger than the ideal kagome lattice. This process is termed as the trimerization of the kagome lattice. Increased trimerization with pressure changes the strength of the frustrated out-of-plane exchanges to the helical phase structure. Thus, the exact process of stabilizing the helical phase and its controlled transformation is demonstrated.

Chapter 4 focuses on decoding the low temperature (< 50 K) phase of the electron-rich $Mn_{3.09}Sn_{0.91}$ samples. As it appears, the electron doping stabilizes the low-temperature phase, additional electron doping is achieved by doping Fe atoms instead of Mn atoms, i.e., the $Mn_{3-x}Fe_xSn$. The results from the magnetization studies on the single-crystal samples showed a behavior as expected. It is shown that the temperature T_{SR} of the spin reorientation transition and the magnetic moment of the samples increases with increasing Fe doping for samples up to $Mn_{2.3}Fe_{0.7}Sn$. The magnetic measurements on the single crystals further reveals that the rise in

magnetization at low temperature transition arises when the field is applied along the c-axis of the samples. In contrast, the in-plane magnetization remains more or less the same. The Fe-doped samples also showed similar behavior. Thus a simple model is proposed based on these measurements. In this model, the magnetic moments of the iT-AFM state exhibit a canting along the $-c$ axis of the hexagonal unit cell. This model is confirmed by neutron diffraction measurements in $Mn_{2.5}Fe_{0.5}Sn$ sample. The neutron diffraction measurements show intensity redistribution at the spin reorientation transition. The value of the canting angle for the $Mn_{2.5}Fe_{0.5}Sn$ sample is found to be 15°.

The canting in the iT-AFM state leads to a non-coplanar state instead of the earlier non-collinear. However, the in-plane component of the canted state remains the same as that of the iT-AFM state. Thus the canted state preserves the cluster octupole order of the sample. In addition to the octupole order of the in-plane domains, the non-coplanar canted ground state exhibits a finite scalar spin chirality at the ground state. This ordered finite scalar spin chirality at the ground state can generate finite Berry curvature. The Hall measurements on the three single crystalline samples reveal an extremely anisotropic Hall signal. The octupole order-induced Hall signal is observed in the ρ_{xz} component, where a field along the y-axis aligns the octupole domains. Furthermore, for the applications of the magnetic field along the c-axis, the ρ_{xy} component shows a Hall signal which appears below the T_{SR} temperature and vanishes above it. Thus the canted ground state host two magnetic orders, the octupole, and the SSC dipole. The possibility of individually manipulating these two orders is shown by utilizing a rotator setup, where the sample is rotated with respect to the magnetic field direction. Thus, the sample exhibits a dual order magnetic state, which is the first report of its kind.

The DFT calculations data also supports the stabilization of the canted magnetic ground state. The DFT calculations are performed to analyze the ground state of $Mn_{3-x}Fe_xSn$ samples. It is found that the Mn_3Sn shows an iT-AFM state, while the Fe_3Sn shows a ferromagnetic ground state. However, a canted ground state with a finite value of the canting angle is found for the samples with Fe between 0.3 to 0.7. The 2-spin Heisenberg exchange cannot stabilize this intermediate state, as a change in sign of J leads to a sudden AFM to FM transition. An analysis of the DFT data with an appropriate Hamiltonian reveals that the higher-order exchange interaction stabilizes the canted state. On the kagome lattice, these interactions take various forms. The main contribution to the exchange energy arises from the 4-spin exchange terms, whereas the 6-spin exchange interaction also contributes at

higher Fe doping. Thus, the higher-order exchange interaction modifies the iT-AFM state, leading to the dual order phenomenon. The new order displays a large AHE signal due to the SSC mechanism.

Chapter 5 focuses on an alternate route toward electron doping of the Mn_3Sn sample. The Sn atoms are replaced by electron-rich Sb atoms to observe if there is any enhancement of the higher-order exchange and thus the non-coplanar ground state. However, it is observed that the Sb doping leads to stabilization and expansion of the helical phase of the iT-AFM structure. Thus, only the electron doping can not be held responsible for enhancing higher-order interactions in the $Mn_{3-x}Fe_xSn$ system. Even more detailed studies are required to understand the evolution of the higher-order exchanges. Moreover, the Sb ≥ 0.2 samples show an additional transition inside the helical phase of the iT-AFM structure. This phase does not show any signatures in the Hall signal. The exact magnetic structure of this transition needs further examination.

In conclusion, the high-temperature helical phase transition and the low temperature magnetic phase are studied in details. The exact ground state and mechanism of these magnetic phases have been comprehensively understood.

6.1 Future Outlook

The present findings exploring the mechanism of magnetic phase transitions in the triangular antiferromagnetic Mn_3Sn is important from the application perspective, as well as deeper understanding of the underlying physics. The pressure-induced trimerization in Mn_3Sn demonstrates a unique method of switching the anomalous Hall signal. Moreover, the change in Hall signal by modification of magnetic structure, rather than inverting the polarity of magnetic moments, represents a broader opportunity for the manipulation of non-trivial, non-collinear antiferromagnetic phases in terms of device applicability. The effect of pressure can be reproduced in thin films of material using the strain from an appropriate substrate. Even more importantly, a piezoelectric substrate can modify the applied stain; thus, the magnetic state and Hall signal can also be manipulated. Moreover, the thin-film systems also present an opportunity to apply uniaxial strain/stress, which can further enrich the understanding of the different magnetic phases.

The higher-order exchange stabilized canted magnetic state found at the low temperatures and the subsequent observation of dual order can lead to drastic consequences. First, the presence of higher-order interactions changes the energy land-

scape of magnetic interaction. This modification calls for a reevaluation of the calculations that are based on the exchange Hamiltonian. Other than that, the ferromagnetic moments stabilized due to the canting of the iT-AFM state interact with the in-plane iT-AFM state through strong exchange interactions. This exchange coupling can modify various properties, starting from the damping mechanism to the Heisenberg nature of the ferromagnetic moments. Moreover, the first experimental observation of dual order phenomenon in the present system invites more theoretical and experimental studies on this behavior. In addition to the effects related to experimental results, the demonstration of higher-order interactions in Mn_3Sn also calls for careful examination of exchange interaction in other materials. A simple comparison of different collinear and non-collinear magnetic states may not reveal the complete set of exchange interactions. Instead, the distinct functional form of these interactions must be utilized to map the energies of a set of calculations to confirm the presence/absence of higher-order terms.

References

[1] M. N. Baibich et al., *Phys. Rev. Lett.*, **61**, 2472–2475 (1988).

[2] G. Binasch et al., *Phys. Rev. B*, **39**, 4828–4830 (1989).

[3] P. Grünberg et al., *Phys. Rev. Lett.*, **57**, 2442–2445 (1986).

[4] S. S. P. Parkin, N. More, and K. P. Roche, *Phys. Rev. Lett.*, **64**, 2304–2307 (1990).

[5] M. Julliere, *Physics Letters A*, **54**, 225–226 (1975).

[6] V. Baltz et al., *Rev. Mod. Phys.*, **90**, 015005 (2018).

[7] P. W. Anderson, *Phys. Rev.*, **79**, 350–356 (1950).

[8] Clarence Zener, *Phys. Rev.*, **82**, 403–405 (1951).

[9] P. G. de Gennes, *Phys. Rev.*, **118**, 141–154 (1960).

[10] Warren E. Pickett and David J. Singh, *Phys. Rev. B*, **53**, 1146–1160 (1996).

[11] Tôru Moriya, *Phys. Rev.*, **120**, 91–98 (1960).

[12] I. Dzyaloshinsky, *Journal of Physics and Chemistry of Solids*, **4**, 241–255 (1958).

[13] Allan H MacDonald, SM Girvin, and D t Yoshioka, *Physical Review B*, **37**, 9753 (1988).

[14] Minoru Takahashi, *Journal of Physics C: Solid State Physics*, **10**, 1289 (1977).

[15] S. Grytsiuk et al., *Nature Communications*, **11**, 511 (2020).

[16] Markus Hoffmann and Stefan Blügel, *Phys. Rev. B*, **101**, 024418 (2020).

[17] Sascha Brinker, Manuel dos Santos Dias, and Samir Lounis, *Phys. Rev. Research*, **2**, 033240 (2020).

[18] Taro Nakajima et al., *Science Advances*, **3**, e1602562 (2017).

[19] X. Z. Yu et al., *Nature*, **465**, 901–904 (2010).

[20] Ajaya K. Nayak et al., *Nature*, **548**, 561–566 (2017).

[21] Jagannath Jena et al., *Nano Letters*, **20**, 59–65 (2020).

[22] Markus Hoffmann and Stefan Blügel, *Physical Review B*, **101**, 024418 (2020).

[23] Ph. Kurz et al., *Phys. Rev. Lett.*, **86**, 1106–1109 (2001).

[24] Niklas Romming et al., *Physical review letters*, **120**, 207201 (2018).

[25] Andreas Krönlein et al., *Physical review letters*, **120**, 207202 (2018).

[26] P. Ferriani et al., *Phys. Rev. Lett.*, **101**, 027201 (2008).

[27] Mara Gutzeit et al., *Phys. Rev. B*, **104**, 024420 (2021).

[28] Andreas Krönlein et al., *Phys. Rev. Lett.*, **120**, 207202 (2018).

[29] Jiayong Zhang et al., *Chinese Physics B*, **25**, 117308 (2016).

[30] Hui Li et al., *Nature Communications*, **7**, 10301 (2016).

[31] J Smit, *Physica*, **21**, 877–887 (1955).

[32] Jan Smit, *Physica*, **24**, 39–51 (1958).

[33] Naoto Nagaosa et al., *Rev. Mod. Phys.*, **82**, 1539–1592 (2010).

[34] Hiroaki Ishizuka and Naoto Nagaosa, *Science Advances*, **4**, eaap9962 (2018).

[35] Yukako Fujishiro et al., *Nature communications*, **12**, 1–6 (2021).

[36] Robert Karplus and J. M. Luttinger, *Phys. Rev.*, **95**, 1154–1160 (1954).

[37] Di Xiao, Ming-Che Chang, and Qian Niu, *Reviews of modern physics*, **82**, 1959 (2010).

[38] Yuan Tian, Li Ye, and Xiaofeng Jin, *Phys. Rev. Lett.*, **103**, 087206 (2009).

[39] J.W. Cable, N. Wakabayashi, and P. Radhakrishna, *Solid State Communications*, **88**, 161–166 (1993).

[40] Shōichi Tomiyoshi and Yasuo Yamaguchi, *Journal of the Physical Society of Japan*, **51**, 2478–2486 (1982).

[41] Pyeongjae Park et al., *npj Quantum Materials*, **3**, 63 (2018).

[42] Satoru Nakatsuji, Naoki Kiyohara, and Tomoya Higo, *Nature*, **527**, 212–215 (2015).

[43] Muhammad Ikhlas et al., *Nature Physics*, **13**, 1085–1090 (2017).

[44] Xiaokang Li et al., *Phys. Rev. Lett.*, **119**, 056601 (2017).

[45] K Kuroda et al., *Nature materials*, **16**, 1090–1095 (2017).

[46] Tomoya Higo et al., *Nature Photonics*, **12**, 73–78 (2018).

[47] Taishi Chen et al., *Nature Communications*, **12**, 572 (2021).

[48] Hao Yang et al., *New Journal of Physics*, **19**, 015008 (2017).

[49] M.-T. Suzuki et al., *Phys. Rev. B*, **95**, 094406 (2017).

[50] Shinji Miwa et al., *Small Science*, **1**, 2000062 (2021).

[51] Motoi Kimata et al., *Nature Communications*, **12**, 5582 (2021).

[52] Motoi Kimata et al., *Nature*, **565**, 627–630 (2019).

[53] Jianpeng Liu and Leon Balents, *Phys. Rev. Lett.*, **119**, 087202 (2017).

[54] Pradeep K. Rout et al., *Phys. Rev. B*, **99**, 094430 (2019).

[55] James M. Taylor et al., *Phys. Rev. B*, **101**, 094404 (2020).

[56] Yunfeng You et al., *Advanced Electronic Materials*, **5**, 1800818 (2019).

[57] Xiaokang Li et al., *Nature Communications*, **10**, 3021 (2019).

[58] Takuya Matsuda et al., *Nature Communications*, **11**, 909 (2020).

[59] Xiaofeng Zhou et al., *Applied Physics Letters*, **115**, 182402 (2019).

[60] Durga Khadka et al., *Science Advances*, **6**, eabc1977 (2020).

[61] Hanshen Tsai et al., *Nature*, **580**, 608–613 (2020).

[62] N. H. Sung et al., *Applied Physics Letters*, **112**, 132406 (2018).

[63] Ioan Mihai Miron et al., *Nature*, **476**, 189–193 (2011).

[64] Luqiao Liu et al., *Science*, **336**, 555–558 (2012).

[65] J. E. Hirsch, *Phys. Rev. Lett.*, **83**, 1834–1837 (1999).

[66] Yuzhu Song et al., *Phys. Rev. B*, **101**, 144422 (2020).

[67] Bing Cheng et al., *Applied Physics Letters*, **115**, 012405 (2019).

[68] WJ Feng et al., *Physical Review B*, **73**, 205105 (2006).

[69] Hiroaki Okamoto et al. *ASM Handbook ; volume 3*. ASM International, 2016.

[70] Pamela C Burnley. *Diamond Anvil Cell, serc.carleton.edu*. 2022.

[71] Guoyin Shen et al., *High Pressure Research*, **40**, 299–314 (2020).

[72] Rob McQueeney. *Magnetic neutron diffraction presentation*. 2018.

[73] P. E. Blöchl, *Phys. Rev. B*, **50**, 17953–17979 (1994).

[74] G. Kresse and J. Hafner, *Phys. Rev. B*, **47**, 558–561 (1993).

[75] G. Kresse and J. Hafner, *Phys. Rev. B*, **49**, 14251–14269 (1994).

[76] G. Kresse and J. Furthmüller, *Phys. Rev. B*, **54**, 11169–11186 (1996).

[77] G. Kresse and J. Furthmüller, *Computational Materials Science*, **6**, 15–50 (1996).

[78] John P. Perdew, Kieron Burke, and Matthias Ernzerhof, *Phys. Rev. Lett.*, **77**, 3865–3868 (1996).

[79] *FLEUR Project. Available at: http://www.apw.de.*

[80] Ph. Kurz et al., *Phys. Rev. B*, **69**, 024415 (2004).

[81] *Distorted low-level signal readback of AC signals in the PPMS in the temperaturerange 25-35 K due to Inconel mitigation of inductive cross talk. https://qdusa.com/siteDocs/ap*

[82] TB Britton et al., *Materials Characterization*, **117**, 113–126 (2016).

[83] PJ Brown et al., *Journal of Physics: Condensed Matter*, **2**, 9409 (1990).

[84] M. Taillefumier et al., *Phys. Rev. B*, **74**, 085105 (2006).

[85] Z. Guguchia et al., *Nature Communications*, **11**, 559 (2020).

[86] Julian Legendre and Karyn Le Hur, *Phys. Rev. Research*, **2**, 022043 (2020).